THE UNIVERSITY OF CHICAGO

ANALYSIS OF COSMIC MICROWAVE BACKGROUND TEMPERATURE AND *E*-MODE POLARIZATION ANISOTROPIES WITH 2019 AND 2020 DATA FROM THE SOUTH POLE TELESCOPE

A DISSERTATION SUBMITTED TO
THE FACULTY OF THE DIVISION OF THE PHYSICAL SCIENCES
IN CANDIDACY FOR THE DEGREE OF
DOCTOR OF PHILOSOPHY

DEPARTMENT OF PHYSICS

BY
WEI QUAN

CHICAGO, ILLINOIS
JUNE 2024

TABLE OF CONTENTS

LIST OF FIGURES

ACKNOWLEDGMENTS

Without unconditional and unwavering support that my parents have given me since I was little, I would not be able to finally complete my dissertation and earn a doctoral degree after almost three decades of education including eight and a half years of graduate school.

My parents have always sought better educational opportunities for me and put that as their top priority. Some examples are taking me to a different country (from China to Japan) and allowing me to experience a new culture, arranging tutoring sessions at home to help me improve my English, and encouraging me to study in the United States and supporting me through my college years at the University of Washington, where I decided to major in physics and started an intellectual journey that has lasted until today and is still continuing. I feel enormously privileged to have had these opportunities and grateful to my parents.

I have worked in the South Pole Telescope (SPT) collaboration for the past seven years and have been helped by many members of the collaboration. I am grateful to every one of my collaborators.

Early on, I worked on low-level data analysis projects. One project was to investigate spectral lines in raw data from detectors. I thank Jason (Henning), Nicholas (Harrington), Sasha (Rahlin), Nathan (Whitehorn), and others for helping me learn how to use SPT's software and analyze raw data. Another project was to build a data quality monitoring system, which comprises several analysis pipelines that calculate data quality metrics from various types of data that we take everyday and a webpage that displays the results. I thank Adam (Anderson) for building the basic framework of the system, without which my work would not have been possible. I also thank Anne (Gambrel), Karia (Dibert), Sam (Guns), Matt (Young), and others for sharing useful code with me when I was creating contents for the webpage. In recent months, Kyle (Ferguson), Kyra (Fichman), and Anna (Coerver) added new contents to the webpage. I thank them as well.

Although I had only a brief period of lab experience, it was an extremely meaningful and

fulfilling period in which I learned many useful things about our instrument. I thank Daniel (Dutcher), Zhaodi (Pan), Joshua (Sobrin), Brad (Benson), Amy (Bender), Amy (Lowitz), Clarence (Chang), Tyler (Natoli), and others for teaching me many things and thank John (Hood) and Ellie (Rath) for being my lab partners.

Deploying to the south pole was absolutely one of the biggest highlights of my graduate school life. I thank Junhan (Kim), Allen (Foster), Judith (Stephen), and others for being my guides on my way to the south pole and during my several weeks of stay on the ice.

For the past four years, I have been co-leading a science analysis project, which is also my thesis project, with Etienne (Camphuis). It has been a great pleasure to work with him. I have enjoyed working with other members of the SPT Paris group as well. I thank Federica (Guidi), Lennart (Balkenhol), Silvia (Galli), Eric (Hivon), and others. Many data products needed by our project were either provided by others or created with much help from others. I thank Melanie (Archipley) and Lindsey (Bleem) for constructing catalogs of galaxies and galaxy clusters, Neil (Goeckner-Wald) and Nicholas (Huang) for measuring the point spread functions of the telescope, Yuuki (Omori) for creating and running simulations, and Cail (Daley) for working with me on making CMB maps. I also thank Jessica (Zebrowski), Christian (Reichardt), Kimmy (Wu), and others for stimulating discussions on calculating power spectra of CMB anisotropies in general.

Besides my research, interacting with members of the Chicago SPT group, especially graduate students, through group meetings and social activities has brought me much joy. I thank Paul (Chichura), Alec (Hryciuk), Emily (Martsen), Kayla (Kornoelje), Jody (Chou), and others. Working with Juliet (Crowell) on various outreach events was very enjoyable as well.

For every task of every project that I worked on, I would not have been able to make progress without guidance from Tom (Crawford) and conversations with him. I cherish many fun and intellectually simulating discussions that I had with him, especially discussions on

Fourier transforms. I feel that Tom has given me a lot of freedom to pursue any investigations that intrigued me rather than simply telling me what I should do. I appreciated his mentoring style very much. Not only has Tom always helped my research and many other students' and postdocs', he has also always strived to make the Chicago SPT group and the wider collaboration welcoming places by taking actions related to equity, diversity, and inclusion. (I also appreciate all the pastries he brought to group meetings and all the humorous things he said!) I feel extremely lucky that I had him as my advisor. I feel extremely lucky that I also had John (Carlstrom) as my advisor. Working by the side of a towering figure in the field like John has been inspiring. Although John's extremely busy schedule did not allow him to have many meetings with me about the nitty-gritty of my projects, he always gave me interesting insights whenever I showed him some results.

I have tried to remember as many things that I did in SPT as possible and people who helped me along the way, but I almost certainly forgot some names (for which I apologize...), so I would like to say thank you to the entire collaboration, and I conclude my acknowledgments.

ABSTRACT

The angular power spectra of the three types of two-point correlation functions obtained from the cosmic microwave background (CMB) temperature and E-mode polarization anisotropies (the $TT/TE/EE$ spectra) encode information on the composition and evolution of the universe. Measurements of the spectra contributed to establishing the ΛCDM cosmological model as the standard, and the satellite experiment *Planck* achieved subpercent-precision constraints on parameters of ΛCDM by mainly using its TT/TE spectra at large angular scales.

However, there are also challenges to ΛCDM, a major one being the Hubble tension. Better measurements of the TE/EE spectra at small angular scales by other experiments like the South Pole Telescope (SPT) can serve as a powerful consistency test of *Planck*'s results and provide new insights on the tension. Since 2019, we have been taking data consistently with SPT-3G, the third-generation imaging instrument installed on the telescope in 2017.

My thesis project is about analyzing data from 2019 and 2020 to substantially improve SPT-3G's existing measurements of the TE/EE spectra and constraints on cosmological parameters based on data from 2018 and to prepare for a future analysis based on the full dataset from SPT-3G. The analysis comprises three major steps: making CMB anisotropy maps from time series recorded by detectors, calculating the $TT/TE/EE$ spectra from the maps, and fitting cosmological models to the spectra. As of the writing of this thesis in February 2024, we have produced maps and spectra and are working on constraining cosmological models. Uncertainties in the TE/EE spectra obtained from this new dataset are smaller than those from the 2018 dataset by an order of magnitude at small angular scales, and we are excited to significantly improve our existing constraints on cosmological parameters such as the Hubble constant.

This thesis comprises four chapters. In chapter 1, I will discuss the origin of the three types of spectra, current measurements of the spectra and constraints on ΛCDM parameters, and

future directions in the field. After that, I will introduce SPT-3G in chapter 2 by discussing important properties of the instrument and showing example raw data. Then, in chapter 3, I will discuss the dataset used in the analysis and methods involved in each major step of the analysis, In the final chapter, chapter 4, I will discuss further details of some of the methods and report results from them, show our maps and spectra, and discuss tasks that remain to be done.

CHAPTER 1

COSMIC MICROWAVE BACKGROUND

Discovered by Penzias and Wilson in mid-1960s (Penzias and Wilson [1965]), the cosmic microwave background (CMB) has been an important subject of study in the field of cosmology for decades.

The CMB is faint microwave radiation that fills the entire universe, and this radiation is full of interesting properties. Its total intensity is remarkably isotropic, and its spectrum has the best blackbody form ever seen in nature (Mather et al. [1990], figure 2). The corresponding blackbody temperature is approximately 2.73 K (for example, Fixsen et al. [1996]). The isotropy is not perfect, and there exists a small anisotropic component at the level of 100 μK (for example, Bennett et al. [1996], figure 4) on top of the isotropic component at 2.73 K. The dominant isotropy and the small anisotropy are visualized in figure 1.1.

The discovery of this nearly isotropic radiation with a blackbody spectrum provided major evidence supporting that the universe was once in a much hotter state (Dicke et al. [1965]), and the study of the small anisotropy made essential contributions to establishing the ΛCDM cosmological model as the current standard model (for example, Bennett et al. [2003]).

The CMB is also slightly linearly polarized (for example, Hu and White [1997]). Unlike the total intensity, the polarization intensity does not have a dominant isotropic component. However, it does have anisotropy at the level of 10 μK, approximately an order of magnitude smaller than the anisotropy in the total intensity.

Here are a few notes related to some terms. Although the polarization anisotropy is also expressed in the unit of temperature, I will use the term *temperature anisotropy* to mean the anisotropy in the total intensity and the term *polarization anisotropy* to mean the anisotropy in the polarization intensity. The term *specific intensity* means energy per unit time, unit

area, unit frequency, and unit solid angle (some definitions may not include the solid angle), and the term *intensity* means specific intensity integrated over a frequency interval.

The discovery of the polarization anisotropy (Kovac et al. [2002]) and subsequent refined measurements (for example, Brown et al. [2009], Crites et al. [2015], Henning et al. [2018], Choi et al. [2020], and Aghanim et al. [2020a]) strengthened what had been learned from the temperature anisotropy, though there is much more the polarization anisotropy can offer. An important goal of current and future CMB experiments is to measure the polarization anisotropy with greater accuracy and precision. Better measurements will provide new insights into outstanding issues in ΛCDM and potential new physics.

In the following sections of this chapter, I will discuss what physical mechanisms created the temperature and polarization anisotropies observed today, what current measurements look like, and what future measurements will be important to make.

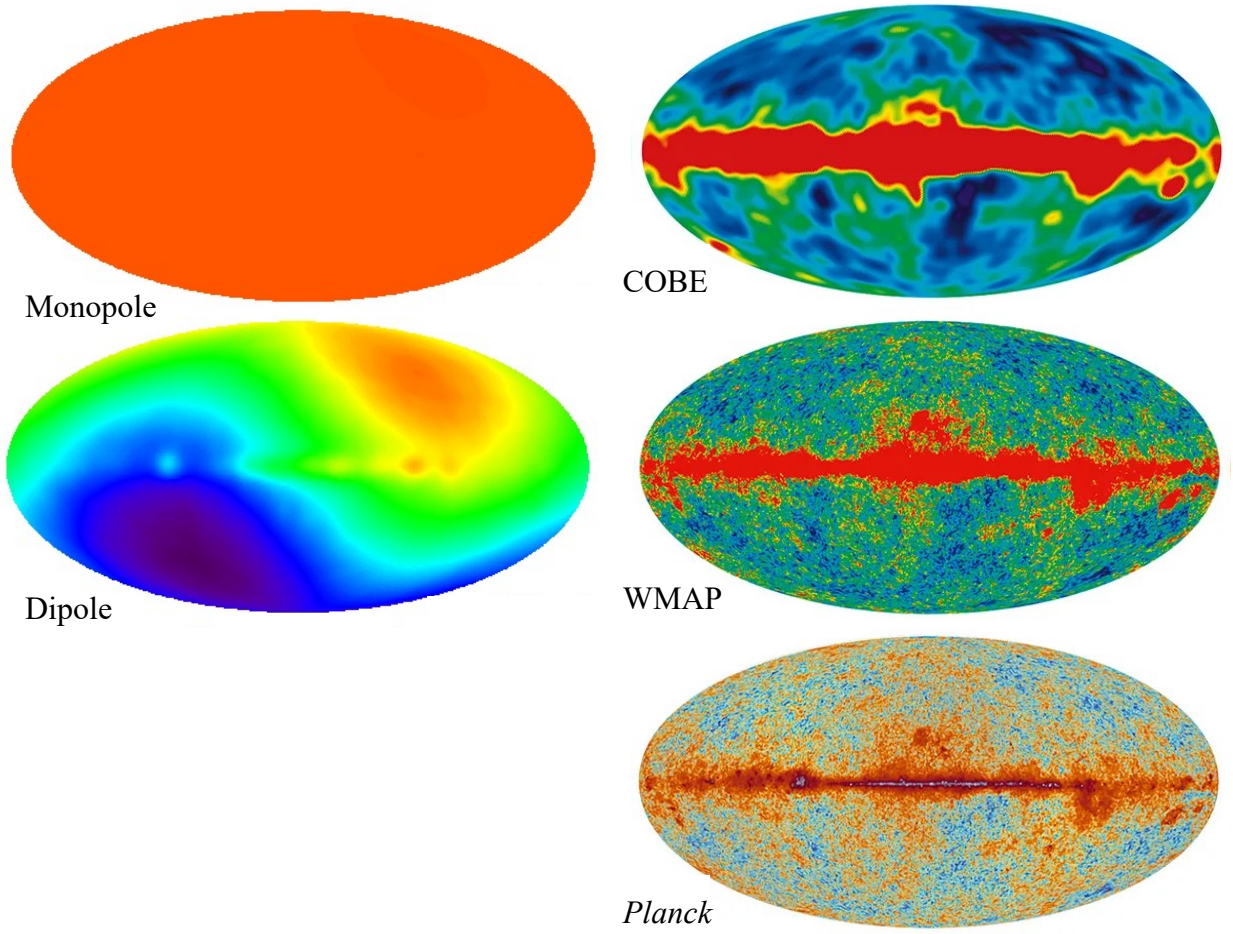

Figure 1.1. Isotropy and anisotropy of the CMB temperature. The top-left image shows that the temperature has a dominant isotropic component, which is at 2.73 K. The bottom-left image shows that the next dominant component is a dipole, which is interpreted as the Doppler shift of the CMB caused by the motion of the solar system relative to a special reference frame in which the CMB does not have such a dipole. This reference frame is known as the CMB rest frame. The amplitude of the dipole is approximately 3.4 mK. After the dipole is removed, there are temperature fluctuations at the level of 100 μK, which have been measured with higher resolution and lower noise by three generations of satellite experiments COBE, WMAP, and *Planck* (shown in the right images) and multiple ground-based experiments. Image sources: NASA LAMBDA Archive and BBC Sky at Night MAGAZINE.

1.1 Temperature Anisotropy

A sky map of the temperature anisotropy can be represented as a function on the sphere. I will use the symbol $\Delta T(\hat{\boldsymbol{n}})$. At each location on the sphere, $\Delta T(\hat{\boldsymbol{n}})$ gives the difference between the temperature at that location and the mean value, 2.73 K. This function's angular power spectrum, C_ℓ^{TT}, is calculated through a spherical harmonic transform as follows:

$$T_{\ell m} = \int \Delta T(\hat{\boldsymbol{n}})\, Y^*_{\ell m}(\hat{\boldsymbol{n}})\, d\hat{\boldsymbol{n}} \tag{1.1}$$

$$C_\ell^{TT} = \frac{1}{2\ell+1} \sum_{m=-\ell}^{\ell} T^*_{\ell m}\, T_{\ell m}. \tag{1.2}$$

(Because the temperature anisotropy measured by an experiment is represented as an image that has a set of pixels, equation 1.1 is replaced by a discrete spherical harmonic transform in practice.)

This angular power spectrum is a statistical estimator of a theoretical spectrum that we would like to know. At each ℓ, all the $2\ell+1$ spherical harmonic coefficients are supposed to be random draws from the same Gaussian probability density function. The mean of the Gaussian is zero, and the variance is a fundamental, theoretical quantity that we would like to know. I will call this quantity $C_{\ell,\,th}^{TT}$. Because C_ℓ^{TT} is in the form of a sum of the squares of $2\ell+1$ Gaussian random variables at each ℓ, for an ensemble of universes based on the same $C_{\ell,\,th}^{TT}$, the sums from the ensemble follow a χ^2 distribution that has $2\ell+1$ degrees of freedom, and the variance of the distribution is $2{C_{\ell,\,th}^{TT}}^2/(2\ell+1)$. Even if an experiment had no noise and were perfect in every other way, C_ℓ^{TT} determined by the experiment would still have an irreducible variance as an estimator of $C_{\ell,\,th}^{TT}$ because the number of spherical harmonic modes at each ℓ that can be used to estimate the variance of the underlying Gaussian probability density function is finite. This variance is known as the cosmic variance, and the uncertainty

in C_ℓ^{TT} as an estimator of $C_{\ell,\,th}^{TT}$ has the following expression:

$$\sigma(C_\ell^{TT}) = \sqrt{\frac{2}{2\ell+1}}\, C_\ell^{TT}. \tag{1.3}$$

Refined versions of this equation will appear in discussions in later sections.

Figure 1.2 shows what $C_{\ell,\,th}^{TT}$ might look like and what C_ℓ^{TT} obtained by a perfect experiment in one of the ensemble of universes based on that $C_{\ell,\,th}^{TT}$ might look like. In fact, the figure shows $D_{\ell,\,th}^{TT}$ and D_ℓ^{TT}, where $D_{\ell,\,th}^{TT} = [\ell(\ell+1)/(2\pi)]C_{\ell,\,th}^{TT}$, and $D_\ell^{TT} = [\ell(\ell+1)/(2\pi)]C_\ell^{TT}$. While $C_{\ell,\,th}^{TT}$ represents the average power in the temperature anisotropy possessed by each of the $2\ell + 1$ modes belonging to a particular ℓ, $D_{\ell,\,th}^{TT}$ represents the total power possessed by all the modes per unit logarithmic interval of ℓ. According to a prediction of the theory of cosmological inflation, $D_{\ell,\,th}^{TT}$ should be approximately constant at ℓs below a few tens. The spectrum indeed has a plateau at those ℓs, but the plateau is hard to see unless the spectrum is plotted against $\ln \ell$. Even when a focus is not on the low ℓs, D_ℓs are still used commonly and often plotted against ℓ rather than $\ln \ell$ in the literature. The values of $D_{\ell,\,th}^{TT}$ at different ℓs represent levels of temperature fluctuations at different angular scales. The relation between an ℓ and the angular scale that it represents is approximately the following: $\theta = 180/\ell$, where θ is expressed in degrees.

Nonzero values of $D_{\ell,\,th}^{TT}$ mean that the CMB temperature has fluctuations/anisotropy. According to the theory of cosmological inflation, the universe underwent an exponential expansion for a small fraction of the first second of the history of the universe, and density fluctuations in matter and radiation were created at the end of inflation. (Although there are other theories of what happened at the very beginning of the universe, inflation is the current leading theory.) These density fluctuations then caused fluctuations in the temperature of the CMB.

Other than simply having nonzero values, $D_{\ell,\,th}^{TT}$ has a series of peaks and troughs, which are caused by oscillations of matter and radiations in early universe. After the density fluctu-

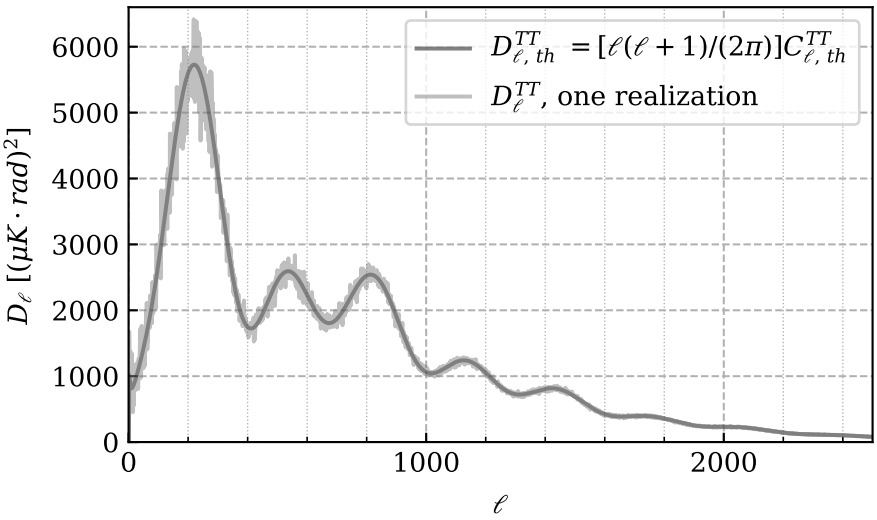

Figure 1.2. Theoretical angular power spectrum of the temperature anisotropy. One realization of this theoretical spectrum that might be measured by a perfect experiment in one universe from an ensemble of universes based on the same theory is also shown.

ations were created by inflation or possibly another mechanism, baryons, electrons, and photons tightly interacted with one another through Coulomb interactions between the baryons and electrons and through Thomson scattering of the photons off the electrons. There were also gravitational interactions among the constituents of this photon-baryon fluid and between the fluid and dark matter. Gravity caused the fluid to compress toward potential wells, but at some point the radiation pressure of the fluid became high enough to cause the fluid to expand. This interplay of the gravity and pressure caused the fluid to oscillate, and the oscillations are known as the acoustic oscillations.

The acoustic oscillations can be decomposed into independent standing-wave oscillations of individual Fourier components of the density fluctuations of the fluid. Each standing wave was an oscillating fluctuation of the density and thus temperature of the fluid. The longer the wavelength of a standing wave, the slower its oscillation. Measurements of $D^{TT}_{\ell,\,th}$ have indicated that the initial condition of the fluid was such that all the standing waves started

to oscillate at nearly the same phase and amplitude.

When the temperature of the universe became low enough for neutral hydrogen to form (approximately 3000 K and 380 000 years after the big bang), the photons no longer had free electrons to interact with and decoupled from the rest of the fluid, and the individual standing waves stopped oscillating at different phases. The baryons and dark matter then started to gravitationally collapse to form stars, galaxies, and other structures. The photons have traveled mostly freely since then and reach us today, and they give us a view that is a superposition of all the standing-wave oscillations that froze at different phases and had different density and temperature fluctuations. The peaks of $D_{\ell,th}^{TT}$ receive contributions from those standing waves that froze when their amplitudes were at maxima, and the troughs receive contributions from those waves that froze when their amplitudes were at zero. For example, the first peak is associated with the waves that froze when the fluid achieved maximal compression inside potential wells for the first time and was about to expand, and the peaks at higher ℓs are associated with waves that had shorter wavelengths and had oscillated more by the time they froze. Shorter wavelengths correspond to to smaller ℓs. Figure 1.3 illustrates these situations.

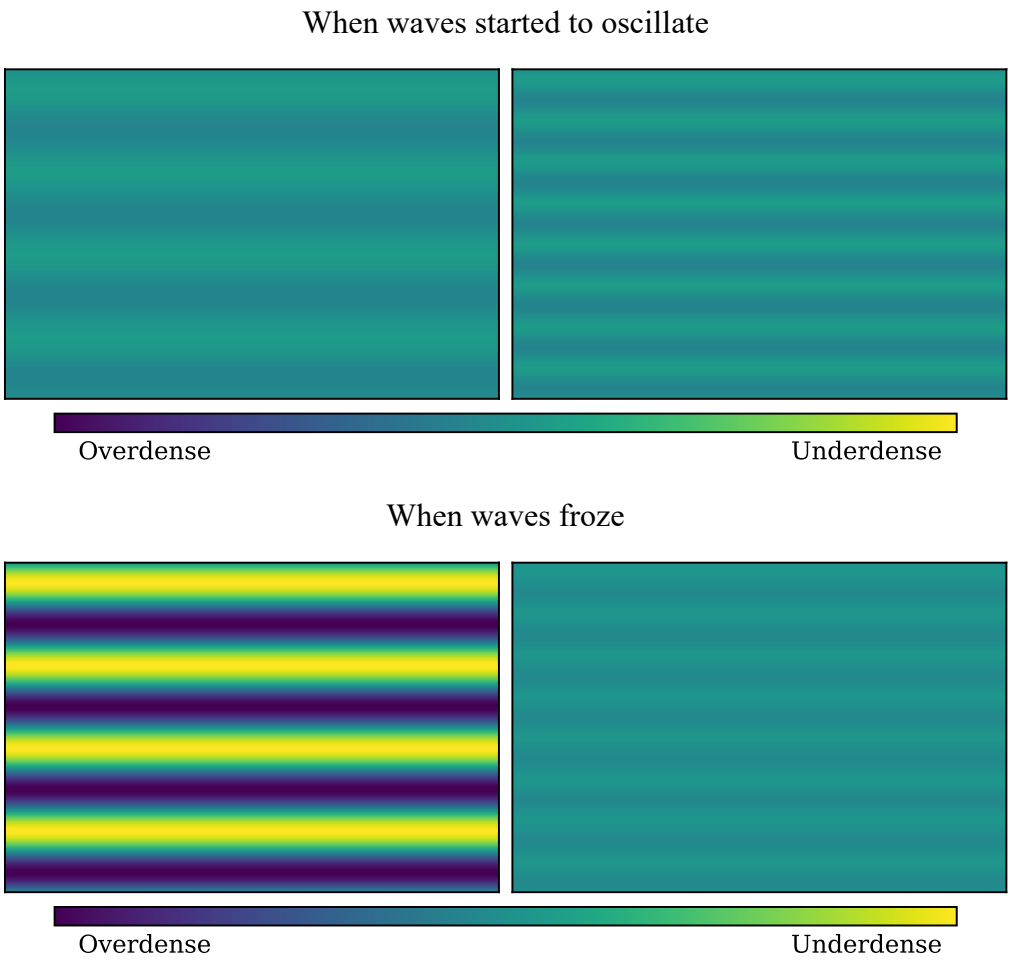

Figure 1.3. Standing-wave oscillations at two different times. The top image shows two standing waves that had different wavelengths and started to oscillate at the same phase near the beginning of the universe. The colors represent the density fluctuations within the waves. The bottom image shows the two waves when they froze. The left wave contributes more power to D_ℓ^{TT} than the right one.

1.2 E-mode Polarization Anisotropy

Polarization of the CMB was caused by Thomson scattering of CMB photons that had local quadrupole variations in their temperatures. Figure 1.4 shows how a quadrupole variation in the temperatures of photons surrounding an electron can create polarization in the radiation scattered from the electron. Different physical mechanisms created local quadrupole variations in the temperatures of the photons of the photon-baryon fluid in early universe, and the standing-wave oscillations were the major mechanism. Figure 1.5 shows how flows of photons, baryons, and electrons at different locations of one Fourier component of the fluid created polarization when the standing-wave oscillation of that Fourier component froze and how the polarization varies along the wave vector. As shown in that figure, the directions of the polarization created by the flows are either parallel or perpendicular to the wave vector of the oscillation. This type of polarization is called the E-mode polarization. (On the other hand, a gravitational wave can create local quadrupoles by stretching and contracting space, and the directions of polarization created in this case can be diagonal to the wave vector when the wave is projected onto the sky in a certain way.) When multiple waves whose wave vectors have the same magnitude but different directions are superposed (superposing rotated versions of the figure), a radial or tangential polarization pattern shown in figure 1.6 can form around an underdense or overdense region. As a result, there are fluctuations in the E-mode polarization as well as the temperature of the CMB.

While the temperature anisotropy observed today was caused by density fluctuations of the photon-baryon fluid, the E-mode polarization anisotropy was caused by velocities of the fluid. To be more specific, the temperature anisotropy is associated with the amplitudes of the standing waves when the oscillations froze, and the polarization anisotropy is associated with the time derivatives of the amplitudes of the waves when the oscillations froze.

Like a map of the temperature anisotropy, a map of the E-mode polarization anisotropy

can be constructed, which will be discussed in subsection 3.3.1, and the angular power spectrum of the map can be calculated. Figure 1.7 shows a theoretical angular power spectrum of the E-mode polarization, $D^{EE}_{\ell,th}$. A shrunk version of $D^{TT}_{\ell,th}$ is also shown. The peaks and troughs in $D^{EE}_{\ell,th}$ are out of phase with respect to the peaks and troughs in $D^{TT}_{\ell,th}$. This is because the standing wave oscillation of a Fourier mode of the fluid had a maximum amplitude when the time derivative of the amplitude was zero, at which point there was no flows in that mode to create polarization, while the amplitude was zero when the time derivative of the amplitude had a maximum magnitude, at which point the flows were fastest. $D^{EE}_{\ell,th}$ has less power than $D^{TT}_{\ell,th}$ and is more challenging to measure precisely. $D^{EE}_{\ell,th}$ has less power because the quadrupoles shown in figure 1.5 did not form easily. For example, for a quadrupole shown in the left image to form, photons from an overdense region needed to travel some distance to reach electrons located in the closest underdense region. However, some of the photons were not able to reach the electrons in the underdense region because the photons were scattered by other electrons during their travels. Although Thomson scattering of photons whose temperatures had quadrupole variations around electrons created the E-mode polarization, Thomson scattering also suppressed the formation of the quadrupoles.

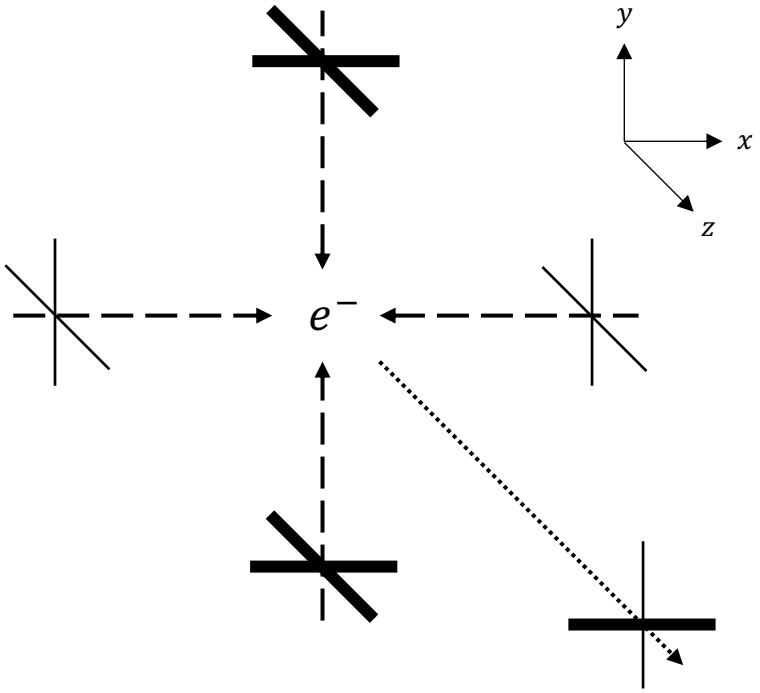

Figure 1.4. Polarization generated by a quadrupole variation in photon temperatures. In this diagram, unpolarized radiation approaches an electron from both $\pm x$- and $\pm y$-directions. The amplitudes of the electric fields along the two orthogonal directions perpendicular to each propagation direction of radiation are represented by the lengths of the two bars. The lengths are made to be the same to indicate that the radiation is unpolarized. The radiation from the $\pm y$-directions have higher temperature/intensity, which is represented by the thicker bars. The electron is thus surrounded by a quadrupole variation in photon intensities. When the electron scatters the incoming radiation from these directions, an observer in the z-direction sees polarized radiation that has higher intensity along the horizontal direction. This diagram was adapted from figure 1 of Hu and White [1997].

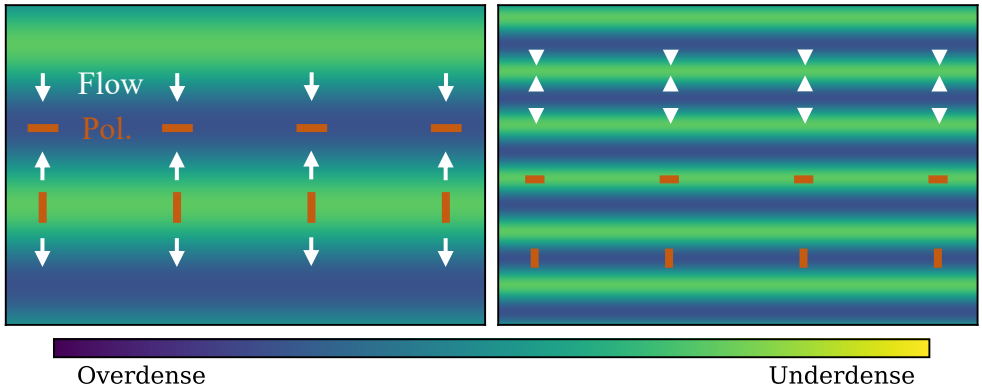

Figure 1.5. Quadrupole variations in the context of the standing-wave oscillations. The phase of the standing-wave oscillation shown on the left is such that the density fluctuations are not at extrema (no bright yellow and dark blue colors), but the amplitude of the wave is changing, so there are flows of photons, baryons, and electrons at different locations. The white arrows represent the flow directions at some locations. The fluid constituents are moving away from underdense regions and toward overdense regions. An electron located in an overdense region sees a quadrupole variation in photon intensities because photons coming from top and bottom have higher intensity than photons coming from left and right. The higher intensity is caused by the Doppler shift associated with the flows. For example, a photon coming from top is from a component of the fluid moving toward the electron, so the photon's intensity gets boosted. An electron located in an underdense region also sees a quadrupole variation, but the photons coming from top and bottom have lower intensity in this case. If the oscillation freezes at this point, radiation traveling out of the page that was scattered by electrons in overdense regions has horizontal polarization to some degree, which is represented by the horizontal red bars. For radiation coming from underdense regions, the polarization direction is vertical. The right panel shows another standing wave. This wave has the same density contrast as the one on the left, but its phase is such that the fluid constituents are moving away from overdense regions and toward underdense regions instead. Then, when the oscillation of this wave freezes at this point, the polarization direction from overdense regions is vertical and underdense regions horizontal. This figure was adapted from figure 10 of Hu and White [1997].

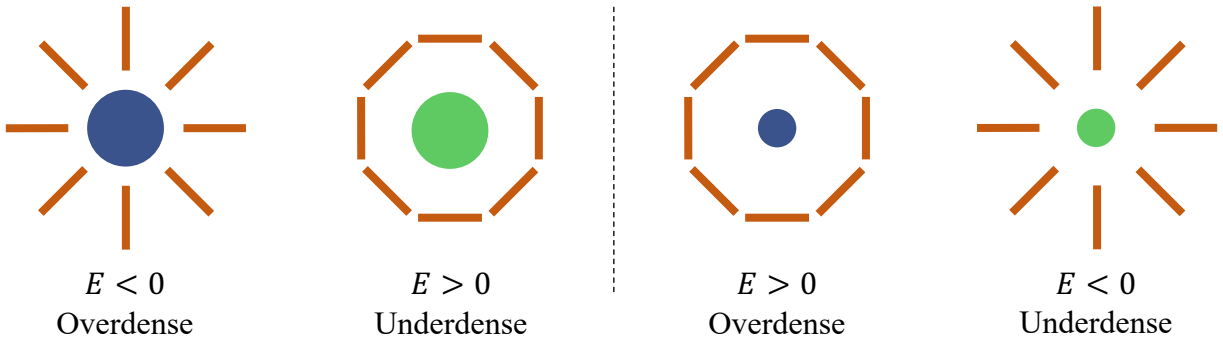

Figure 1.6. Characteristic patterns of the E-mode polarization. These patterns can arise when the rotated versions of the waves shown in 1.5 are superposed. For the wave shown on the left panel of that figure, superposing rotated versions of it creates a radial pattern around an overdense region and a tangential pattern around an underdense region. This is shown in the left half of this figure. For the wave shown on the right panel of 1.5, superposing rotated versions of it creates different polarization patterns as shown in the right half of this figure. By convention, a radial pattern is defined to have a negative E value, and a tangential pattern a positive value. This figure was adapted from figure 12 of Hu and White [1997].

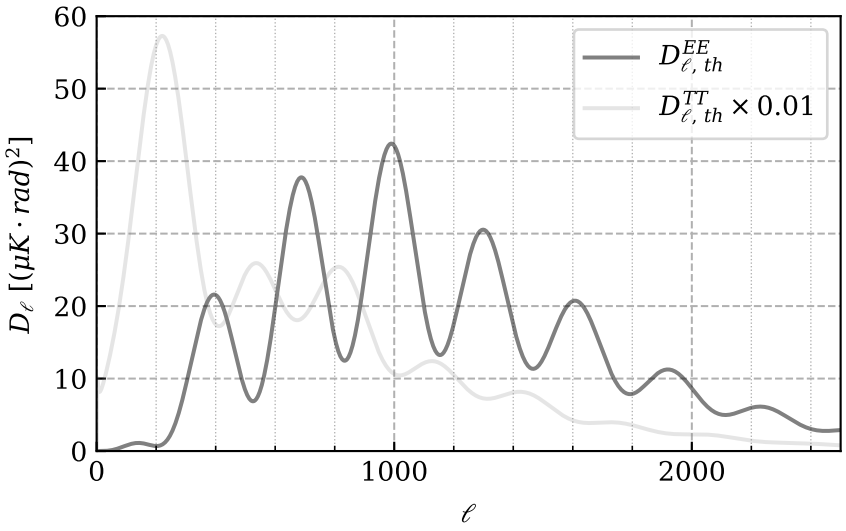

Figure 1.7. Theoretical angular power spectrum of the E-mode polarization anisotropy. A small copy (1%) of $D^{TT}_{\ell,\,th}$ is also shown so that the two spectra can be compared in the same figure.

1.3 Correlation Between the Two Types of Anisotropies

Besides $D_{\ell,th}^{TT}$, which can be roughly regarded as the square of the amplitude of a frozen standing-wave oscillation as a function of the wavelength, and $D_{\ell,th}^{EE}$, which can be regarded as the square of the time derivative of the amplitude, there is a third spectrum $D_{\ell,th}^{TE}$, which can be regarded as the product of the amplitude and its time derivative. $D_{\ell,th}^{TE}$ is also the spectrum of the cross-correlation between temperature and E-mode polarization anisotropy maps, while the $D_{\ell,th}^{TT}$ and $D_{\ell,th}^{EE}$ are autocorrelation spectra of the respective maps.

Figure 1.8 shows $D_{\ell,th}^{TE}$ along with $D_{\ell,th}^{TT}$ and $D_{\ell,th}^{EE}$. At ℓs where either $D_{\ell,th}^{TT}$ or $D_{\ell,th}^{EE}$ has a peak or trough, either the amplitude or its time derivative of a standing-wave oscillation was close to zero when it froze, so $D_{\ell,th}^{TE}$ is close to zero as well. Unlike $D_{\ell,th}^{TT}$ and $D_{\ell,th}^{EE}$, $D_{\ell,th}^{TE}$ has both positive and negative values. As shown in figure 1.6, an overdense region can have either positive or negative E-mode polarization. An overdense region generally corresponds to a high-temperature region, and an underdense region a low-temperature region, so the arrangements shown in the left half of figure 1.6 represent a negative correlation between the temperature and E-mode polarization, but the arrangements shown in the right half represent a positive correlation. At very low ℓs, however, an overdense region corresponds to a low-temperature region because of the Sachs-Wolfe effect, so the correlation is positive in that case.

In this thesis, I will use the phrase *the EE/TE/TT spectra of the anisotropies of the CMB* (or sometimes simply *the EE/TE/TT spectra*) to mean $D_{\ell,th}^{EE}$, $D_{\ell,th}^{TE}$, and $D_{\ell,th}^{TT}$, of which the anisotropies that we observe today are thought to be one random realization. Not only do these spectra have the peaks and troughs, they also have nontrivial envelopes of the peaks and troughs that are not simply constant. As one example, $D_{\ell,th}^{TT}$ still has nonzero power at its troughs. As another example, the first peak of $D_{\ell,th}^{EE}$ is much smaller than later peaks. Although very interesting and important, these effects will not be discussed here for

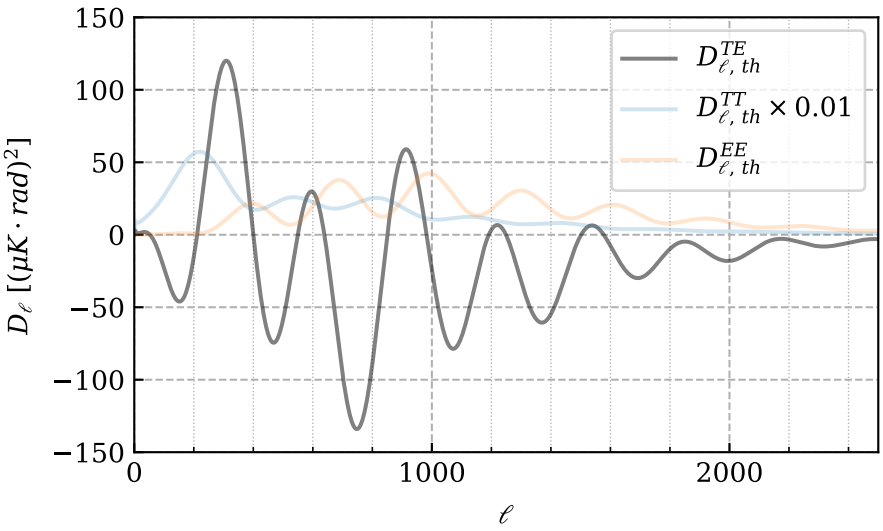

Figure 1.8. Theoretical temperature-E-mode cross-correlation spectrum. $D^{TT}_{\ell,th}$ and $D^{EE}_{\ell,th}$ are also shown so that the three spectra can be compared in the same figure.

simplicity. These effects and more details of the acoustic oscillations can be readily found in resources such as review papers (for example, Zyla et al. [2020], volume 1, chapter 29, and Hu and Dodelson [2002]).

1.4 Cosmological Parameters

The ΛCDM model is the current standard model of cosmology. In this model, matter and radiation were created at the beginning of the universe by some mechanism, which can be inflation or something else, and the universe has expanded since then according to general relativity with the FLRW metric (isotropic and homogeneous) that has Euclidean space. The expansion rate is governed by the types and energy densities of the components of the universe. The present age of the universe is 13.8 billion years, and dark energy (Λ) and cold dark matter (CDM) occupy a vast majority of the energy density of the universe (68% and 27%, respectively), while standard model particles (photons, neutrinos, electrons, protons,

and neutrons) occupy only 5%.

There are six basic parameters in the model, several derived parameters from the basic ones, and additional parameters associated with extensions of ΛCDM. A set of two parameters called A_s and n_s represent the amplitude and spectral index of the power spectrum of the initial density fluctuations of matter and radiation. Another set of two parameters called $\Omega_c h^2$ and $\Omega_b h^2$ represent the current densities of cold dark matter and baryons in the universe. Another parameter is called $100\theta_{MC}$, which is the ratio of two distances: the distance which the acoustic oscillations traveled from the beginning of the universe to the time when the CMB was formed (the standing waves discussed earlier can be regarded as sums of traveling waves) and the distance which the CMB photons traveled from the time when they were formed to the present day. The other parameter is called τ, which represents the fraction of CMB photons that were scattered by free electrons during the photons' travels to us. The free electrons were formed when the universe was reionized by first stars. An important parameter that can be derived from these six parameters is the Hubble constant, H_0, which is the current expansion rate of the universe. There also exist extension models of ΛCDM, one of which allows additional species of relativistic particles in early universe or other types of neutrinos by floating the effective number of types of neutrinos, N_{eff}, instead of fixing it at the value from the standard model.

The shapes of the $EE/TE/TT$ spectra of the anisotropies of the CMB (positions of the peaks and troughs, relative heights of the peaks, overall amplitudes and tilts of the spectra, and so on) are affected by the parameters of ΛCDM and its extensions. Therefore, these spectra can be used to constrain cosmological parameters. For example, figure 1.9 shows how the $EE/TE/TT$ spectra change as the dark matter density is decreased. Comprehensive discussions on cosmological parameters and how they affect the $EE/TE/TT$ spectra can be found in various papers such as Aghanim et al. [2020b] (section 3).

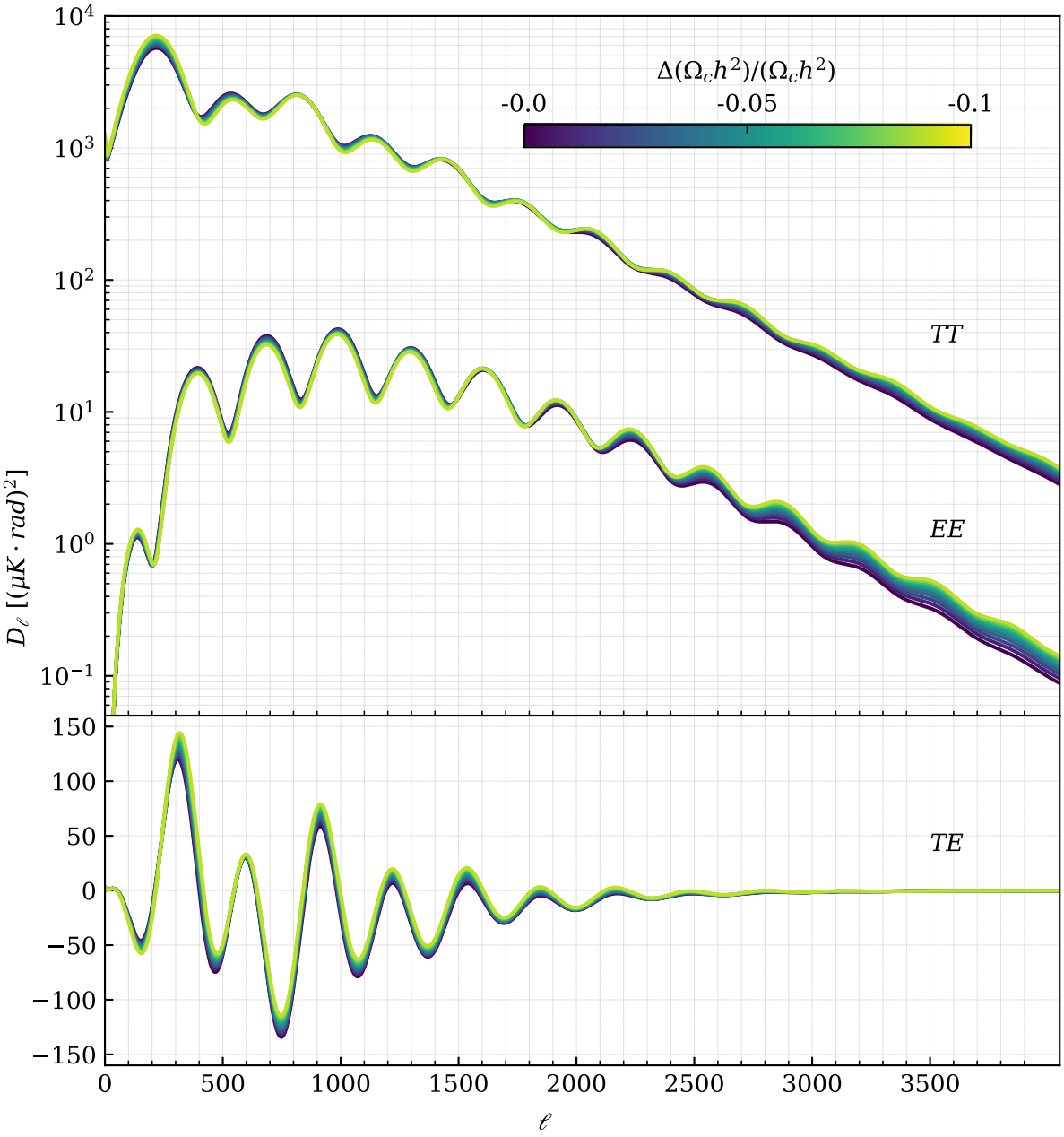

Figure 1.9. Dependence of the shapes of the spectra on the dark matter density. This figure shows how the $EE/TE/TT$ spectra change as the dark matter density is gradually decreased from the current best estimate to the value that is 10% lower than that. The total energy density of the universe and the density of dark energy were fixed, and a decrease in the dark matter density was compensated by an increase in the baryon density. The figure was created by adapting code from a tutorial by Zhaodi Pan.

1.5 Current Measurements

The $EE/TE/TT$ spectra of the anisotropies of the CMB have been measured by a large number of experiments, and the measurements have been fit well by ΛCDM. Figure 1.10 shows recent measurements by three experiments. One is the satellite *Planck*, and the other two are the ground-based telescopes the Atacama Cosmology Telescope (ACT) in Chile and the South Pole Telescope (SPT) in Antarctica. The measurements labeled as Planck were published in Aghanim et al. [2020a] and based on all the data from the experiment. The satellite collected data from 2009 to 2013. The measurements labeled as ACT DR4 were published in Choi et al. [2020] and Aiola et al. [2020] and based on the fourth data release from ACT, which included data from 2013 to 2016. New measurements based on data from more years are expected to be available soon. ACT was decommissioned in 2022, and a new telescope called Simons Observatory is being commissioned at the same site. The measurements labeled as SPTpol were published in Henning et al. [2018], and the measurements labeled as SPT-3G were published in Dutcher et al. [2021], Balkenhol et al. [2021], and Balkenhol et al. [2023]. SPTpol was the second-generation imaging instrument on SPT and was operated from 2012 to 2016. Henning et al. [2018] was based on data from three years, and new measurements based on all the data from the four years are expected to be available soon. SPT-3G is the third-generation imaging instrument and has been operated since 2017. The measurements shown here are based on data from 2018, and new measurements based on 2019 and 2020 are expected to be available soon. The figure also shows *Planck*'s best-fit theoretical spectra, which are based on a particular set of values for the six ΛCDM parameters. All the measurements have been generally fit well by ΛCDM.

Figure 1.11 compares the sizes of the uncertainties shown in figure 1.10 with the theoretical spectra and the irreducible uncertainties caused by the cosmic variance. As for the TT spectrum, *Planck* essentially reached the cosmic variance limit at ℓs below 1500 or so.

At these ℓs, the noise fluctuations in *Planck*'s temperature anisotropy map were small compared with the temperature anisotropy signals, and the uncertainties in the measurements of the TT spectrum were mostly from the cosmic variance. However, *Planck*'s uncertainties in its measurements of the TE spectrum were farther from the cosmic variance limit at those ℓs, and the distance from the cosmic variance limit was even larger as for the EE spectrum. This is because the E-mode polarization anisotropy signals are much weaker than the temperature anisotropy signals, and the noise fluctuations in *Planck*'s E-mode polarization anisotropy map were not negligible compared with the signals anymore, so the uncertainties in the measurements of the TE and EE spectra had sizable contributions from the noise fluctuations besides the cosmic variance. Nevertheless, *Planck* still achieved smaller uncertainties than ACT and SPT at relatively low ℓs. At higher ℓs, ACT and SPT achieved lower uncertainties than *Planck* because of higher-resolution and lower-noise maps produced by the ground-based experiments. There will be more discussions on what factors determine an experiment's uncertainties in section 2.4.

A note on the uncertainties shown in this figure: as will be discussed in subsections 3.3.6 and 4.4.2, experimental groups typically report binned measurements of the $EE/TE/TT$ spectra rather than data points at individual ℓs. The wider a bin, the smaller the fractional uncertainty in the binned measurement, Because different experiments used different bin sizes, to compare the uncertainties fairly, I multiplied the uncertainties from ACT and SPT by factors that account for the differences between their binning and *Planck*'s. For example, the size of each *Planck* bin is 30, but the size of each SPT-3G bin is 50 for ℓs below 2000 and 100 for ℓs above 2000. To take these differences into account, I multiplied the uncertainties in the SPT-3G low-ℓ and high-ℓ bins by $\sqrt{50/30}$ and $\sqrt{100/30}$, respectively.

Currently, the most precise constraints on the ΛCDM parameters are from *Planck*. It achieved fractional uncertainties at the level of subpercent in all the six parameters except for τ (Aghanim et al. [2020b], table 1). *Planck* derived most of its constraining power on the

parameters from its measurements of the TT and TE spectra at low ℓs. The uncertainties in the parameters achieved by ACT and SPT are larger than those achieved by *Planck* by a factor of a few (for example, Balkenhol et al. [2023], figure 7), but constraints from the two experiments are expected to become much stronger once more data are added.

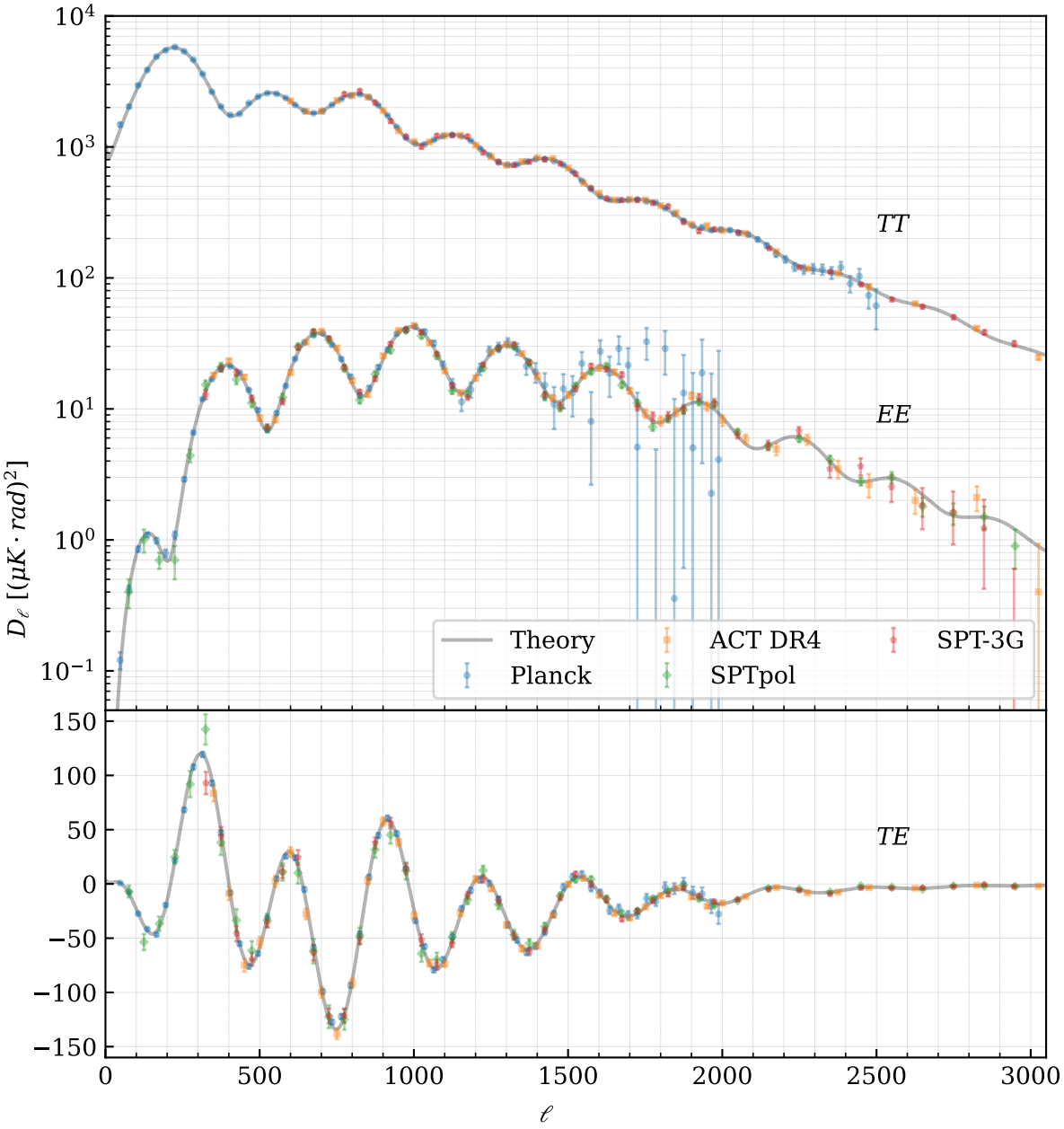

Figure 1.10. Measurements of the spectra by three experiments. The data points were taken from NASA LAMBDA Archive.

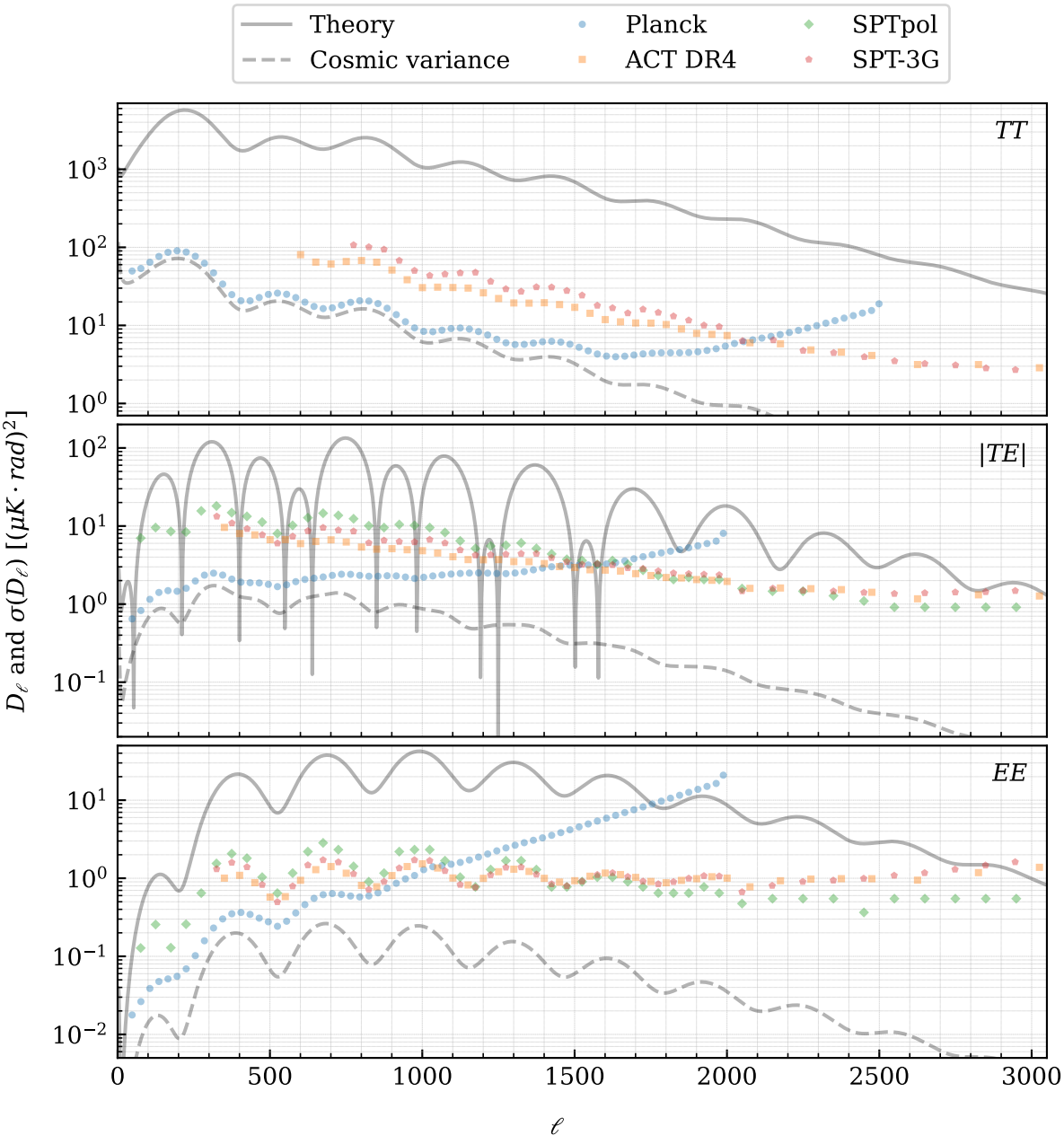

Figure 1.11. Measurement uncertainties achieved by the three experiments.

1.6 Future Directions

Although *Planck* achieved impressive constraints on the ΛCDM parameters, and ΛCDM has been successful in describing CMB measurements and measurements of other cosmological phenomena, there are also challenges to ΛCDM.

A major challenge is the so-called Hubble tension, which is the name for discrepancies among measurements of the Hubble constant obtained in different ways. On the one hand, the Hubble constant can be estimated by observing the conditions in the early universe revealed by the CMB anisotropies, evolving the universe from that time to the present day using ΛCDM, and predicting what the current expansion rate of the universe should be. On the other hand, the Hubble constant can also be directly estimated by measuring how fast nearby galaxies are receding. CMB experiments have typically obtained lower values for the Hubble constant than the other class of experiments. For example, while *Planck* reported 67.4 ± 0.5 km/s/Mpc, the SH0ES program, an experiment that observed supernovae in nearby galaxies, reported 73.04 ± 1.04 km/s/Mpc (Riess et al. [2022]).

An important goal of current and future CMB experiments is to measure the E-mode polarization anisotropy with increasing accuracy and precision. As shown in figure 1.11, there is still a lot of room for improvement in the measurements of the TE and EE spectra. If measured sufficiently precisely, the E-mode polarization anisotropy is expected to have stronger constraining power of cosmological parameters than the temperature anisotropy (Galli et al. [2014]). Better measurements of the polarization will serve as a powerful consistency test of the existing constraints on the ΛCDM parameters and potentially provide hints of new physics. Regarding the Hubble constant, CMB experiments have reported that values of the Hubble constant determined by using only measurements of the EE spectrum were higher than values obtained from the TE and TT spectra but not at statistically significant levels (Dutcher et al. [2021], figure 13). Better measurements of the EE spectrum in the future

should be able to shed more light on this interesting trend.

The CMB anisotropies discussed in this chapter were created by the acoustic oscillations of the photon-baryon fluid. Any anisotropy that was created before the photons decoupled from the fluid is called primary anisotropy. There also exist secondary anisotropies (the Sunyaev-Zel'dovich effects, gravitational lensing of the CMB photons, and so on), which were caused by interactions between the CMB photons and other components of the universe after the photons decoupled from the fluid and started to travel toward us. Regarding primary anisotropies, the B-mode polarization anisotropy is also very important. However, these other important signals will not be discussed in this thesis, and I will use the phrase *the anisotropies of the CMB* to mean only the primary anisotropies created by the acoustic oscillations.

CHAPTER 2

SPT-3G

The South Pole Telescope (SPT) is a CMB experiment and has been running since 2007. It is located at the Amundsen-Scott South Pole Station, which is one of the best locations on earth for CMB observations because of the extremely dry and stable atmosphere at the south pole. One of the current goals of SPT is to make low-noise measurements of the E-mode polarization anisotropy and thereby better constrain cosmological parameters.

The SPT-3G camera is the current imaging instrument on the telescope and has been used to take data since 2017. I have worked on analyzing SPT-3G data throughout my graduate career. I worked on low-level data analysis projects between late 2017 and early 2020 and started my thesis project in early 2020. The low-level data analysis projects will not be discussed in this thesis, but I discussed some highlights during my thesis defense, and I will be very happy to share slides and/or a recording of the presentation upon request. The thesis project will be discussed in chapters 3 and 4.

In the following sections of this chapter, I will provide an overview of the telescope and the camera, show example raw data from the camera, and discuss how SPT complements *Planck*.

2.1 South Pole Telescope

Figure 2.1 is a photograph of the telescope and shows its notable primary mirror. The diameter of the mirror is 10 m, which determines the angular resolution of the telescope to be approximately one arc minute at 150 GHz, the frequency where the blackbody spectrum of the CMB peaks. SPT has the largest primary mirror and highest resolution of all the currently operating dedicated CMB telescopes.

As annotated in the figure, the telescope motions have two degrees of freedom: the az-

imuth and elevation angles. Because of the unique location of the south pole, the two coordinates of the equatorial coordinate system, right ascension and declination, map onto the azimuth and elevation angles in simple ways. Declination is the negative of the elevation angle. Right ascension is the same as the azimuth angle except that the former is fixed in the celestial sphere, and the latter is fixed on the ground and rotates with respect to the former.

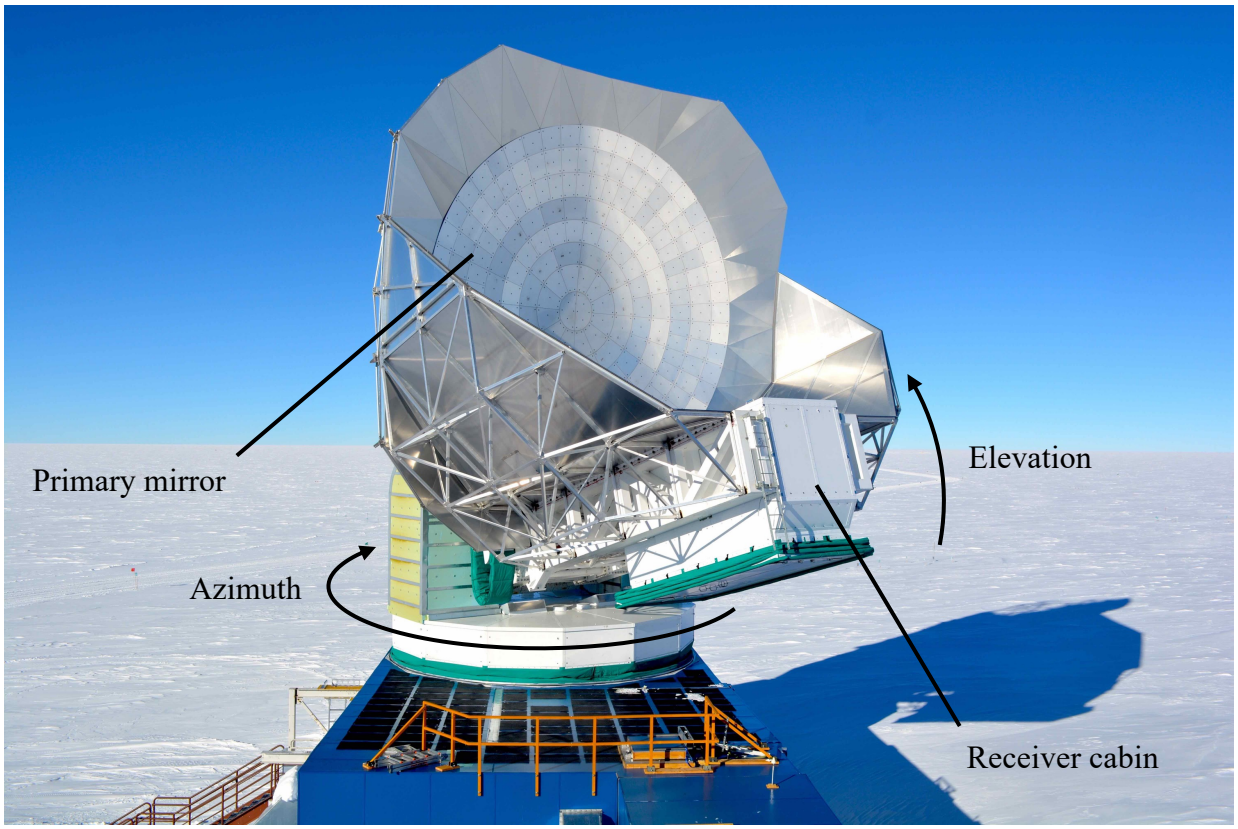

Figure 2.1. Photograph of SPT taken during the 2017–2018 austral summer. Photographers: Amy Bender and Brad Benson.

2.2 Third-Generation Camera

Three generations of imaging instruments have been housed inside the receiver cabin of the telescope (annotated in figure 2.1), and the currently operating, third-generation instrument

is called SPT-3G. SPT-3G was installed in the 2016–2017 austral summer, and it was a significant upgrade from the second-generation instrument, SPTpol, by having 10 times more detectors. The detector count increased from approximately 1500 to 16000. Much work was done in 2017 to characterize the instrument. In 2018, we had a good start by taking high-quality data during the first month of our observing season, but an unexpected mechanical issue with the telescope caused a severe interruption. However, we were still able to resume taking data later in the year. Since 2019, we have been taking data consistently without any major issues, and we will continue taking data for at least a few more years.

Our general observing strategy is to focus on small areas of the sky and observe them repeatedly to make low-noise measurements of the CMB anisotropies in those areas. Because the CMB does not change on the timescale of human lives. as we observe the same areas of the sky repeatedly and combine maps of the CMB made from different observations, the CMB stays the same in a combined map, and the noise in the map decreases over time. Different observations have uncorrelated noise, so the cumulative noise decreases as the inverse of the square root of the number of observations. Given the unique location of the south pole, an area of the sky that is visible at one time is always visible and does not rise or set. This is advantageous to our observing strategy. The areas of the sky that we have mainly observed for the past five years are shown in figure 2.2. Between late March and late November of each year, we observed the blue patch, which we call the winter field. The winter field has very low level of emission from the Milky Way. In other months, the sun was too close to the winter field, so we observed different areas, which we call the summer fields.

Simplistically speaking, our detectors are very sensitive thermistors that convert changing intensity of incident radiation from the sky into changing electrical power dissipated on the detectors. Radiation from the sky is reflected off the primary mirror and goes into a cryogenic camera inside the receiver cabin. After passing through a series of lenses inside the camera, the radiation couples to arrays of pairs of orthogonal antennae lithographed onto

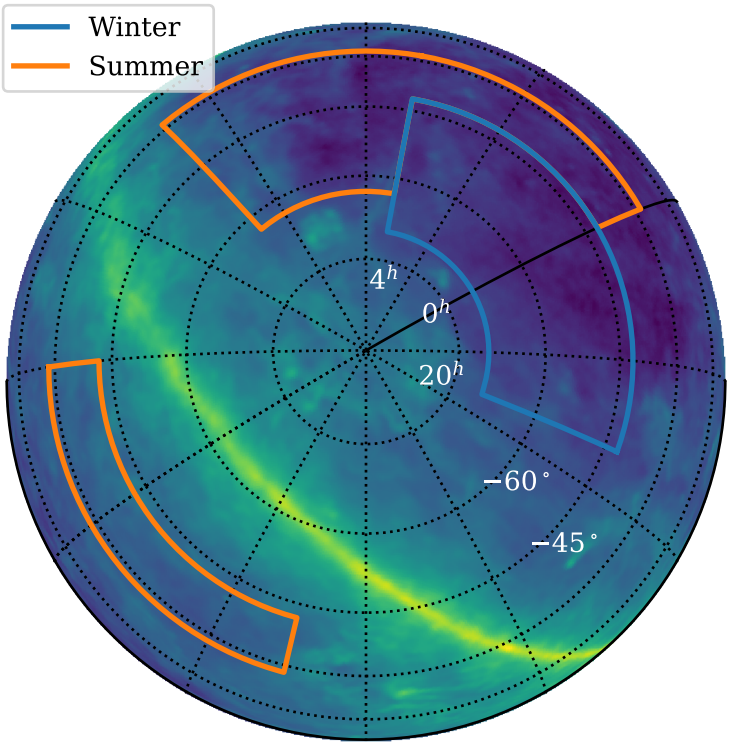

Figure 2.2. Winter and summer fields. The color map represents *Planck*'s measurements of the emission from the dust of the Milky Way.

silicon wafers. The two orthogonal antennae in a pair are for two orthogonal polarization directions. Electromagnetic waves generated by each antenna are split into waves in three frequency bands, delivered to three island structures through transmission lines, terminated at the islands, and converted into heat. There are 10 wafers in total, and each wafer has an array of 269 pairs of antennae. The three frequency bands are centered at 95, 150, and 220 GHz. There are approximately 16 000 sensors in total, and each one-third is for one frequency band. Figure 2.3 has photographs of the antenna arrays and some of the island structures. Each island structure contains a thin metal film called a transition-edge sensor. The sensor is maintained at its superconducting-to-normal transition temperature (approximately 500 mK), where its resistance changes sensitively in response to slight variations in its temperature. We apply a constant voltage to each sensor. As the incident radiation from

the sky changes, the heat delivered to an island also changes, which changes the resistance of the sensor, which in turn changes the electrical current running through the sensor and the electrical power dissipated on it. When the intensity of the radiation increases, the island's temperature increases. This then increases the resistance of the sensor and decreases the electrical power dissipated on it. Similarly, a decrease in the intensity of the radiation causes an increase in the electrical power. As we scan the telescope across an area of the sky, we measure the electrical power dissipated on each sensor over time and thereby infer the intensity of the incident radiation at different locations in the sky within the area. Detailed descriptions of components of the camera and operating principles of the sensors can be found in Sobrin et al. [2022]. In later sections, I will use the word *detector* to mean an antenna and one of the three sensors connected to it.

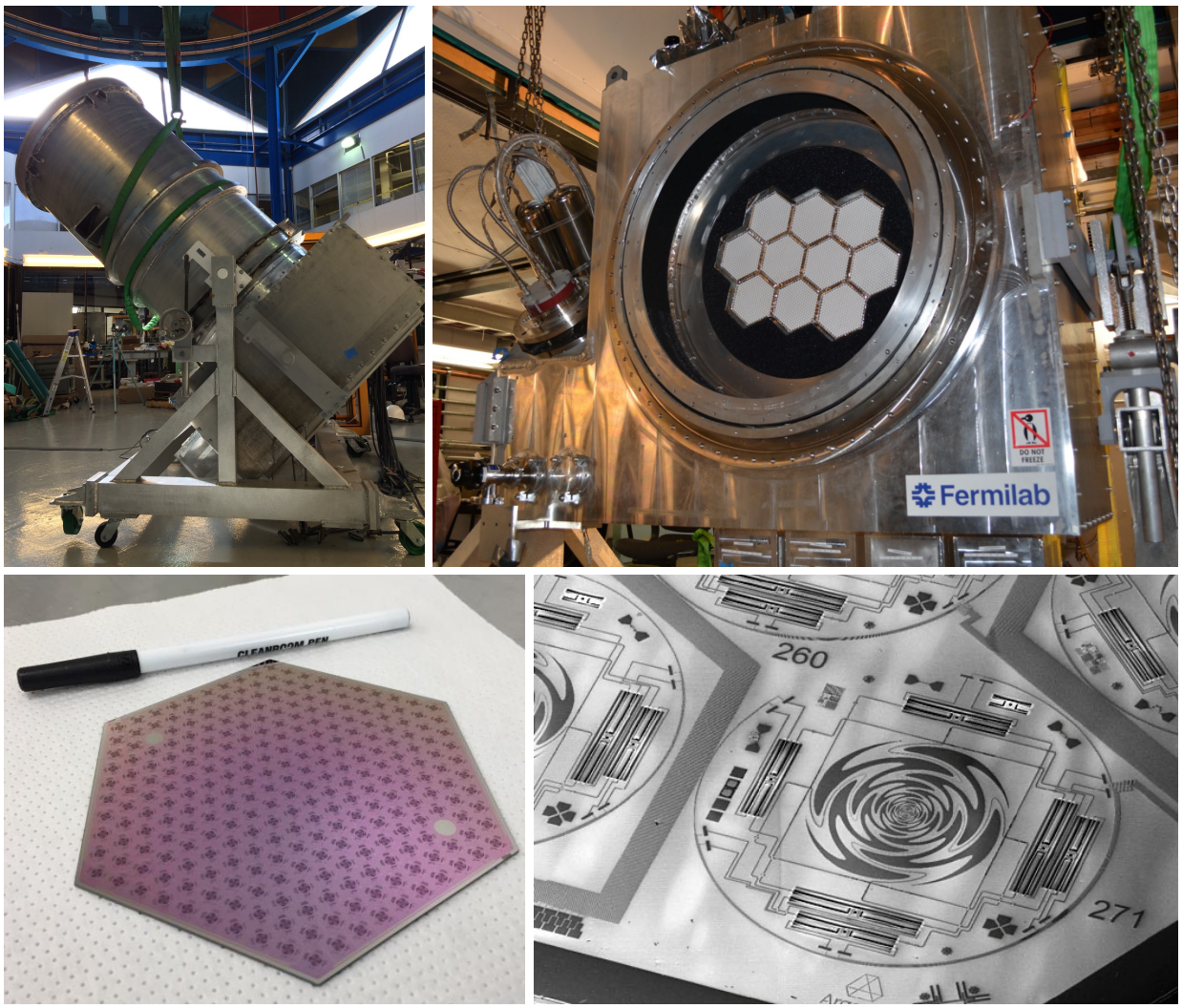

Figure 2.3. Photographs of components of SPT-3G. The top left photograph shows the outside of the cryogenic camera. The top right photograph shows the inside of the camera when the optics tube shown in the top left photograph is removed. Photographers of these images: Amy Bender and Brad Benson. Each wafer shown in the top right image is covered by an array of small dome-shaped lenses. Beneath the lenses is an array of antennae, which is shown in the bottom left photograph. Photograph source: Dutcher et al. [2018]. The bottom right photograph shows one pair of sinuous antennae that are sensitive to orthogonal polarization directions and the six island structures (two polarization directions for each of the three frequency bands) connected to them. Photograph source: Posada et al. [2016].

2.3 Example Raw Data

Raw data from SPT-3G are time series of the electrical power dissipated in each detector and time series of the telescope's azimuth and elevation angles. We call a time series a timestream.

Figure 2.4 shows the timestream of one detector and the timestreams of the azimuth and elevation angles of the telescope during the entirety of a calibration observation, in which we scanned the telescope across an astrophysical source that has known brightness and recorded each detector's response to the source. Figure 2.5 shows the same timestreams from only a short period of that observation. The bottom panel of figure 2.4 shows that the electrical power dissipated on the detector had an increasing trend. This means that the detector received less radiation from the sky over time. The main source of the radiation received by a detector is the microwave emission from the atmosphere. As the telescope's elevation increased over time, the detector received the microwave emission from a thiner column of the atmosphere. The decreased intensity of the incident radiation resulted in the increased electrical power dissipated on the detector (a phenomenon discussed in section 2.2). However, during one part of the observation, the timestream also had many downward spikes. These spikes happened when the detector received the radiation from the astrophysical source and can be seen more clearly in figure 2.5. Figure 2.5 also shows the scanning pattern of the telescope, which is a raster. We scan the telescope back and forth in the azimuth while maintaining the same elevation, increases the elevation by a step, conduct another pair of scans in the azimuth, increases the elevation by another step, and so on.

Figure 2.6 shows timestreams from multiple detectors during one scan of an observation of the winter field. A detector's timestream during one scan is dominated by the atmospheric emission. Within each frequency band, timestreams from different detectors are highly correlated because the detectors observe common atmospheric fluctuation patterns. Furthermore, there is a high degree of interfrequency correlation between timestreams in the 150 and 220

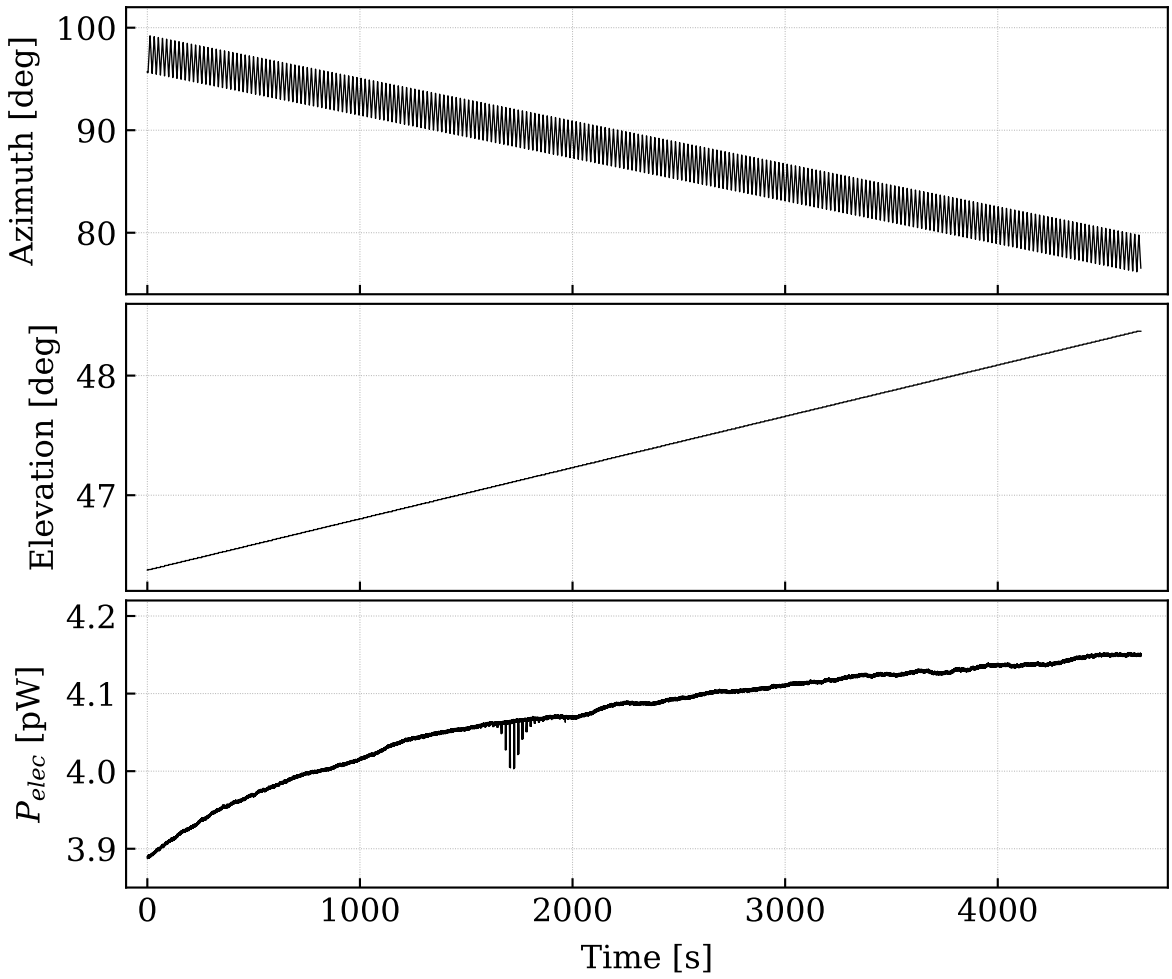

Figure 2.4. Timestreams from a calibration observation (the full length).

GHz bands as well because the two frequency bands are adjacent to the two sides of an H_2O emission line at around 185 GHz.

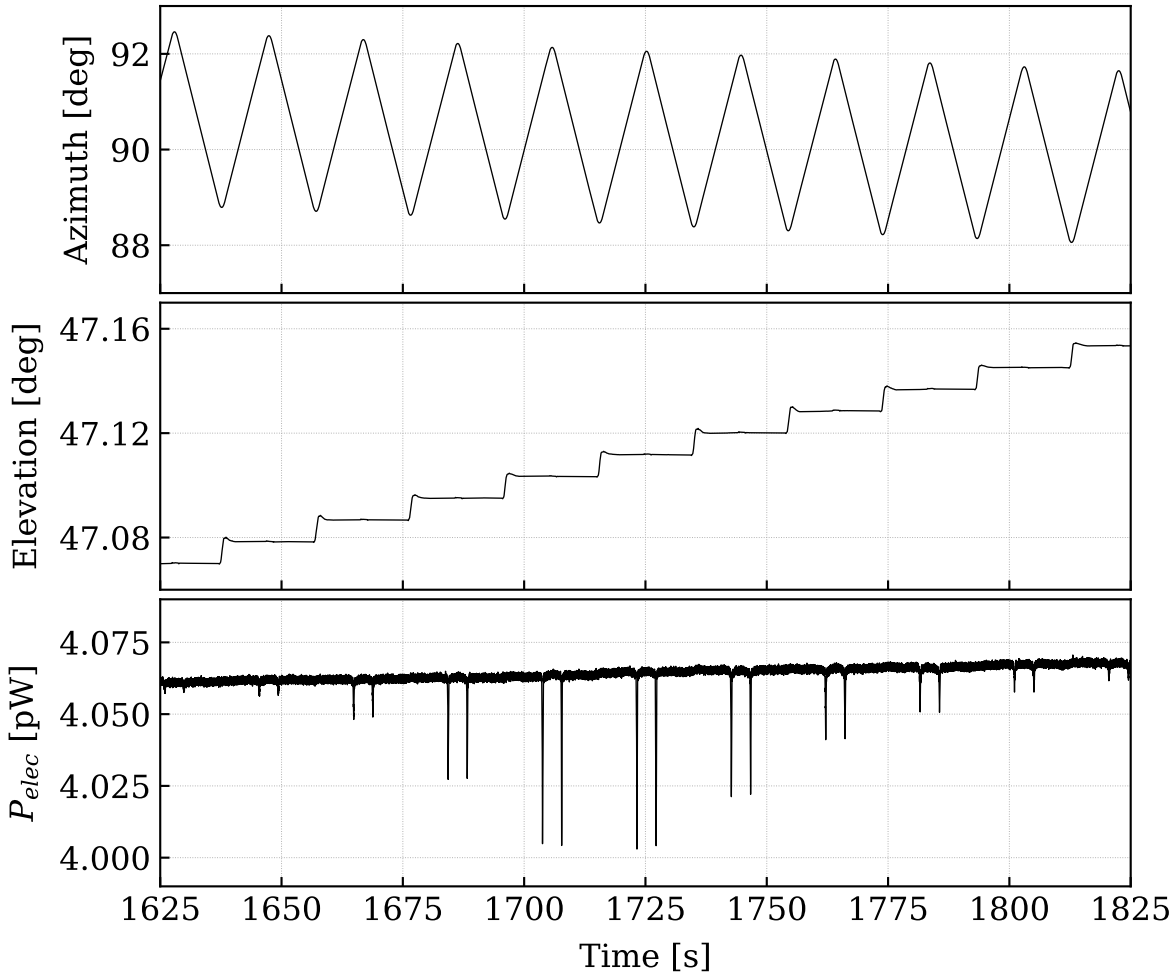

Figure 2.5. Timestreams from a calibration observation (a short period). The downward spikes in the detector timestream formed pairs because the detector responded to the astrophysical source twice in a pair of increasing-azimuth and decreasing-azimuth scans.

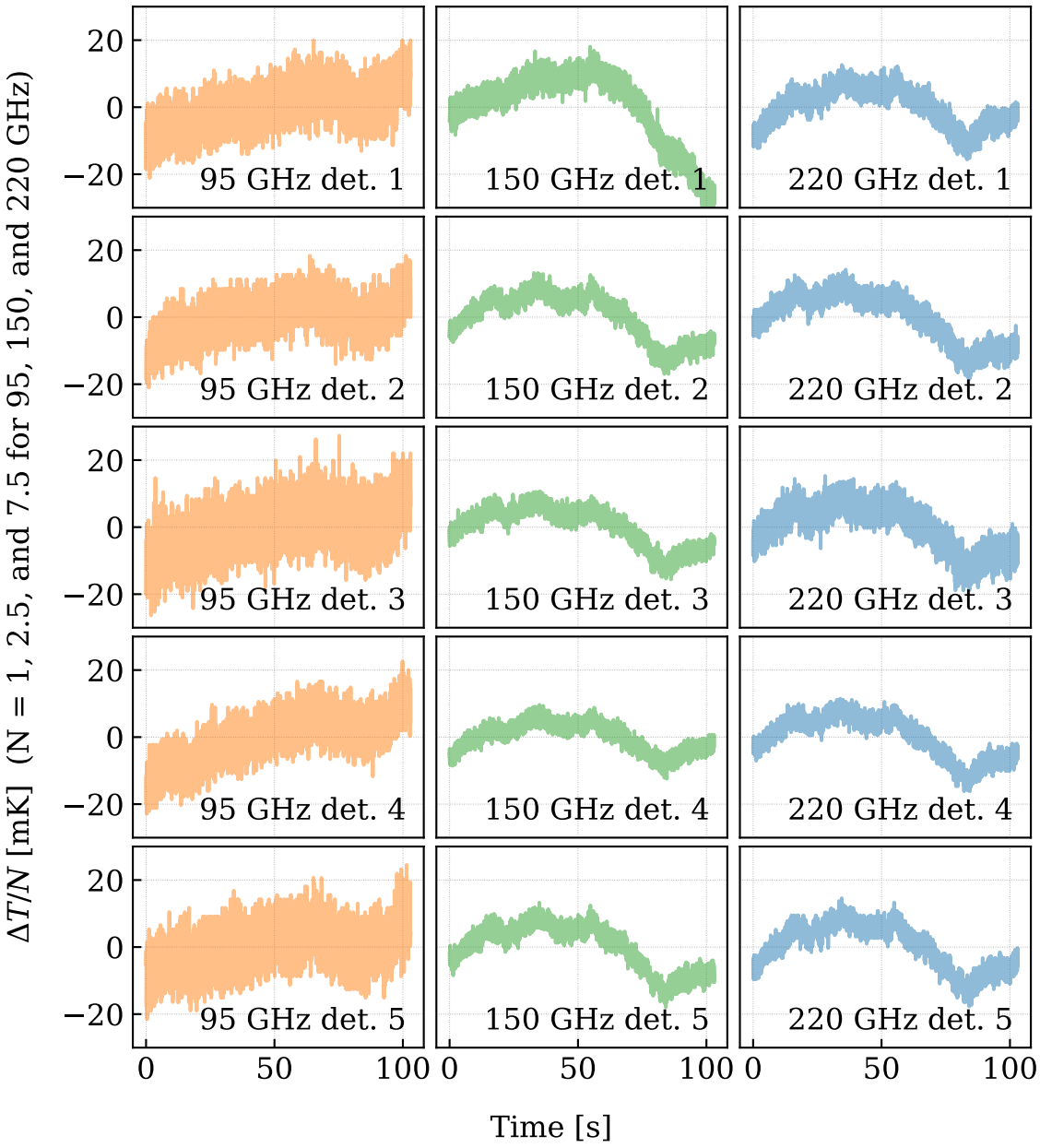

Figure 2.6. Detector timestreams from one scan of a field observation. For each frequency band, five timestreams of randomly chosen detectors on different wafers are shown. Each timestream's mean was subtracted, and its unit was converted from ΔP_{elec} to ΔT. As indicated in the y-axis label, the timestreams from each frequency band were also divided by a different normalization factor so that the timestreams from the different frequency bands could be shown on the same y-axis scale easily.

2.4 Complementarity

SPT-3G and *Planck* are complementary to each other. While *Planck* made more precise measurements of the $EE/TE/TT$ spectra of the anisotropies of the CMB at relatively low ℓs (large angular scales) and derived their constraining power on cosmological parameters from those ℓs, we are making more precise measurements at relatively high ℓs (small angular scales) with SPT-3G. We expect to be able to constrain some cosmological parameters, including the Hubble constant, with higher precision than *Planck* by eventually using all the data from the camera.

A very useful formula called the Knox formula (Knox [1995], equation A11) can approximately predict uncertainties in measurements of the $EE/TE/TT$ spectra that can be achieved by an experiment given some basic properties of the experiment. As for the EE spectrum, the formula is the following:

$$\sigma(C_\ell^{EE}) = \sqrt{\frac{2}{(2\ell+1)\, f_{sky}}}\,(C_\ell^{EE} + N_\ell^{EE}), \tag{2.1}$$

where f_{sky} is the fraction of the full sky observed by the experiment, and N_ℓ^{EE} is the angular power spectrum of the noise fluctuations in the E-mode polarization map produced by the experiment. Equation 2.1 is a modified version of equation 1.3 and incorporates two additional effects. One effect is that the noise of an instrument worsens the uncertainties, and the other effect is that observing a limited area of the sky decreases the effective number of spherical harmonic modes observed and thus worsens the uncertainties. The number of available modes would be $2\ell + 1$ at each ℓ if the CMB at every location in the sky could be observed. In reality, the presence of the plane of the Milky Way and the strategy of an experiment inevitably make f_{sky} smaller than 1.0, and the effective number of observed modes at each ℓ becomes $(2\ell + 1)f_{sky}$. This reduction in observed modes is another source of sample variance besides the cosmic variance discussed in section 1.1.

Figure 2.7 shows the predictions of equation 2.1 for two hypothetical experiments and shows how the two experiments complement each other. Experiment A observes a small area of the sky ($f_{sky} = 0.04$) for a certain period of time to obtain low-noise measurements of the CMB. The noise in its E-mode polarization map is assumed to be white noise, so N_ℓ^{EE} is simply a constant. (In the D_ℓ convention, the noise spectrum increases as the square of ℓ.) Experiment B has the identical instrument but observes a large area of the sky ($f_{sky} = 0.60$) within the same period of time, so it spends less time per unit area than A and obtains noisier measurements per unit area. It has 15 times higher N_ℓ^{EE} than the other experiment. At relatively low ℓs, where both experiments' noise spectra are lower than the signal spectrum, observing more area is more effective in obtaining smaller uncertainties than having lower noise. On the other hand, at relatively high ℓs, where the noise spectra are higher than the signal spectrum, having lower noise is more effective than observing more area.

Experiment A in this example was meant to represent SPT-3G, and experiment B *Planck*. While *Planck* was a satellite experiment with a small aperture (approximately 1.5 m) that observed the full sky, SPT-3G is big ground-based experiment focusing on small areas of the sky. The example above does not include the effect of the resolution of an experiment, which is that lower resolution causes more worsening of the noise spectrum as ℓ increases. Making high-resolution and low-noise maps of the CMB at small angular scales is a major strength of SPT in the landscape of CMB experiments.

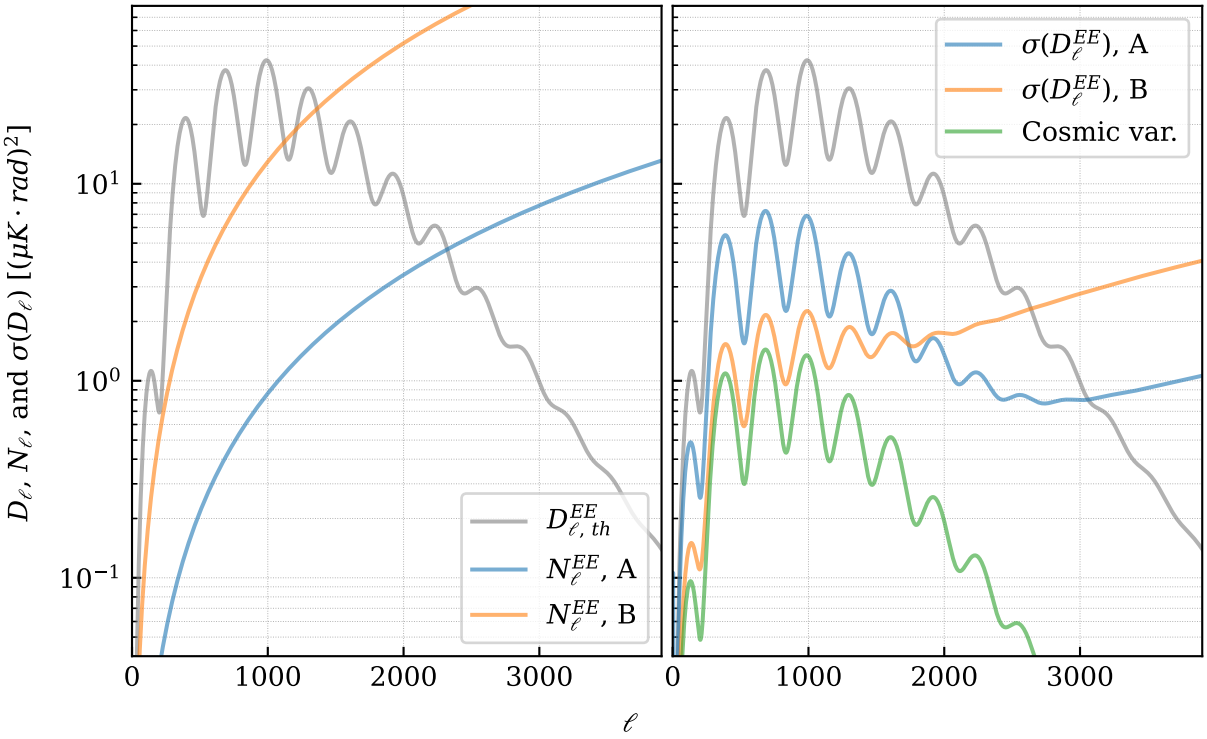

Figure 2.7. Uncertainties predicted by the Knox formula for hypothetical experiments. Both panels show the same theoretical EE spectrum as the gray curves. The left panel shows two experiments' noise spectra, and the right panel shows the the expected uncertainties in their measurements of the EE spectrum. The cosmic variance limit (a version of equation 1.3 for the EE spectrum) is also shown in the right panel.

CHAPTER 3

DATASET AND METHODS

The aims of my thesis project are to substantially improve SPT's most recent measurements of the EE/TE spectra of the anisotropies of the CMB and constraints on cosmological parameters by analyzing the data that we took during the 2019 and 2020 winter observing seasons with SPT-3G and to prepare for a future analysis that will use all the data from SPT-3G. I have been co-leading this analysis since April 2020. In the following sections of this chapter, I will introduce the 2019–2020 winter dataset and discuss the methods that we used or will use in each major step of the analysis.

3.1 2019–2020 Dataset

SPT's most recent measurements of the $EE/TE/TT$ spectra of the anisotropies of the CMB and constraints on cosmological parameters were based on the data taken during the 2018 winter observing season (Dutcher et al. [2021], Balkenhol et al. [2021], and Balkenhol et al. [2023]), and the 2018 winter dataset is approximately 8 times smaller than the 2019–2020 winter dataset. In 2018, we were able to take data for only half the season with only approximately 6600 detectors. For each winter since 2019, we were able to take data for the entire season with approximately 12 000 detectors, so the data volume from each winter since 2019 is approximately 4 times larger than the data volume from winter 2018. Therefore, the 2019–2020 winter dataset is approximately 8 times larger than the 2018 dataset.

The 2019–2020 winter dataset comprises many repeated observations of subareas of the winter field. Figure 3.1 is another representation of the winter and summer fields introduced in section 2.2. This figure shows how the winter and summer fields are divided into their subfields. As for the winter field, it is divided into four subfields, each of which spans the same range of right ascension as the full field but spans only one-fourth of the range of

declination spanned by the full field. If we were to make a detector observe the entire field without interruption, there would be too big of a change in the optical power incident on the detector caused by too big of a change in declination and therefore the thickness of the atmosphere seen by the detector. This would cause the detector to move out of its normal-to-superconducting transition at some point during the observation and would make the detector unusable. To avoid this issue, we observe only one subfield at a time and readjust a detector's position in the transition before we start observing another subfield. One observation of a subfield lasts for approximately two hours and comprises 36 pairs of increasing-azimuth and decreasing-azimuth scans. Each scan lasts for approximately 100 seconds and covers approximately 100 degrees in right ascension.

During the two seasons, in total we conducted 1047, 908, 788, and 591 observations of the el0, el1, el2, and el3 subfields, respectively. Although the duration of one observation is the same regardless of which subfield is observed, different subfields have different areas, so the observation time per unit area is longer for a smaller subfield in one observation. To ensure that the total observation time per unit area is uniform across the entire field, we conducted more observations of the larger subfields.

The vast majority of the observations had good data quality. Out of the 3334 observations that we conducted in total, we had to discard only 48 observations because of occasional issues with our data acquisition system. For each good observation and each scan, we assessed the quality of each detector's timestream against several criteria: whether the detector was operating in its normal-to-superconducting transition, whether the timestream had large discontinuities, whether the detector showed good optical response during a calibration observation that preceded the subfield observation, and so on. We found that 10 729 detectors passed these data quality cuts and that 831 detectors did not pass the cuts on average. All the timestreams from these good detectors then formed the input of this analysis.

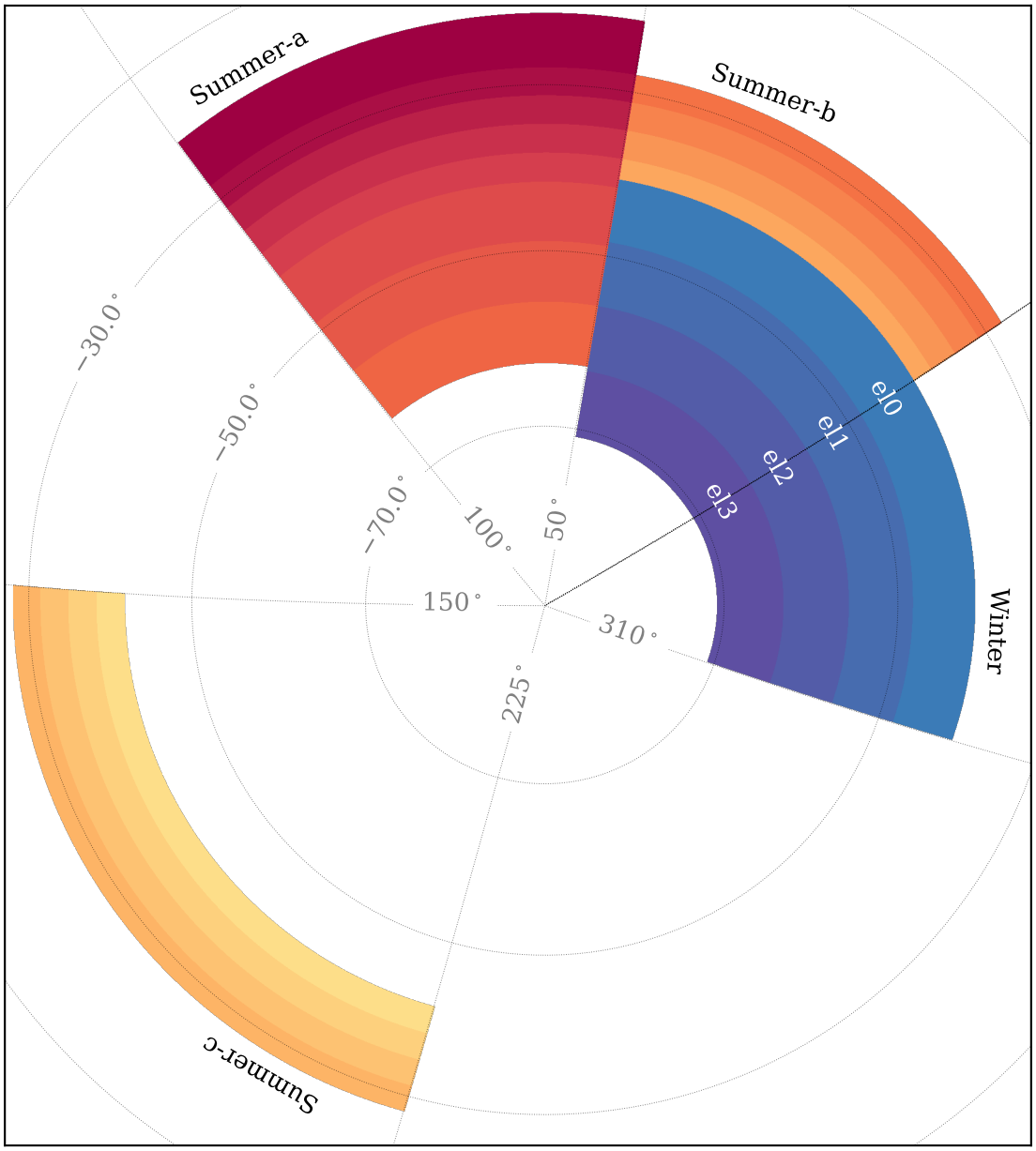

Figure 3.1. Subfields of the winter and summer fields. The winter field covers approximately 4% of the full sky (1650 deg^2). The field approximately spans 100° in right ascension (from $20^{\mathrm{h}}40^{\mathrm{m}}0^{\mathrm{s}}$ to $3^{\mathrm{h}}30^{\mathrm{m}}0^{\mathrm{s}}$) and 28° in declination (from −42° to −70°). It is split into four subfields called el0, el1, el2, and el3. Each subfield spans the same range of right ascension as the full field but spans only approximately 7° in declination. Each of the summer fields is divided into subfields in similar ways as shown by the color gradients.

3.2 From Timestreams to Maps

This analysis can be roughly divided into the following three major steps: making maps from the timestreams, calculating spectra from the maps, and constraining cosmological parameters from the spectra. In the following sections, I discuss what methods we used in the first two steps and what methods we plan to use in the third step.

In this section, I discuss a simplified maximum likelihood method of making maps from timestreams. I discuss what the likelihood function is, what simplification we make to obtain a solution, and how we processed all the timestreams in this dataset given that solution.

3.2.1 Likelihood Function

The parameters that we estimate from the simplified maximum likelihood method are the I, Q, and U Stokes parameters in each pixel within a field and each frequency band. The I parameter in one pixel and one frequency band represents the total intensity of the radiation coming from that location in the sky in that frequency band, and the Q and U parameters quantify the linear polarization intensity. Figure 3.2 shows how these Stokes parameters are expressed in relation to the components of the electric field vector of the radiation in a conventional coordinate system. The E-/B-mode polarization in a pixel are not quantities directly measurable by our detectors; rather, first we measure the Q and U parameters, and then we construct the E-/B-mode polarization from them.

One detector measures a linear combination of the three Stokes parameters in one frequency band. If a hypothetical noiseless detector is designed to measure the intensity along the direction that makes an angle ψ_α from north, then this intensity, I_α, can be expressed

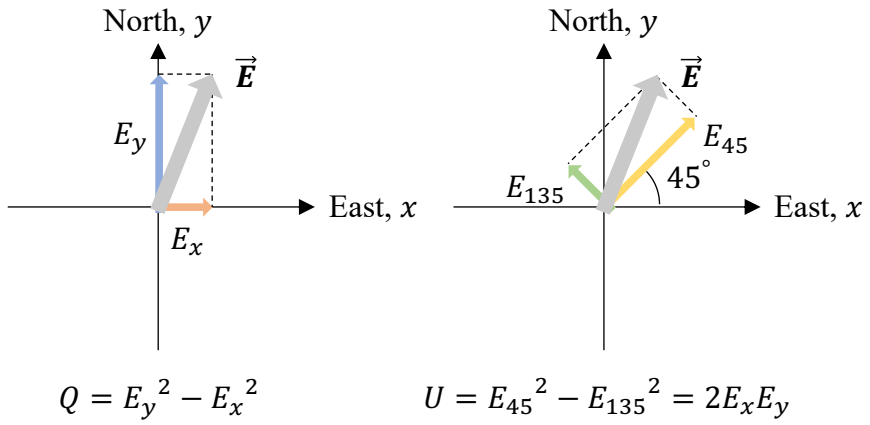

Figure 3.2. Expressions for the Stokes parameters. In this diagram, the thick gray arrow represents the electric field vector (at one instant) of some radiation coming from a certain location in the sky. The directions of the x-axis and y-axis used to decompose the vector are conventionally taken to be north and east. The Q Stokes parameter is the difference between the intensity along the north–south direction and the intensity along the east–west direction averaged over many periods of the oscillations of the field, so $Q = {E_y}^2 - {E_x}^2$. Here I omitted constants like c and ϵ_0 and the time average symbols for simplicity. The U Stokes parameter is the difference between the intensity along the northeast–southwest direction and the intensity along the northwest–southeast direction, so $U = 2E_xE_y$. The I Stokes parameter is equal to ${E_y}^2 + {E_x}^2$.

as follows:

$$\begin{aligned} I_\alpha &= (E_y \cos\psi_\alpha + E_x \sin\psi_\alpha)^2 \\ &= \frac{1}{2}\left[{E_y}^2 + {E_x}^2 + ({E_y}^2 - {E_x}^2)(\cos^2\psi_\alpha - \sin^2\psi_\alpha) + 2\,E_y\,E_x \cdot 2\cos\psi_\alpha \sin\psi_\alpha\right] \\ &= \frac{1}{2}\left(T + Q\cos 2\psi_\alpha + U \sin 2\psi_\alpha\right). \end{aligned} \tag{3.1}$$

Here, I used the symbol T instead of I because I have used the word *temperature* for the total intensity of the CMB.

Once multiple detectors in the same frequency band with different angles measure the

radiation coming from a pixel, pretending that other pixels and frequency bands do not exist for a moment, we can construct a likelihood function for the Stokes parameters of that pixel and find the maximum likelihood solution. The likelihood function, L, has the following form:

$$L \propto exp\,[\,-(M - AS)^T\, V^{-1}\,(M - AS)\,], \tag{3.2}$$

where

$$M = \begin{pmatrix} I_\alpha \\ I_\beta \\ I_\gamma \\ \vdots \end{pmatrix},\ A = \frac{1}{2}\begin{pmatrix} 1 & cos\,2\psi_\alpha & sin\,2\psi_\alpha \\ 1 & cos\,2\psi_\beta & sin\,2\psi_\beta \\ 1 & cos\,2\psi_\gamma & sin\,2\psi_\gamma \\ \vdots & \vdots & \vdots \end{pmatrix},\ S = \begin{pmatrix} T \\ Q \\ U \end{pmatrix}. \tag{3.3}$$

The symbol V represents the covariance matrix of the measurements from the multiple detectors, and Gaussian noise is assumed for every measurement. Given this likelihood function, the values of the Stokes parameters that maximize the function are given by the following equation:

$$S = (A^T\, V^{-1} A)^{-1} (A^T\, V^{-1} M) \tag{3.4}$$

(Couchot et al. [1999]).

3.2.2 Simplification

The likelihood function introduced above is in fact only a minute part of our complete likelihood function because there are many pixels within a field and many multifrequency measurements on each pixel. For this analysis, the number of pixels within the winter field is $O(10^7)$, and the number of measurements from all the detectors and all the observations was $O(10^{13})$, so the dimensions of M, A, S, and V can have similar orders of magnitude in principle.

Because with our large data volume it is computationally expensive, if not impossible, to estimate all the elements of the covariance matrix, make sure that the matrix is invertible, and actually invert it, we would like to make a simplification by assuming that the matrix is diagonal. In other words, we would like the uncertainty on one measurement to be uncorrelated with that of every other measurement. However, as shown in figure 2.6, timestreams from different detectors are highly correlated because of the dominant, common, low-frequency atmospheric noise. This makes measurements taken on nearby pixels at nearby times by different detectors have correlated uncertainties. At a lower level, detectors also have uncorrelated $1/f$ noise, which is not caused by the atmosphere but by various components of the instrument. (I use the term $1/f$ *noise* to simply mean a noise spectrum that rises as the frequency decreases, and the spectrum may not exactly be inversely proportional to the frequency.) The $1/f$ noise in a timestream makes measurements taken at nearby times by one detector have correlated uncertainties. Regarding the atmospheric noise, in fact we do not necessarily need to treat it as a source of noise as far as the simplification that we would like to make is concerned. This is because the telescope scans fast enough (one degree per second) so that atmospheric fluctuations appear static on a timescale of one scan. Therefore, we can treat atmospheric noise as a slowly varying signal instead of a source of correlated noise among detectors, so atmospheric noise does not need to contribute to non-diagonal elements of the covariance matrix. Regarding the uncorrelated $1/f$ noise, we follow the idea proposed in Hivon et al. [2002], which was to apply a high-pass filter to timestreams to remove the noise. Doing so makes the assumption that the matrix is diagonal reasonable.

Making the simplification that the covariance matrix is diagonal, we can have an independent likelihood function and an independent maximum likelihood solution for each pixel and each frequency band. In this case, the elements of the matrices that form the solution

(the matrices in equation 3.4) have the following forms:

$$V^{-1} = \begin{pmatrix} w_\alpha & 0 & 0 & \cdots \\ 0 & w_\beta & 0 & \cdots \\ 0 & 0 & w_\gamma & \cdots \\ \vdots & \vdots & \vdots & \ddots \end{pmatrix}, \tag{3.5}$$

$$A^T V^{-1} A = \frac{1}{4} \begin{pmatrix} \sum w_i & \sum w_i \, cos\, 2\psi_i & \sum w_i \, sin\, 2\psi_i \\ \sum w_i \, cos\, 2\psi_i & \sum w_i \, cos^2 2\psi_i & \sum w_i \, cos\, 2\psi_i \, sin\, 2\psi_i \\ \sum w_i \, sin\, 2\psi_i & \sum w_i \, cos\, 2\psi_i \, sin\, 2\psi_i & \sum w_i \, sin^2 2\psi_i \end{pmatrix}, \tag{3.6}$$

$$A^T V^{-1} M = \frac{1}{2} \begin{pmatrix} \sum w_i \, I_i \\ \sum w_i \, I_i \, cos\, 2\psi_i \\ \sum w_i \, I_i \, sin\, 2\psi_i \end{pmatrix}. \tag{3.7}$$

In these expressions, i labels a detector ($i = \alpha, \beta, \gamma, \ldots$), w_i represents the inverse variance of the measurement from a detector (the weight of the measurement), and each summation runs over i.

Estimating the Stokes parameters for each pixel and for each frequency band then becomes similar to calculating weighted means of only the measurements taken on that pixel and in that frequency band. We construct the vector in equation 3.7 by adding the weighted measurements from the detectors (including the appropriate factors of *cos* and *sin*), construct the matrix in equation 3.6 by adding the weights (also including the appropriate factors of *cos* and *sin*), and multiply the inverse of the matrix (the combined weights) by the vector (the combined weighted measurements).

Here are expressions for the weighted means for two simplified situations. If multiple detectors have similar weights, and their angles are evenly spaced in the range from 0 to π, which are not far from the actual conditions of our measurements, then the off-diagonal

elements of the matrix in equation 3.6 are close to 0, so S approximately has the following form:

$$S = \begin{pmatrix} T \\ Q \\ U \end{pmatrix} \approx 2 \begin{pmatrix} \sum w_i \, I_i \, / \, \sum w_i \\ \sum w_i \, I_i \, cos \, 2\psi_i \, / \, \sum w_i \, cos^2 \, 2\psi_i \\ \sum w_i \, I_i \, sin \, 2\psi_i \, / \, \sum w_i \, sin^2 \, 2\psi_i \end{pmatrix}. \tag{3.8}$$

If there are only four detectors, α, β, γ, and δ, and the detectors have the same weight and have 0°, 45°, 90°, and 135° as their angles, then

$$S = \begin{pmatrix} T \\ Q \\ U \end{pmatrix} = \begin{pmatrix} (I_\alpha + I_\beta + I_\gamma + I_\delta)/2 \\ I_\alpha - I_\gamma \\ I_\beta - I_\delta \end{pmatrix}, \tag{3.9}$$

which reproduces the definitions of the Stokes parameters shown in figure 3.2.

3.2.3 Single-Observation and Coadded Maps

Following past power spectrum analyses from SPT, we continued using the mapmaking method discussed in subsection 3.2.2 for this analysis. To process all the timestreams in the dataset, first we made maps for individual subfield observations, and then we combined those maps in different ways for different analysis tasks. Now I discuss these two steps.

The maps from one subfield observation comprises what we call weighted T, Q, and U maps and weight maps for each of the three frequency bands. Weighted T, Q, and U maps in one frequency band are represented as an array of vectors. Each vector is for one pixel, and the vector is the one in equation 3.7 formed by all the measurements taken on that pixel during that subfield observations by detectors in that frequency band. The weight maps in that frequency band are represented as an array of matrices. Each matrix is connected to one vector in the array of the vectors and is the matrix in equation 3.6 formed by the same

set of measurements used for the vector.

We constructed the weighted T, Q, and U maps and weight maps for each subfield observation and each frequency band by applying the same processing repeatedly to each timestream from each scan of that observation. Here I discuss main steps in that processing. For each scan, we converted the unit of the timestream of each detector from W to μK, applied a high-pass filter and an anti-aliasing filter to the timestream, and assigned a weight to the filtered timestream. As discussed in subsection 3.2.2, we needed to apply a high-pass filter to use the simplified maximum likelihood method. In fact, there was another purpose of applying a high-pass filter, which was to improve high-ℓ noise in our maps. This point will be discussed in section 4.1. After we filtered each timestream, for each of its samples, we identified which pixel of the subfield that sample belonged to and added that sample's contributions to the sums in equations 3.6 and 3.7 for that pixel and the appropriate frequency band.

We combined weighted T, Q, and U maps and weight maps from multiple individual subfield observations to create what we call coadded T, Q, and U maps, T, Q, and U coadds for short, for each frequency band. The coadds in one frequency band from a group of individual subfield observations were made by adding all the weighted T, Q, and U maps from those observations together, adding all the weight maps together, and multiplying the inverse of the added weight maps by the added weighted T, Q, and U maps.

We used this coadding procedure to make different types of coadds for each frequency band. We made what we call the full-depth coadds, which were the results of combining the maps from all the 3334 subfield observations. The full-depth coadds have the lowest possible noise levels that we can achieve with our dataset. Our full-depth coadds will be shown in section 4.3. We also divided all the subfield observations into two halves and made coadds for each half. We call these coadds half-depth coadds. Furthermore, we divided all the subfield observations into 30 groups and made coadds for those groups as well. We call these coadds

bundles. A bundle comprises coadds from approximately 100 subfield observations (about 20–30 from each subfield). We used these different types of coadds for different analysis tasks.

After we made these coadds, we compared the full-depth and half-depth coadds with publicly available *Planck* maps to check how well our maps were calibrated and obtained calibration factors that we needed to multiply our coadds by from the comparison. We applied these factors to the full-depth and half-depth coadds and the bundles. This calibration process and another related topic will be discussed in section 4.2. Then, we used the bundles to estimate the $EE/TE/TT$ spectra of the anisotropies of the microwave sky, which is the topic of the next subsection.

A few notes on some terms: I used the phrase *the anisotropies of the microwave sky* in the previous sentence, and this phrase will appear again in later sections. I will also use the phrase *the anisotropies of the CMB* in some places. The former encompasses the latter because there are other astrophysical sources of microwave emission than the CMB. In some discussions, both phrases seem equally appropriate. In other discussions, one phrase seems more appropriate than the other, and I will use what I think is the better one in those cases. The $EE/TE/TT$ spectra of the latter are the same in different frequency bands when they are all expressed in the unit of the equivalent CMB temperature fluctuation rather than a unit of intensity. A temperature fluctuation at one location in the sky at one frequency represents a fluctuation in the intensity of the radiation from that location. The temperature and intensity are connected via a derivative of the blackbody spectrum as follows:

$$\Delta T(\nu) = \Delta I(\nu) \,/\, \frac{\partial B(\nu, T)}{\partial T}|_{T=2.73\ K} \tag{3.10}$$

As for the CMB, $\Delta I(\nu)$ at different frequencies are equivalent to the same $\Delta T(\nu)$. That is not quite true for the spectra of emission from other sources such as galaxies because the spectra have different frequency dependence. When I mention the spectra from the other sources, what I have in mind are the spectra in all the three frequency bands that we observe, but I

will omit the words *frequency bands* for brevity.

3.3 From Maps to Spectra

In this section, first I discuss general mathematical relations between a set of T, Q, and U maps and its $EE/TE/TT$ spectra, and then I discuss the specific procedure that we used to obtain unbiased estimates of the $EE/TE/TT$ spectra of the anisotropies of the microwave sky from the coadds made in the previous step.

3.3.1 From T, Q, and U to EE/TE/TT

Given a set of T, Q, and U maps, we can calculate its TT spectrum from the T map alone through equations 1.1 and 1.2, and we can calculate its EE/TE spectra by constructing an E-mode polarization map, or an E map for short, from the Q and U maps and using equations similar to 1.1 and 1.2 on the E and T maps. The qualitative definition of the E-mode polarization shown in figure 1.6 suggests that the value at a given location in the E map is determined by the radial and tangential components of the polarization at surrounding locations. These components can be calculated by combining the values in the Q and U maps at those locations. Figure 3.3 shows that Q and U can be combined to form a new Stokes parameters Q_r, which quantifies the radial and tangential components of the polarization at each surrounding location, $\hat{\boldsymbol{n}}'$, with respect to the originally given location, $\hat{\boldsymbol{n}}$. Then, Q_r is integrated over $\hat{\boldsymbol{n}}'$ to give the value in the E map at $\hat{\boldsymbol{n}}$ as follows:

$$E(\hat{\boldsymbol{n}}) = \int Q_r(\hat{\boldsymbol{n}}')\, w(\hat{\boldsymbol{n}} \cdot \hat{\boldsymbol{n}}')\, d\hat{\boldsymbol{n}}', \tag{3.11}$$

where $w(\hat{\boldsymbol{n}} \cdot \hat{\boldsymbol{n}}')$ is a weight function equal to the inverse of the square of the distance between the two locations (Zaldarriaga [2001]). When $\hat{\boldsymbol{n}}' = \hat{\boldsymbol{n}}$, the weight is chosen to be zero. Incidentally, a B-mode polarization map can be obtained by a similar integral, in

which U_r is integrated instead of Q_r. (Because Q and U maps measured by an experiment are images that have a set of pixels, a discrete version of the integral is needed in practice.) The particular choice of the weight above is applicable to only a small patch of the sky where the curvature of the sphere can be ignored, and the weight in a general case has a more complex form (Rotti and Huffenberger [2019]). However, the idea of integrating radial and tangential polarization remains the same. Once the E map is constructed, we can calculate its spherical harmonic coefficients, $E_{\ell m}$, and then combine $E_{\ell m}$ and $T_{\ell m}$ to obtain the EE/TE spectra by using the following equations:

$$E_{\ell m} = \int E(\hat{\boldsymbol{n}})\, Y^*_{\ell m}(\hat{\boldsymbol{n}})\, d\hat{\boldsymbol{n}} \tag{3.12}$$

$$C_\ell^{EE} = \frac{1}{2\ell+1} \sum_m E^*_{\ell m}\, E_{\ell m} \tag{3.13}$$

$$C_\ell^{TE} = \frac{1}{2\ell+1} \sum_m \Re(T^*_{\ell m}\, E_{\ell m}) \tag{3.14}$$

(Because the E map is an image that has a set of pixels, the integral in equation 3.12 is replaced by a discrete spherical harmonic transform in practice.)

In fact, we do not need to explicitly construct an E map to obtain $E_{\ell m}$ because $E_{\ell m}$ can be directly calculated from spherical harmonic transforms of Q and U maps. These transforms use spin-±2 spherical harmonics, ${}_{\pm2}Y_{\ell m}(\hat{\boldsymbol{n}})$, and $E_{\ell m}$ can be obtained by the following equation:

$$(E_{\ell m} \mp iB_{\ell m}) = \int (Q \pm iU)(\hat{\boldsymbol{n}})\ {}_{\mp2}Y^*_{\ell m}(\hat{\boldsymbol{n}})\, d\hat{\boldsymbol{n}}. \tag{3.15}$$

($B_{\ell m}$ represents the spherical harmonic coefficients of the B-mode polarization map.) Spin-±2 spherical harmonics are obtained by applying certain differential operators involving $\frac{\partial}{\partial\theta}$ and $\frac{\partial}{\partial\phi}$ to the usual spherical harmonics, $Y_{\ell m}(\hat{\boldsymbol{n}})$, and are used for multipole expansions of spin-±2 functions on the sphere (Zaldarriaga and Seljak [1997]). A spin-s function, ${}_sf(\hat{\boldsymbol{n}})$, is

a function whose value at $\hat{\boldsymbol{n}}$ needs to be defined with respect to the directions of $\hat{\boldsymbol{\theta}}$ and $\hat{\boldsymbol{\phi}}$ at that location and transforms in a particular way when $\hat{\boldsymbol{\theta}}$ and $\hat{\boldsymbol{\phi}}$ are rotated around $\hat{\boldsymbol{n}}$. Under a right-handed rotation by an angle, ψ, the value acquires a multiplicative factor, $e^{-is\psi}$. (${}_sf(\hat{\boldsymbol{n}}) \rightarrow e^{-is\psi}\,{}_sf(\hat{\boldsymbol{n}})$.) The transformation equations from Q and U to Q_r and U_r shown in figure 3.3 indicate that $(Q \pm iU)(\hat{\boldsymbol{n}})$ are spin-s functions where $s = \mp 2$. The usual spherical harmonics are spin-0 functions. For this analysis, we used publicly available programs called `HEALPix` (Gorski et al. [1999]) and `PolSpice` (Chon et al. [2004]) to calculate discrete versions of these transforms on our coadds.

A big difference between the 2018 $EE/TE/TT$ analysis and this one is that we are no longer using a flat-sky approximation, in which a small area of the sphere is projected onto a plane, and two-dimensional Fourier transforms of images on the plane are used to estimate angular power spectra instead of spherical harmonic transforms of the small area of the sphere. We decided to make this change because we learned from the 2018 analysis that the winter field occupied large enough of an area of the sphere to cause undesirable projection effects, especially effects related to how values of a spectrum at different ℓs are correlated, when the flat-sky approximation was used.

(2) $$Q_r(p_n') = Q(p_n')\cos 2\psi_n - U(p_n')\sin 2\psi_n$$
$$U_r(p_n') = Q(p_n')\sin 2\psi_n + U(p_n')\cos 2\psi_n$$

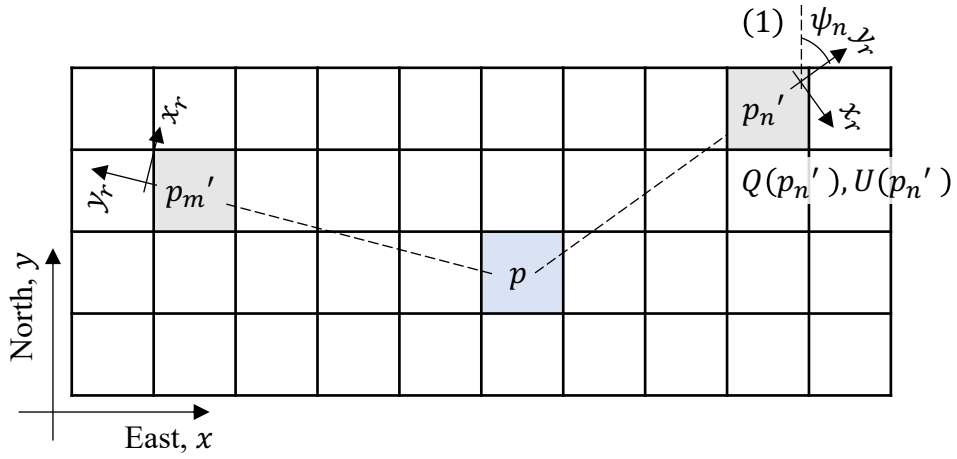

(3) $$E(p) = \sum_i Q_r(p_i')\, w_i, \qquad B(p) = \sum_i U(p_i')\, w_i$$

Figure 3.3. Transformation from Q and U to E and B. This diagram shows how the E-mode polarization in a given pixel can be calculated from the Q and U values in surrounding pixels. The grid represents a group of pixels, and the Q and U values in each pixel have been measured. The E-mode polarization in pixel p is a sum of contributions from all surrounding pixels. For example, to obtain the contribution from pixel p_n', the first step is to find the angle between the y-axis and the line joining the centers of p and p_n' and define a new set of axes x_r and y_r, where y_r is in the radial direction. The second step is to calculate the new Q and U values in p_n' that are defined with respect to the new axes. The relation between the new values, $Q_r(p_n')$ and $U_r(p_n')$, and the original values, $Q(p_n')$ and $U(p_n')$, is shown in the two equations. This process is repeated for every surrounding pixel, and the E value in p is a weighted sum of all the Q_r values.

3.3.2 Pixel Mask

I have discussed the mathematical relations between a set of T, Q, and U maps and its $EE/TE/TT$ spectra, and now I discuss the procedure we used to obtain unbiased estimates of the $EE/TE/TT$ spectra of the anisotropies of the microwave sky from our coadds. In particular, I discuss five elements of the procedure: designing a pixel mask, calculating cross-correlation spectra between bundles, correcting for known biases in the cross-correlation spectra, probing the spectra for potential systematic errors, and estimating the statistical errors in the spectra. This procedure was mostly the same as what was used in past analyses.

Before calculating the spherical harmonic transforms of our coadds, we multiplied them by a pixel mask to downweight certain pixels so that we could measure the $EE/TE/TT$ spectra of the anisotropies of the CMB with higher precision. A pixel mask is a map that has the value 1.0 for most of its pixels but has values smaller than 1.0 and larger than or equal to 0.0 for some of its pixels.

Our pixel mask had two components. One component was what we call a border mask, which defined the extent of the winter field that we wanted to use. We did not want to include every single pixel within the field because some pixels near the borders were very noisy. Those pixels were observed by only a small number of detectors. However, we also did not want to discard an unnecessarily large number of pixels because discarding pixels meant decreasing the sky area and thus increasing the sample variance discussed in section 2.4. To find the optimal extent of the field, we tried different extents and used the option that had the best balance between decreasing noise and increasing the sample variance. In this option, we kept 96% of all the pixels that we ever observed.

Another component of our pixel mask was what we call a source mask. It had 2654 small holes that covered pixels containing galaxies and galaxy clusters that we detected in our maps with high signal-to-noise ratios. Finding galaxies and galaxy clusters was in itself a large-scale analysis project. This was done by other teams within our collaboration, and we

used a catalog produced by them, The total area that we lost to these holes was 1.4% of the area of the border mask.

As is the case with multiplying a signal by a tapering function before calculating its discrete Fourier transform to reduce spectral leakages, our border and source masks had tapers near the borders and the edges of the holes.

3.3.3 Cross-Correlation Spectra

To estimate the $EE/TE/TT$ spectra of the anisotropies of the microwave sky, we used not the full-depth coadds but the bundles (partial-depth coadds) to avoid a potential additive bias caused by noise in the full-depth coadds. For example, the spherical harmonic coefficients of the full-depth T coadd in one frequency band, $T_{\ell m,\,full}$, have two components: a component associated with the signals, $s_{\ell m}$, and one associated with noise, $n_{\ell m}$. Then, the TT spectrum of the coadd can be expressed in the following way:

$$\begin{aligned} C^{TT}_{\ell,\,full} &= \frac{1}{2\ell+1}\sum T^{*}_{\ell m,\,full}\,T_{\ell m,\,full} \\ &= \frac{1}{2\ell+1}\sum \left(s_{\ell m}+n_{\ell m}\right)^{*}\left(s_{\ell m}+n_{\ell m}\right) \\ &= \frac{1}{2\ell+1}\sum (s^{*}_{\ell m}\,s_{\ell m}+s^{*}_{\ell m}\,n_{\ell m}+n^{*}_{\ell m}\,s_{\ell m}+n^{*}_{\ell m}\,n_{\ell m}). \end{aligned} \tag{3.16}$$

On the last line, the first term inside the parentheses is an estimate of the signal spectrum and is the only term that we would like to have ideally. The second and third terms do not create biases because the signals and noise do not correlate with each other. However, the fourth term, which is the spectrum of the noise, does create a bias in $C^{TT}_{\ell,\,full}$ as an estimate of the signal spectrum unless the noise spectrum is accurately estimated and subtracted from $C^{TT}_{\ell,\,full}$. This means that a misestimation and then an improper subtraction of the noise spectrum create an additive bias.

To avoid this potential issue, we calculated cross-correlation spectra between the bundles.

Different bundles contain observations conducted during different periods, so noise in one bundle does not correlate with that in another bundle (Polenta et al. [2005]). For example, two T coadds from two bundles, i and j, in the same frequency band, contain the same signals, $s_{\ell m}$, but different noise, $n_{\ell m,\,i}$ and $n_{\ell m,\,j}$. Then, the TT cross-correlation spectrum between the two bundle coadds (as opposed to the TT autocorrelation spectrum of the full-depth coadd in the previous case) can be expressed in the following way:

$$\begin{aligned} C^{TT}_{\ell,\,i\times j} &= \frac{1}{2\ell+1}\sum \Re[(s_{\ell m}+n_{\ell m,\,i})^{*}\,(s_{\ell m}+n_{\ell m,\,j})] \\ &= \frac{1}{2\ell+1}\sum \Re[(s^{*}_{\ell m}\,s_{\ell m}+s^{*}_{\ell m}\,n_{\ell m,\,j}+n^{*}_{\ell m,\,i}\,s_{\ell m}+n^{*}_{\ell m,\,i}\,n_{\ell m,\,j})]. \end{aligned} \tag{3.17}$$

In this case, the fourth term does not create a bias in $C^{TT}_{\ell,\,i\times j}$ as an estimate of the signal spectrum because the correlation represented by that term is also expected to be zero. When there are n bundles, $n(n-1)/2$ cross-correlation spectra can be calculated, and the average of the spectra can be used as the final estimate of the TT signal spectrum. Although this second method is not subject to the bias that can affect the first method, estimates of signal spectra obtained from the second method do have larger variances than those obtained from the first method. However, the differences become negligible if there are several tens of bundles.

With our 30 bundles, we calculated 435 cross-correlation spectra and their average for $EE/TE/TT$ and for combinations of different frequency bands. Equation 3.18 represents all the average cross-correlation spectra that we obtained:

$$C^{AB,\,\nu_1\times\nu_2}_{\ell,\,avg} = \frac{2}{n(n-1)}\sum_{i=1}^{n-1}\sum_{j=i+1}^{n}\frac{1}{2\ell+1}\sum_{m=-\ell}^{\ell}\Re(A^{*}_{\ell m,\,i,\,\nu_1}\,B_{\ell m,\,j,\,\nu_2}), \tag{3.18}$$

where A and B represent combinations of T and E, and ν_1 and ν_2 represent combinations of two of the three frequency bands, and i and j represent bundle numbers.

3.3.4 Known Biases

Although the average cross-correlation spectra that we calculated from the bundles did not have the additive noise bias discussed above, they did still contain some multiplicative biases that we needed to correct for. These multiplicative biases were associated with certain features present in the maps.

One bias was caused by the high-pass filter that we applied to the timestreams during the mapmaking. This introduced a multiplicative bias in the average cross-correlation spectra because the filter removed not only low-frequency noise in the timestreams but also low-frequency signals. We calculated this loss of signals through simulations, which we call mock observations.

In general, in a mock observation, we prepare a set of simulated T, Q, and U maps in one frequency band, extract the telescope pointing information from a real subfield observation, generate a mock timestream for each detector and each scan by using the pixel values of the simulated maps and the pointing information, filter the mock timestreams in the same way as we filtered the real timestreams during the mapmaking, and make output T, Q, and U maps from the mock timestreams. By dividing the $EE/TE/TT$ spectra of the output maps with those of the simulated maps, we can quantify the loss of signals caused by the filter. We call these ratios filter transfer functions. To correct for the signal loss in $EE/TE/TT$ spectra calculated from real maps, we divide the spectra by the filter transfer functions. Filtering timestreams biases signal spectra calculated from the maps, but the biases can be removed from the spectra through simulations. When this approach was proposed by Hivon et al. [2002], it was regarded as an innovative idea in the CMB community, and SPT has always used this approach.

For this analysis, we created 500 sets of simulated noiseless T, Q, and U maps for each frequency band, mock-observed each set of simulated maps using approximately 40 observations' pointing information for each subfield, made a corresponding set of T, Q, and U

coadds from the output maps of the mock subfield observations, and averaged the ratios of the output spectra to the input ones over all the realizations to estimate the filter transfer functions associated with our high-pass filter and correct the average cross-correlation spectra.

Another bias was associated with the telescope's finite resolution caused by diffraction and other optical effects. The sky viewed through the telescope in one frequency band is a smoothed version of the true sky in that frequency band. This smoothed sky can be mathematically represented as the convolution of the true sky and the point spread function of the telescope. We commonly call a point spread function a beam. Our beams are approximately Gaussian. In harmonic space, an angular power spectrum of the sky viewed through the telescope is the product of the true spectrum and the angular power spectrum of the beams of our telescope. We estimated our beam in each frequency band by observing point-like objects in the sky such as planets and galaxies, making maps of those objects, and calculating two-dimensional Fourier transforms of the maps. (Because these maps covered very small areas of the sky, where the curvature of sky can be ignored, two-dimensional Fourier transforms are accurate approximations of spherical harmonic transforms.) Then, we divided the average cross-correlation spectra by the power spectra of the beams to correct for the smoothing effect. Accurately estimating our beams is an analysis task extremely important to not only this analysis but every other SPT analyses. However, because I was not closely involved in that analysis task, I will not discuss the beams further in this thesis except for simply showing what they look like in section 4.5.

One other bias was also a smoothing effect, which was caused by the pixelated nature of our maps. After many scans from many observations, our detectors observed many slightly different parts of each pixel, and the value of a pixel in a coadd is a weighted average of all those measurements. This averaging is a smoothing effect. The sky represented by our coadds is the convolution of the true sky and a kernel that has the shape of a pixel. Our pixels are

not exactly rectangular but close, so the kernel is approximately a two-dimensional rectangle function. In harmonic space, the smoothing effect multiplies an angular power spectrum of the true sky by the angular power spectrum of the kernel. We calculated the power spectra of our pixels (different pixels in our field have slightly different shapes) and used the average spectrum to correct for this bias.

All the biases discussed in this section will be shown in section 4.5.

3.3.5 Unknown Systematic Errors

Besides correcting for the known biases in the average cross-correlation spectra, we also probed and are still probing the spectra for potential systematic errors,

One probe is a series of what we call null tests. In general, in a null test, we split a full dataset into two parts in a way that makes one part more sensitive to a potential systematic error than the other part. For example, for a field that we observed during both dark months of a year and bright months, we may want to confirm that the telescope did not receive a significant amount of radiation during observations conducted during the bright months. (The sun is typically at least a few tens of degrees far from any border of a field that we observe during bright months of a year, but we still want to check whether the sun has a nonnegligible effect.) In that case, we can use all the observations conducted when the sun was above the horizon to form one part and all the observations conducted when the sun was below the horizon to form the other part. For each frequency band, within each part, we construct the same number of bundles. Then, we subtract the bundles within one part from the bundles within the other part to form what we call null bundles. Ideally, the two parts contain the same signals, and neither part contains the potential systematic error, so the null bundles contain only noise. From the null bundles we calculate what we call null spectra, which are similar to the average cross-correlation spectra discussed in subsection 3.3.3, and the only difference is that the null bundles are used in this case instead of bundles

that contain signals. We check whether the null spectra are consistent with noise or contain something significant beyond noise. If the latter is the case, that means we find a significant level of a systematic error, and we need to add extra steps to our data processing to remove that systematic error. For this analysis, we conducted null tests associated with six types potential systematic errors. We did discover a systematic error through one of the tests and incorporated a mitigation method into the way we calculated the cross-correlation spectra from the signal bundles. These tests and their results will be discussed in section 4.4.

Other than the null tests for each frequency band, another probe is a series of consistency tests between the average cross-correlation spectra in different frequency bands. Because the $EE/TE/TT$ spectra of the anisotropies of the CMB in all frequency bands are identical, and the spectra of the anisotropies of other sources have reasonably well-known frequency dependence, we can use our average cross-correlation spectra in one frequency band to predict what we should obtain in another frequency band. If the prediction and what we actually obtained agree within noise, we regard the spectra in the two frequency bands as consistent measurements of the same physical phenomena. If there is a disagreement, it is possible that the spectra in one frequency band contain a systematic error. For example, the cause of the systematic error may be that we did not estimate the beam in one frequency band correctly and therefore did not properly correct for the multiplicative bias in that frequency band. As of the writing of this thesis, we have just started these tests and do not have results to report yet.

3.3.6 Band Powers and Covariance

Once we corrected for the known biases in $C_{\ell,\,avg}^{AB,\,\nu_1\times\nu_2}$ and removed a systematic error that we found through null tests, we reduced the spectra to what we call band powers.

Although each spectrum had a value at every ℓ (within a range of ℓs that we measured with our data), values at nearby ℓs were not independent measurements in that they had

highly correlated uncertainties. One reason for this correlation is that the maps from which the spectrum was obtained cover only a limited area of the sky. This is similar to the situation where the Fourier transform of a signal is calculated after that signal is multiplied by a rectangular window function. In that case, the width of the rectangle determines the frequency resolution of the spectrum of the signal.

Instead of keeping the values of a spectrum at every ℓ, we created intervals of ℓs, or what we call ℓ bins, and averaged the values within each ℓ bin. This way, average values in nearby bins were less correlated. We call these average values in different ℓ bins band powers and will use the band powers to constrain cosmological parameters. For this analysis, the range of ℓs we probe is $[400, 4000]$, and the size of an ℓ bin is 50. Binning a spectrum is in fact not a process that we use at only this stage. We bin spectra in other steps as well to better interpret some results because a binned spectrum has less scatter in its data points.

For a binned spectrum, equation 2.1 is slightly modified. The factor in the front becomes $(2\ell + 1)\,\Delta\ell\, f_{sky}$, where $\Delta\ell$ is the width of a bin. In other words, binning a spectrum reduces the number of data points but also reduces the uncertainty in each data point.

Before we can fit theoretical models to the band powers and constrain cosmological parameters, we needed to estimate the statistical errors in our band powers. We needed to construct a band power covariance matrix, which contains our estimates of the variance of each band power and the covariance between different band powers.

The band powers represent our estimates of the underlying $EE/TE/TT$ spectra from which the anisotropies of the microwave sky that we observe were generated a random realization, and multiple factors contribute to the variance and covariance. One factor is the sample variance associated with signals that was discussed in section 2.4. Another factor is noise in our data, which is caused by the atmosphere and our instrument. As suggested in figure 2.7, the first factor is more important than the second one at relatively low ℓs, and this relation reverses at higher ℓs. A third factor is the correlation between measurements at

nearby ℓs caused by the small sky area that we observed.

In past SPT analyses, empirical approaches involving mock-observation output data and bundles constructed from real data were used to build covariance matrices. To estimate the sample variance associated with signals, we mock-observed a few hundred sets of simulated noiseless T, Q, and U maps in each frequency band, calculated band powers from each set of output T, Q, and U coadds, created an array of a few hundred values for each ℓ bin and each type of band power (a type is specified by choices of A, B, ν_1, and ν_2 in equation 3.18), and calculated the covariance matrix of these arrays by following the standard definition of covariance. To estimate the noise variance, we used all the $n(n-1)/2$ cross-correlation spectra that we obtained by cross-correlating the bundles. We created an array of $n(n-1)/2$ values for each ℓ bin and each type of band power and calculated the covariance matrix of these arrays. A common issue in these approaches has been that some matrix elements were not estimated accurately because the numbers of simulated skies and bundles were finite, and this caused difficulties in inverting those matrices. To address that issue, we had to put into a significant amount of work to condition those matrices (Balkenhol and Reichardt [2022]).

For this analysis, besides these empirical approaches, we also adopted a recently developed approach that uses analytical calculations (Camphuis et al. [2022]). After checking that the empirical and analytical approached produced consistent results, we used the band power covariance matrix produced by the analytical approach because the analytically calculated matrix did not need conditioning. The analytical approximations did require our pixel mask to have no holes because a mask that had many holes caused band powers in different ℓ bins to correlate with each other in ways that were too difficult to calculate analytically. As a result, we also adopted a procedure known as inpainting, in which we guessed what the CMB anisotropies should look like in pixels contaminated by bright galaxies and galaxy clusters by using values of surrounding pixels and use the guessed values in the contaminated pixels. Like obtaining accurate beams, obtaining an accurate and well-behaved covariance matrix

is another extremely important analysis task that required significant work. However, given that I was not closely involved in this task, I will not discuss it further in this thesis.

Having band powers and a band power covariance matrix enables us to constrain cosmological parameters, which is the topic of the next section.

3.4 From Spectra to Parameters

In this subsection, first I discuss the Bayesian inference framework that we plan to use to constrain cosmological parameters from the band powers obtained in the previous step, and then I discuss the tests that we plan to run to probe the constraints for potential issues.

3.4.1 Bayesian Inference Framework

According to Bayes' theorem,

$$p(\theta|x) \propto L(x|\theta)\,\pi(\theta), \tag{3.19}$$

where $\pi(\theta)$ is a prior probability density function for a set of parameters, θ, that an experimenter wishes to constrain, $L(x|\theta)$ is a likelihood function for an experiment's data, x, given θ, and $p(\theta|x)$ is a posterior probability density function for θ given x. The posterior probability density function represents constraints on the parameters given the data.

In our context, x is a set of band powers, and θ comprises cosmological parameters of ΛCDM and its extensions and a set of parameters not relevant to cosmological models. The non-cosmology parameters contain parameters that specify the amplitudes and shapes of the $EE/TE/TT$ spectra of the anisotropies of other sources than the CMB and parameters that scale the band powers by constant factors to reflect our estimates of the statistical errors in the overall amplitudes of the band powers. The number of these non-cosmology parameters is around 30, and the number of the cosmological parameters is between 5 and 10.

The quantities $\pi(\theta)$ and $L(x|\theta)$ are then based on the band powers and parameters. Regarding $\pi(\theta)$, we use Gaussian priors for the non-cosmology parameters and a few cosmological parameters such as τ that we are not able to constrain well because we observe only a small fraction of the sky. The mean and standard deviation of each Gaussian prior are based on measurements of the corresponding parameter in the literature (except for the parameters relevant to the band power amplitudes). For other cosmological parameters, we use uniform priors within physically allowed ranges. Regarding $L(x|\theta)$, it has the following form:

$$L(x|\theta) \propto exp\{-[x - m(\theta)]^T V^{-1} [x - m(\theta)]\}, \tag{3.20}$$

where V is a band power covariance matrix, and $m(\theta)$ is a set of theoretical band powers predicted by θ. (In fact, x is also affected by θ through the scaling factors relevant to the band power amplitudes.)

To obtain $p(\theta|x)$, we repeatedly draw particular values of the parameters from $\pi(\theta)$, calculate $m(\theta)$ for those values by a multi-step process, and calculate $L(x|\theta)$ by using equation 3.20. The multi-step process to calculate $m(\theta)$ comprises using publicly available programs such as `CAMB` (Lewis et al. [2000]) to theoretically calculate the $EE/TE/TT$ spectra of the anisotropies of the CMB for the chosen cosmological parameters, combining these spectra with the $EE/TE/TT$ spectra of the anisotropies of other sources specified by the chosen non-cosmology parameters, incorporating a few effects such as the relativistic aberration of the CMB caused by the motion of the earth relative to the rest frame of the CMB, and finally reducing the combined spectra to band powers. The repeated drawing of samples from the high-dimensional parameter space is based on Markov Chain Monte Carlo techniques through publicly available programs such as `Cobaya` (Torrado and Lewis [2021]). In recent years, we have incorporated machine learning and other new computational techniques through programs such as `CosmoPower` (Spurio Mancini et al. [2022]) to make the sampling process

more efficient.

3.4.2 Consistency Tests

I have discussed the Bayesian inference framework that we plan to use to constrain cosmological parameters from the band powers obtained in the second major analysis step, and now I discuss the tests that we plan to run to probe the constraints for potential issues.

We will eventually use the full set of band powers to obtain the tightest possible constraints, but we need to test whether constraints obtained from different subsets of the band powers are consistent with each other. These subsets can be based on frequency bands (95/150/220 GHz), ℓ ranges ($\ell < 1500/\ell > 1500$, for example), and anisotropy combinations ($EE/TE/TT$). If we do not find statistically significant discrepancies, we can proceed to another test.

The next test is to check whether the constraints from the full set of band powers are robust against reasonable changes in the non-cosmology parameters. These changes can be using different priors for those parameters, removing existing parameters, or introducing new parameters. If we do not find statistically significant discrepancies again, we can be confident that the constraints obtained from the full set of band powers are valid.

When we run these tests, we will blind ourselves to some extent by shifting constraints obtained from different test configurations by an arbitrary constant for each parameter and by not revealing these shifts to ourselves. This way, we can focus on only the relative difference between two estimates of a parameter and the size of the difference compared with the two uncertainties without having to contemplating the absolute value of each estimate. After we complete these tests, we can unblind ourselves and compare our new constraints on cosmological parameters with existing ones in the literature.

One other test, which is relevant to both this and the previous major analysis steps, is what we call an alternate cosmology test. In some steps of this analysis, we used simulated sky

maps, which we generated by using the cosmological model that fitted *Planck*'s band powers the best. For example, to obtain the filter transfer functions, we mock-observed an ensemble of simulated sky maps, and they were based on *Planck*'s best-fit cosmological model. The purpose of an alternate cosmology test is to check the dependence of our simulation-based analysis results on the cosmological model used to generate the simulations. In this test, we shift *Planck*'s best-fit values of the ΛCDM parameters by five sigma in one direction in the high-dimensional parameter space, generate simulated sky maps from that alternate cosmological model, mock-observe the maps and calculate band powers, correct the band powers by using the filter transfer functions that we obtained earlier from the best-fit cosmological model (not the alternate model), use (1) the covariance matrix that we constructed earlier, which was also based on the best-fit model, and (2) the unbiased band powers to constrain the cosmological parameters, and check whether we can recover the alternate parameter values that we chose in the beginning.

As of the writing of this thesis, we have started an alternate cosmology test. We have not started the other tests discussed in this section because we need to finish the interfrequency consistency tests discussed in subsection 3.4.2 first.

CHAPTER 4

RESULTS

In the previous chapter, I discussed the methods used in each of the three major steps of this analysis. In this chapter, I will show important results from the first two major steps: full-depth coadds and unbiased band powers (unbiased to our current best knowledge). I will also discuss some of the analysis tasks from the first two major steps that I worked on with much help from my collaborators. The discussions of those analysis tasks will include details of some of the methods that were discussed briefly in the previous chapter and results that we obtained from those methods. I will start by returning to the first major step, making the individual observations' maps and coadds from the timestreams.

4.1 Timestream High-Pass Filter

As discussed in subsection 3.2.2, we applied a high-pass filter to the timestreams so that we could use the simplified maximum likelihood method of mapmaking, but there was another purpose of removing low-frequency noise from the timestreams, which was to reduce high-ℓ noise in the maps.

4.1.1 Low-Frequency and High-ℓ Noise

Low-frequency noise in timestreams can contribute to both low-ℓ and high-ℓ noise in maps. In the spherical coordinate system that we established to calculate spherical harmonic transforms of maps, the polar angle, θ, coincides with declination, and the azimuthal angle, ϕ, coincides with right ascension. (Technically, $\theta = 90^\circ - \delta$, where δ is declination.) Because a scan and therefore a timestream traces a constant-θ arc on the sphere, a low-frequency oscillation in a timestream is projected onto the sphere (onto a map) as a long-wavelength oscillation along the ϕ direction, or a low-$|m|$ oscillation, where m is from $e^{im\phi}$. Given that

$Y_{\ell m}(\theta, \phi) \propto P_\ell^m(cos\,\theta)\, e^{im\phi}$, where $|m|$ ranges from 0 to ℓ for a given ℓ, both low-ℓ and high-ℓ spherical harmonics contain low-$|m|$ oscillations. Thus, low-frequency noise in timestreams appear as low-$|m|$ noise in maps, and low-$|m|$ noise can contribute to both low-ℓ and high-ℓ noise.

Because in this analysis we aim to measure high-ℓ anisotropies of the CMB as precisely as possible, we wanted to prevent low-frequency noise in the timestreams from creating excess high-ℓ noise in the maps, and applying a high-pass filter to the timestreams was useful for this purpose. When we apply a high-pass filter to a timestream, we use a linear least-squares method to remove sines and cosines up to a certain frequency. One question we needed to answer was what value we should use for the cutoff frequency of the high-pass filter. Using a higher cutoff frequency removes more contributions of low-$|m|$ noise to high-ℓ noise, but this applies to signals as well. We did not want to make the cutoff frequency unnecessarily high and lose too many signals, so there was an optimization to be done.

4.1.2 Choice of the Cutoff Frequency

To decide what cutoff frequency we should use for the high-pass filter, we chose four candidate cutoff frequencies and a small but representative subset of the full dataset, made four versions of coadds from the same small dataset, calculated noise spectra for each version, and compared the spectra. The small dataset contained timestreams from 25 days' worth of subfield observations. The four cutoff frequencies were in fact four ranges of cutoff frequencies, but each range of frequencies was equivalent to a single cutoff value in ℓ. Because the scan speed of the telescope in right ascension is the same (one degree per second) regardless of what declination a scan is at, when an oscillation at a fixed frequency in a timestream is projected onto the sphere, the wavelength of the oscillation on the sphere subtends an angle that changes as the declination of the scan changes. The relation between the frequency, f_c, and the equivalent ℓ of the subtended angle, ℓ_c, is the following: $\ell_c = 360 \times f_c/(v\, cos\, \delta)$, where

v is one degree per second, and f_c is in Hz. To achieve the same angular-scale cutoff across the full range of declination of the field, we apply different cutoff frequencies to timestreams from scans at different declination. For example, the cutoff in ℓ at 300 is equivalent to the frequency range from 0.25 Hz (if a scan's declination is $-70°$) to 0.58 Hz (declination $-42°$). The four cutoffs in ℓ that we chose were 100, 200, 300, and 400. For each cutoff, we made the full-depth coadds from the small dataset and visually inspected some of them. To estimate the $EE/TE/TT$ spectra of noise in the full-depth coadds, we used two sets of half-depth coadds. We subtracted one set from the other to cancel the same signals in them and calculated the spectra of the difference coadds. Incidentally, the uncorrelated $1/f$ noise discussed in subsection 3.2.2 have knees at around or below 0.05 Hz (Bender et al. [2020]), so the lower bound of the frequency range equivalent to the cutoff in ℓ at 100 is still high enough to remove the $1/f$ noise and make the simplified maximum likelihood method of mapmaking valid.

Figure 4.1 shows the noise spectra of the difference coadds. Each TT noise spectrum has a "$1/\ell$" part and a flat part. While the former originates from the atmosphere, the latter originates from the instrument. Each EE noise spectrum is mostly flat because the atmosphere is mostly unpolarized. Figure 4.2 shows the same spectra but has the multiplicative factor $\ell(\ell+1)/(2\pi)$. The spectra in the second figure were also divided by 18, which is the ratio of the number of subfield observations in the full dataset to the number in the small subset. With the division, these spectra should roughly represent what we would have obtained if we had used the full dataset for this investigations and make it easier to see at roughly what ℓs the noise spectra intersect with expected signal spectra.

Given these noise spectra, we decided to use 300 as the cutoff for this analysis. Decreasing the cutoff from 300 to 200 or 100 introduced the bumps in some of the noise spectra at ℓs near 1500, 2000, and 2500, and increasing the cutoff from 300 to 400 did not make a big difference because the bumps were mostly removed when 300 was used. Similar bumps have been seen

in past SPT analyses, but the locations and shapes of these bumps have varied. These bumps are thought to be caused by some properties of the way in which the atmosphere is observed through our scan pattern. Regardless of the exact mechanism causing these bumps, they are indeed the excess high-ℓ noise that we wanted to reduce. My previous statements about how low-frequency noise in a timestream is projected onto the sphere might have implied that I was discussing excess high-ℓ noise that originates from the instrument, but the origin is the atmosphere, which we observe with our detector array through the raster scan, and the resultant timestreams are then projected back onto the sphere.

In hindsight, besides comparing the noise spectra, it might have been better to also consider the sample variance. Although decreasing the cutoff from 300 to 200 or 100 introduced the excess noise, the uncertainties in some of our band powers near the affected ℓs are dominated by the sample variance. If we had used a lower cutoff, we could have retained more signals and reduced the sample variance. This trade-off was not explored in my investigation and may be useful to consider in future analyses.

In the 2018 analysis, besides a high-pass filter, we also applied what we call a common-mode filter. We calculated the average timestream of the timestreams from all the good detectors on each wafer and in each frequency band and subtracted the average from each individual timestream. The common-mode filter acted as another kind of high-pass filter, and the cutoff was approximately 500. The common-mode filter was necessary for the 2018 analysis because 2018 timestreams had worse low-frequency noise than 2019–2020 ones, which we believe was caused by vibrations of a mechanical structure on which the wafers were mounted. After the 2018 season, we installed a new mechanical structure that was much more stable. Analyzing 2019–2020 timestreams, we decided that we no longer needed a common-mode filter.

Other than the cutoff value of the high-pass filter, we optimized several other mapmaking parameters by analyzing small portions of the full dataset. After that, we made the weighted

T, Q, and U maps and weight maps for all the 3334 subfield observations, from which we then made various coadds: the full-depth coadds, two sets of half-depth coadds, and 30 bundles.

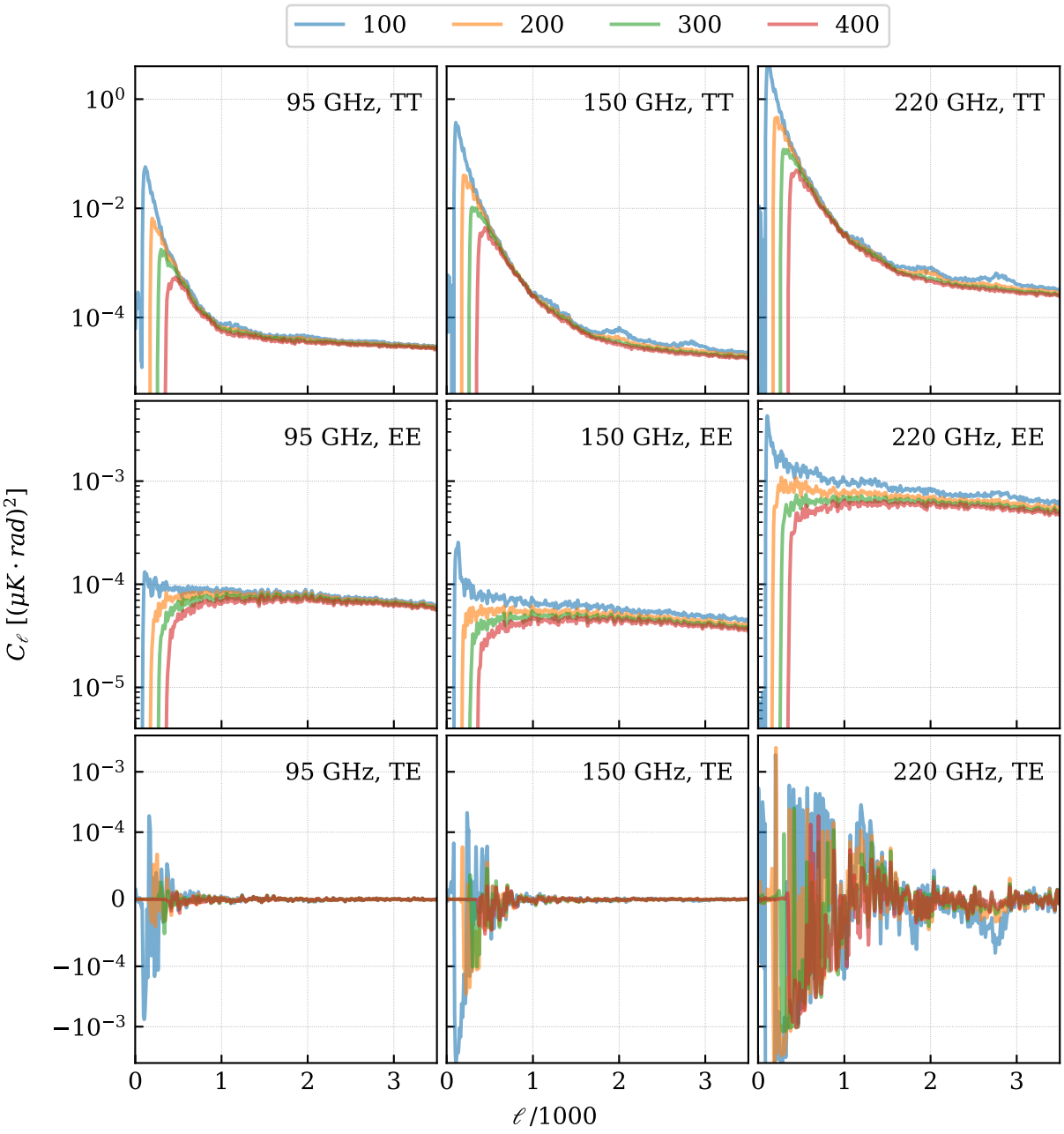

Figure 4.1. $EE/TE/TT$ noise spectra (C_ℓ) obtained from different high-pass filters. Each of the nine panels shows four spectra associated with the four different high-pass cutoff values (four colored curves) for one frequency band and one combination of two anisotropy types (label in the top right corner)

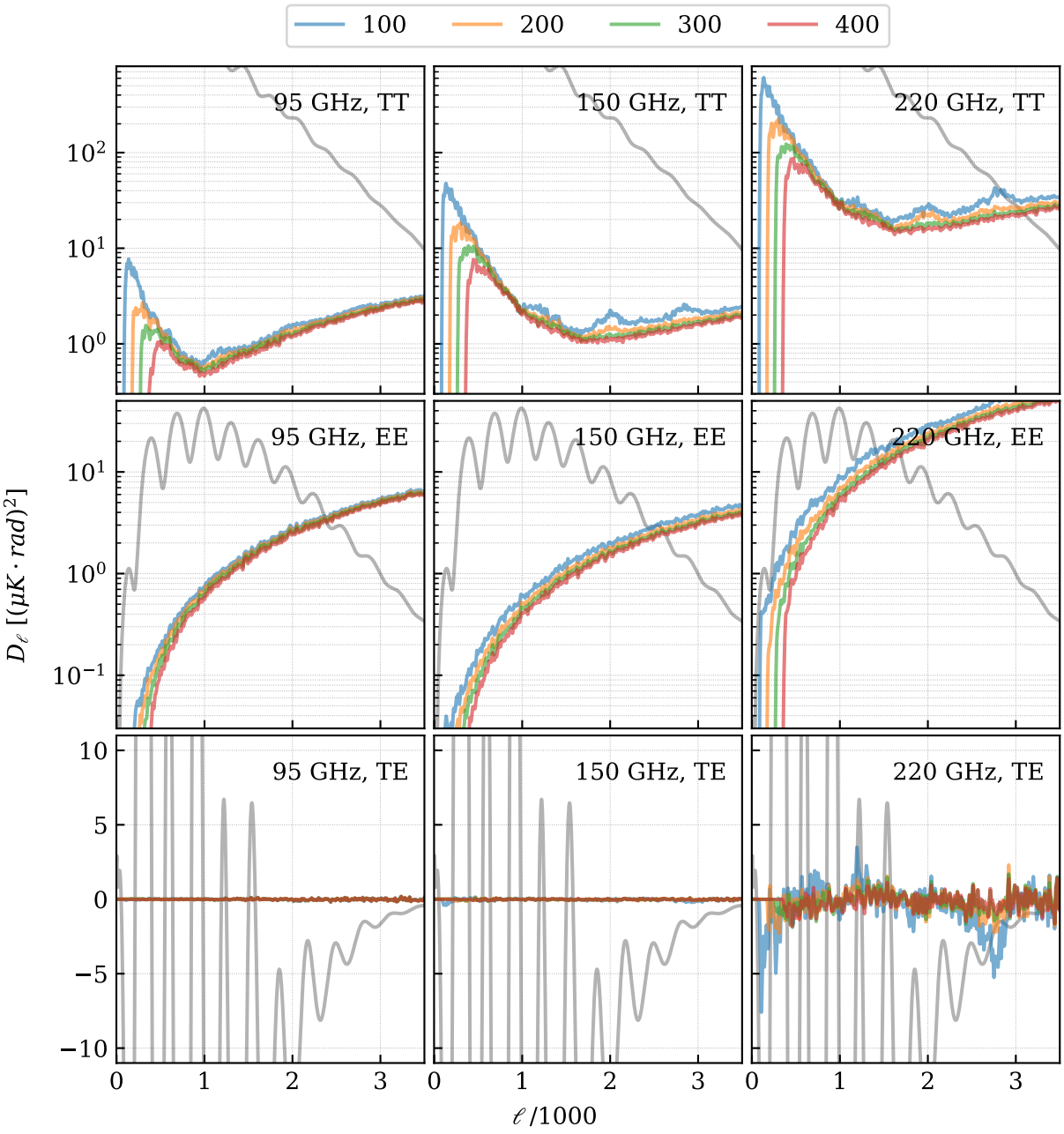

Figure 4.2. $EE/TE/TT$ noise spectra (D_ℓ) obtained from different high-pass filters. The spectra shown in figure 4.1 were multiplied by $\ell(\ell+1)/(2\pi)$ and divided by 18. *Planck*'s best-fit theoretical $EE/TE/TT$ spectra of the anisotropies of the CMB are shown as gray curves.

4.2 Map Calibration

After we made the coadds, we needed to apply small corrections to them to reduce systematic errors. These systematic errors were caused by our lack of accurate knowledge of certain detector properties that we needed to specify during the mapmaking. The small corrections included calibrating the T, Q, and U coadds by multiplying them by factors somewhat different from unity and cleaning the Q and U coadds by subtracting small copies of T coadds from them.

4.2.1 Gain

One of the detector properties of which we did not have accurate knowledge is what we call the gain of a detector. It is the change in the electrical power dissipated on a detector in response to a unit change in the temperature of the radiation incident on the detector. To be more precise, the words *temperature of the radiation* mean the equivalent CMB temperature fluctuation of the intensity of the radiation in the frequency band of the detector and along the polarization direction of the detector. As discussed in subsection 3.2.3, an early step of the timestream processing during the mapmaking was to use the gain of a detector to convert its timestreams' unit from W to μK.

We measured the gain of each detector regularly throughout an observing season by scanning the detector across an astrophysical source that has a known equivalent CMB temperature fluctuation and recording the change in the electrical power, but this known temperature is in fact not very accurate. It is a value that we obtained by analyzing coadds of the source made from SPT-SZ data, and this value is not necessarily accurate for the purpose of measuring the gain of an SPT-3G detector because the SPT-SZ frequency bands were similar but not identical to the SPT-3G frequency bands. SPT-SZ also had three frequency bands centered at around 95, 150, and 220 GHz, but the two cameras have slightly

different band center frequencies, widths, and shapes. As a result, the effective equivalent CMB temperature fluctuation (the integral of the product of the right-hand side of equation 3.10 and a transmission spectrum) of the source in one frequency band of SPT-SZ is slightly different from the source temperature in the corresponding frequency band of SPT-3G. In addition, individual SPT-3G detectors within the same frequency band have slightly different transmission spectra, so the source has slightly different equivalent CMB temperature fluctuations for different SPT-3G detectors as well. Because we calculated the equivalent CMB temperature fluctuation of the source from each SPT-SZ frequency band and used that single temperature to estimate the gains of all the SPT-3G detectors in the corresponding frequency band, we suspected that there was a gain misestimation factor (an estimated gain divided by the true gain) associated with each detector.

Using misestimated gains when making maps can cause two systematic errors in the maps. In a simple situation where there are only two orthogonal and noiseless detectors that measure the T and Q parameters, if both detectors' gains are correct, then they correctly measure the two parameters, which may have the following expressions:

$$T = T_\alpha + T_\beta,\ Q = T_\alpha - T_\beta, \tag{4.1}$$

where T_α and T_β are the equivalent CMB temperature fluctuations of the intensities measured by the two detectors. If the two detectors' gains are misestimated by factors $g_a + g_d$ and $g_a - g_d$, respectively, where g_a is the average of the two misestimation factors, and $2g_d$ is the difference, then the misestimated Stokes parameters, T' and Q', have the following expressions:

$$T' = (g_a + g_d)T_\alpha + (g_a - g_d)T_\beta = g_a(T_\alpha + T_\beta) + g_d(T_\alpha - T_\beta) = g_a T + g_d Q, \tag{4.2}$$

$$Q' = (g_a + g_d)T_\alpha - (g_a - g_d)T_\beta = g_a(T_\alpha - T_\beta) + g_d(T_\alpha + T_\beta) = g_a Q + g_d T. \tag{4.3}$$

Because the CMB is mostly unpolarized, and g_d is expected to be small relative to unity, $T' \approx g_a T$. Then, one systematic error caused by the misestimated gains is that both T' and Q' contain miscalibrated versions of the true values (T and Q) by the factor equal to the average gain misestimation factor. The other error is that Q' is also contaminated by a small copy of the true temperature value ($g_d T$), and the size of the contamination is determined by the difference between the two gain misestimation factors (Hu et al. [2003]). In a real situation where there are many pairs of orthogonal detectors and many gain misestimation factors, there are effective g_a and g_d associated with the entire detector array, and there still exist the two types of systematic errors shown in the simple situation: a miscalibration of a set of T, Q, and U coadds by the same factor and leakages of small copies of the T coadd into the Q and U coadds. We checked both errors using our full-depth and half-depth coadds and corrected for the errors in those coadds and the bundles.

4.2.2 Overall Calibration

Correcting for the overall miscalibrations of our T, Q, and U coadds comprised two steps, First, we compared our T coadds with *Planck*'s T coadds, which are known to have very accurate calibration. Then, we multiplied our T, Q, and U coadds by numbers within 10% of unity as the result of the comparisons.

The initial comparison was between our 150 GHz full-depth T coadd with *Planck*'s 143 GHz full-depth T coadd. *Planck* has nine frequency bands, and its three bands that are close to ours are centered at around 100, 143, and 217 GHz. The 143 GHz full-depth T coadd has the lowest noise level of the three full-depth T coadds, so we compared the 143 GHz coadd with the corresponding coadd of ours, our 150 GHz full-depth T coadd. Because both coadds are expressed in the unit of the equivalent CMB temperature fluctuation, and the anisotropies of the CMB is the same at all frequencies when expressed in this unit, directly comparing two coadds in different frequency bands in this case does not have an issue similar

to the one discussed above about the difference between SPT-3G and SPT-SZ. We wanted to know what factor our 150 GHz coadd should be multiplied by so that it looks as close as possible to the *Planck* coadd. The *Planck* coadd covers the full sky, but it was only the small part of the coadd that coincides with our field that was relevant in this comparison.

The method that we used to estimate what factor we should multiply our coadd by was to calculate a ratio of two cross-correlation spectra as follows:

$$T_{cal,\,150}(\ell) = \frac{C_\ell^{TT,\,SPT\,full\times Planck\,full}}{C_\ell^{TT,\,SPT\,half1\times SPT\,half2}} = \frac{\sum_m \Re(T^*_{\ell m,\,SPT\,full}\,T_{\ell m,\,Planck\,full})}{\sum_m \Re(T^*_{\ell m,\,SPT\,half1}\,T_{\ell m,\,SPT\,half2})}, \quad (4.4)$$

where the numerator is the cross-correlation spectrum between the SPT-3G 150 GHz and *Planck* 143 GHz full-depth T coadds, and the denominator is the cross-correlation spectrum between a pair of SPT-3G 150 GHz half-depth T coadds. At each ℓ, this ratio can essentially be regarded as a simple expression constructed from two numbers s and p, and the expression is simply $(sp)/(ss)$, or p/s. The two numbers represent measurements of the CMB temperature anisotropy by the two experiments, so this ratio is the factor by which the two measurements differ. In the denominator, we calculated the cross-correlation spectrum of a pair of half-depth coadds rather than the autocorrelation spectrum of the full-depth coadd to avoid the type of the bias discussed in subsection 3.3.3. After we corrected the cross-correlation spectra for the multiplicative biases discussed in subsection 3.3.4 associated with both experiments' coadds, we saw that $T_{cal,\,150}(\ell)$ had small fluctuations around a constant value in an ℓ range in which the CMB temperature anisotropy is measured with high signal-to-noise rations and dominates the anisotropy of other sources ($600 < \ell < 1200$, for example). We estimated this constant value, which we called $T_{cal,\,150}$, and multiplied each of our 150 GHz full-depth T, Q, and U coadds by this calibration factor. The same multiplication was applied to the half-depth coadds and bundles as well. In fact, instead of estimating one calibration factor for the entire field, we estimated one factor for each of the four subfields. Because we saw somewhat statistically significant differences between some

of the subfields, we multiplied different areas of the coadds by different factors.

Once we calibrated the 150 GHz coadds, we compared our 95 and 220 GHz half-depth T coadds with the 150 GHz half-depth T coadd to correct for the overall miscalibrations in those two frequency bands. We did not use *Planck* 100 and 217 GHz coadds because they have higher noise levels. For these comparisons, we calculated ratios similar to the one shown in equation 4.4. For example, to obtain a calibration factor for the 220 GHz coadds, we calculated the following ratio:

$$T_{cal,\,220}(\ell) = \frac{C_\ell^{TT,\,SPT\,150\,half1\times SPT\,150\,half2}}{C_\ell^{TT,\,SPT\,150\,half1\times SPT\,220\,half2}}. \tag{4.5}$$

In the denominator, we did not use the full-depth coadd from each frequency band because there was correlated noise between different bands. As was the case with $T_{cal,\,150}(\ell)$, $T_{cal,\,220}(\ell)$ and $T_{cal,\,95}(\ell)$ also had small fluctuations around constant values. We estimated these values, called them $T_{cal,\,220}$ and $T_{cal,\,95}$, and used them as factors to multiply our coadds by. These calculations were also done on the subfield-by-subfield basis. Because we again saw somewhat statistically significant differences between some of the subfields, we multiplied different areas of the 95 and 220 GHz full-depth and half-depth T, Q, and U coadds and bundles by different factors.

As the result of correcting for the overall miscalibrations of our T, Q, and U coadds, we multiplied the 95, 150, and 220 GHz coadds by factors ranging from 1.06 to 1.08, from 1.00 to 1.03, and from 0.98 to 1.01, respectively. Our estimates of the uncertainties on these factors ranged from 0.5% to 1.0% of the factors. The estimates were based on noise fluctuations in the coadds used to calculate the ratios of the cross-correlation spectra, After creating these corrected coadds, we proceeded to another step: removing the temperature-to-polarization leakages from the corrected coadds.

4.2.3 Temperature-to-Polarization Leakage Removal

Correcting for the temperature-to-polarization leakages also comprised two steps, First, we calculated the sizes of copies of T coadds contained in Q and U coadds by cross-correlating T coadds with Q and U coadds. Second, we subtracted approximately 1% of T coadds from Q and U coadds as the result of the calculations.

We calculated the sizes of the leakages by using a linear least-squares method in which the parameters to estimate included the sizes of the leakages. To calculate how much of T coadds leaked into Q and U coadds in each frequency band, we constructed the following model:

$$C_\ell^{TP,\,half1\times half2} = P_{leak}\, C_\ell^{TT,\,half1\times half2} + P_{non\,leak}\, C_\ell^{TP,\,non\,leak}. \tag{4.6}$$

In this model, P denotes either of the two polarization Stokes parameters, Q and U. The left-hand side is the cross-correlation spectrum between a half-depth T coadd and the half-depth P coadd from the other half. Here, we can treat the P coadd as a spin-0 function and calculate its spin-0 spherical harmonic coefficients ($Q_{\ell m} = \int Q(\hat{\boldsymbol{n}})\, Y^*_{\ell m}(\hat{\boldsymbol{n}})\, d\hat{\boldsymbol{n}}$, for example). This cross-correlation spectrum comprises two components. Assuming the P coadd contains a small copy of the T coadd in the same half, $C_\ell^{TP,\,half1\times half2}$ should contain a small copy of the cross-correlation spectrum between the two half-depth T coadds, $C_\ell^{TT,\,half1\times half2}$. This small copy is represented by the first term on the right-hand side, where P_{leak} is the size of the leakage that we want to estimate. The second term on the right-hand side contains an estimate of the TP spectrum of the anisotropies of the microwave sky, which I label as $C_\ell^{TP,\,non\,leak}$. This is not caused by the T-to-P leakage and is an astrophysical signal. We obtained an estimate of $C_\ell^{TP,\,non\,leak}$ from mock-observation output maps. We do not simulate T-to-P leakages in a mock observation, so we can calculate C_ℓ^{TP} from a set of mock-observation output T, Q, and U maps and use the spectrum to approximate $C_\ell^{TP,\,non\,leak}$

contained in our real data. Because the P coadd still needed a further calibration at this point (the topic of the next subsection), and the mock-observation output maps were based on properly calibrated simulated skies, we introduced a free parameter that adjusts the amplitude of $C_\ell^{TP,\,non\,leak}$ to absorb the miscalibration of the P coadd. That parameter is labeled as $P_{non\,leak}$ in the model.

Using this model and the three cross-correlation spectra, we estimated both P_{leak} and $P_{non\,leak}$ in each frequency band with a linear least-squares method, and we used P_{leak} to clean the leakages in the full-depth, half-depth, and bundle P coadds in this frequency band by subtracting the product of P_{leak} and the corresponding T coadds from the P coadds. As is the case with the overall miscalibrations, we found statistically significant differences in the sizes of the leakages in different subfields and between Q and U, so we cleaned different subfields and Stokes parameters by using different values for P_{leak}. The values ranged from 0.0025 to 0.0185, and our estimates of the uncertainties ranged from 0.0005 to 0.0010. After creating the cleaned Q and U coadds, we proceeded to yet another step.

4.2.4 Polarization Efficiency

Besides the gain of a detector, another detector property that we did not have accurate knowledge of was what we call the polarization efficiency of a detector. The polarization efficiency of a detector represents the detector's ability to couple to only the intensity along the direction aligned with the detector's angle, or the ability to reject the intensity along the orthogonal direction. If the detector does not couple to the intensity along the orthogonal direction at all, the detector has 100% polarization efficiency. The more the detector couples to the intensity along the orthogonal direction, the lower its polarization efficiency.

The model in equation 3.1 has only the intensity along the direction aligned with the detector's angle and thus assumes that the detector has 100% polarization efficiency, but our detectors do not have the perfect efficiency. A more realistic model includes the intensity

along the orthogonal direction as well and has the following expression:

$$\begin{aligned} I_\alpha &= (E_y \cos\psi_\alpha + E_x \sin\psi_\alpha)^2 + \epsilon_\alpha (E_y \sin\psi_\alpha - E_x \cos\psi_\alpha)^2 \\ &= \frac{1}{2}[(1+\epsilon_\alpha) T + (1-\epsilon_\alpha) Q \cos 2\psi_\alpha + (1-\epsilon_\alpha) U \sin 2\psi_\alpha], \end{aligned} \tag{4.7}$$

where ϵ_α is a nonzero coefficient smaller than 1.0, and the polarization efficiency of this detector is defined as $1 - \epsilon_\alpha$. This model shows that the detector measures reduced Q and U signals as a result of its imperfect polarization efficiency.

Although this model is more accurate, we did not adopt it and simply assumed that ϵ of each detector was zero during the mapmaking because we did not have accurate measurements of the quantities. As a result, even after we corrected for the overall miscalibrations and temperature-to-polarization leakages, our Q and U coadds in each frequency band were still miscalibrated.

4.2.5 Polarization Calibration

To correct for the miscalibrations of our Q and U coadds, we compared them with *Planck*'s Q and U coadds, and the procedure for these comparisons was almost the same as that used for the T coadds (the procedure discussed in subsection 4.2.2). First, we cross-correlated our 150 GHz full-depth Q and U coadds with *Planck*'s 143 GHz full-depth Q and U coadds to obtain $Q_{cal,150}$ and $U_{cal,150}$, which are the Q and U versions of $T_{cal,150}$. In these cross-correlation spectrum calculations, the Q and U coadds were treated as spin-0 functions. We calculated $Q_{cal,150}$ and $U_{cal,150}$ on the subfield-by-subfield basis but did not find statistically significant differences between the eight calibration factors (Q and U for each of the four subfields). Therefore, we calculated a weighted average of the eight numbers, which we called $P_{cal,150}$, and applied it to all the 150 GHz Q and U coadds (full-depth, half-depth, and bundles). Second, we cross-correlated our 95 and 220 GHz half-depth Q and U coadds

with the calibrated 150 GHz half-depth Q and U coadds. For both 95 and 220 GHz, we found statistically significant differences between the eight calibration factors. However, the differences were still small relative to our estimate of the uncertainty in $P_{cal,150}$, and we decided to use only one calibration factor in each frequency band for simplicity.

As the result of correcting for the miscalibrations of our Q and U coadds, we multiplied the 95, 150, and 220 GHz coadds by 1.07, 1.08, and 1.19, respectively. There is still an ongoing discussion on the uncertainties in these numbers, but they are expected to be approximately 0.02. Our estimates of the uncertainties in the polarization and overall miscalibration factors will be used in the prior probability density functions (of the parameters that modify the band power amplitudes) discussed in subsection 3.4.1.

Besides the overall calibration, temperature-to-polarization leakage removal, and polarization calibration, another correction that we applied was what we call polarization rotation. The detector property relevant to this correction was the angle of a detector. The angle of each detector is determined by two factors: the overall orientation of the collection of the 10 wafers and the orientation of the detector's antenna on the wafer the to which the detector belongs. The angles that we specified during the mapmaking were based on our knowledge of how we installed the wafers and how the antennae were lithographed onto the wafers. Because we did not measure and verify each detector's angle after we installed the wafers, there was the possibility that each angle that we specified had an offset from the true value. If the average offset over all the detectors is zero, the variance of the offsets causes our Q and U coadds to have reduced signals. Because this effect is degenerate with the effect caused by not accurately specifying the polarization efficiency of a detector, the polarization calibration discussed above corrected for the two effects at the same time. If the average offset over all the detectors is nonzero, this global offset causes our Q coadds to contain small copies of U signals, and U coadds Q signals. Because we measured the global offset to be about 0.5°, the mixing between Q and U coadds was negligible, and I will not discuss this further.

After applying the four types of corrections, we considered our coadds to be reasonably calibrated and cleaned. Some of the coadds are visualized in the next section.

4.3 Full-Depth Coadds

In this section, I show some of the calibrated and cleaned full-depth coadds that we produced by following the steps discussed in section 4.2, and I explain notable features in the coadds.

Figures 4.3–4.5 show the full-depth T coadds in the three frequency bands. The three coadds have different noise levels but generally look similar to one another. This similarity is consistent with a statement made at the end of subsection 3.2.3: when expressed in the unit of the equivalent CMB temperature fluctuation, the anisotropies of the CMB looks the same in different frequency bands. A characteristic feature of these coadds is that a hot or cold spot is not circular but elongated, and it is elongated along the direction perpendicular to the constant-declination contour passing through the location of the blob. This feature is caused by the high-pass filter that we applied to the timestreams. Because the scans and therefore the timestreams follow constant-declination contours, the high-pass filter preferentially attenuates the components of the anisotropies of the CMB that have large-angular-scale oscillations along the contours. For reference, figure 4.6 shows the *Planck* 143 GHz full-depth T coadd in the winter field. Because *Planck* coadds retain large angular-scale information, this coadd looks quite different from the SPT-3G coadds.

Figure 4.7 shows the 150 GHz full-depth T, Q, and U coadds. Unlike the previous figure, this figure shows only a small region of the field near its center so that characteristic patterns in the Q and U coadds can be seen more easily. While the Q coadd has ridges that run in the vertical direction, the U coadd has ridges that run in the diagonal directions. These patterns exist because the polarization of the CMB is dominated by the E-mode polarization rather than the B-mode. Figure 4.8 shows a simplistic model that explains this statement. Finally,

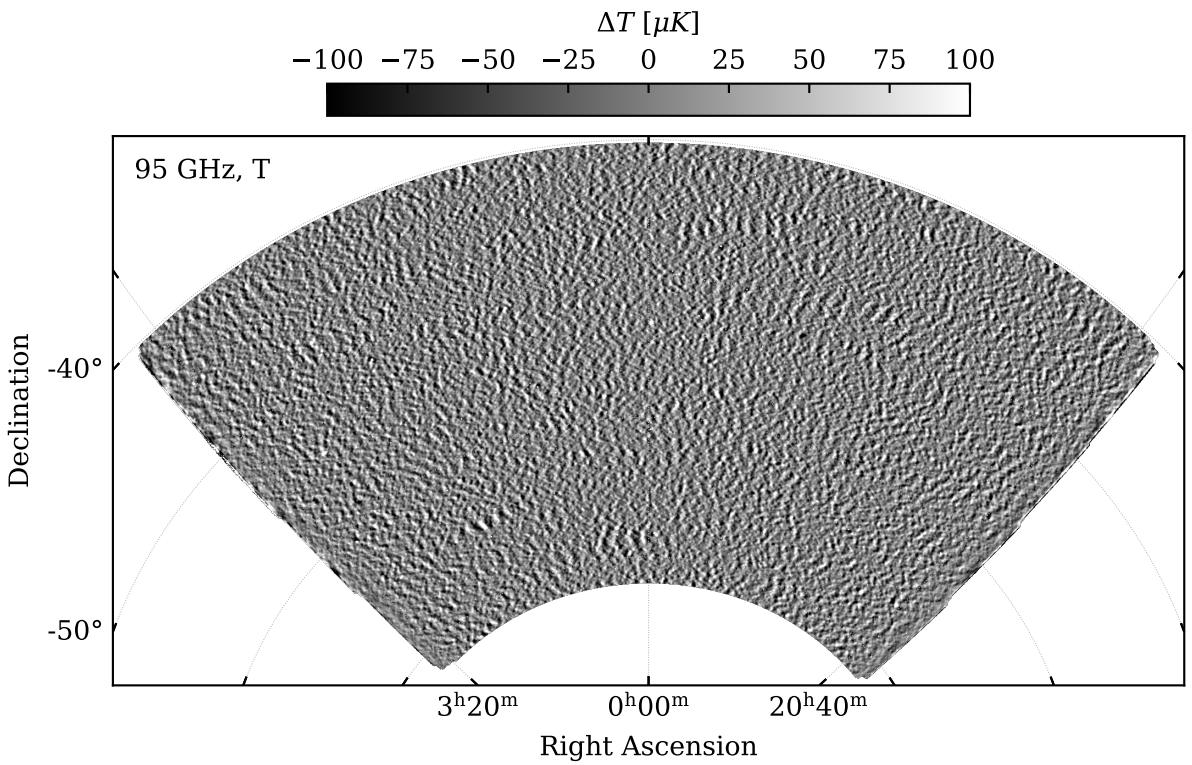

Figure 4.3. 95 GHz full-depth T coadd. Finer details can be seen when the image is enlarged.

figure 4.9 shows what the noise part of the full-depth T, Q, and U maps shown in figure 4.7 could look like. We made these maps by subtracting one set of half-depth T, Q, and U coadds from the other. (Adding these two sets of half-depth coadds gives the full-depth coadds.) These noise maps are spatial-domain representations of the types of noise spectra discussed in section 4.1. A TT noise spectrum rises as ℓ decreases, so the T noise map shown here has long-wavelength fluctuations. On the other hand, an EE noise spectrum is mostly flat, so the Q and U noise maps shown here simply have white noise fluctuations.

Figure 4.10 compares the SPT-3G 150 GHz full-depth T, Q, and U coadds with mock-observed *Planck* 143 GHz full-depth T, Q, and U coadds in a small area around the center of the winter field. By mock-observing the original *Planck* coadds, we removed the large angular-scale information in them that was absent from the SPT-3G coadds. This allowed

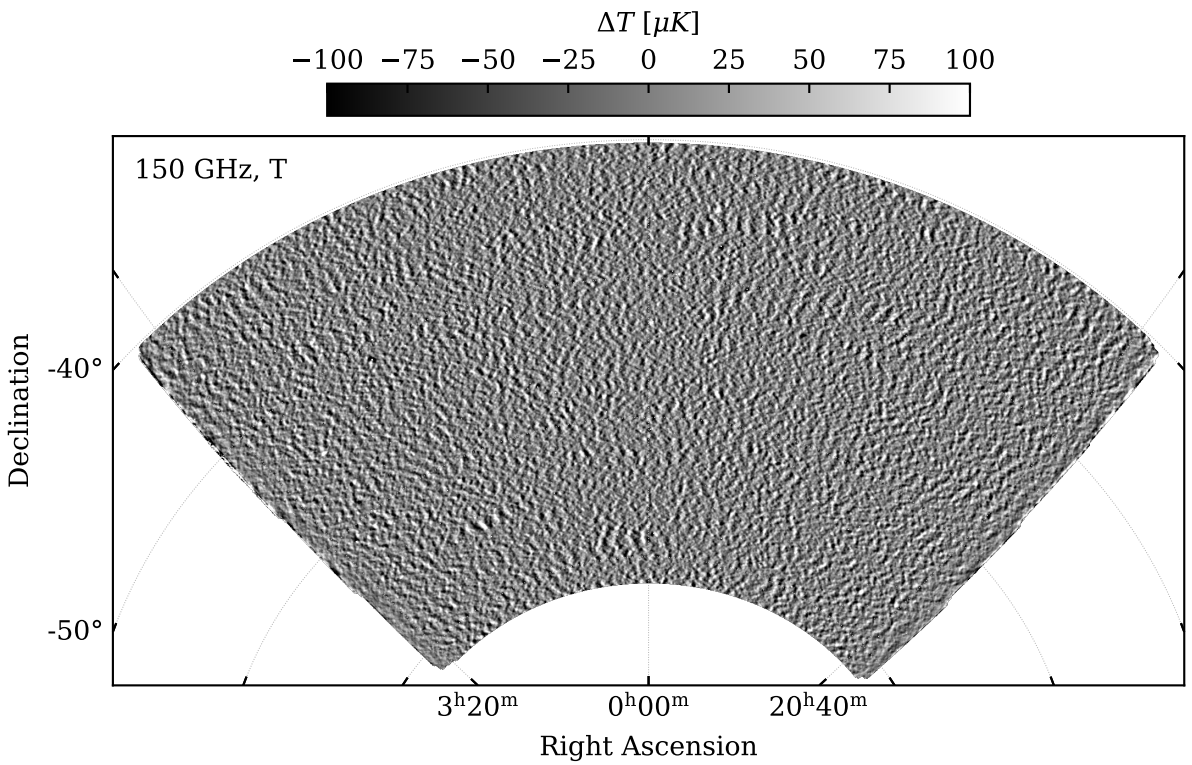

Figure 4.4. 150 GHz full-depth T coadd.

us to compare the two sets of coadds in the same range of angular scales. The two T coadds in the figure show that our maps have higher resolution than *Planck*'s maps, and the two sets of Q and U coadds show that our maps have lower noise levels than *Planck*'s maps. These differences make SPT-3G complement *Planck*.

We made nine full-depth coadds in total (three Stokes parameters and three frequency bands). The total number of pixels in each coadd is approximately 3.66×10^7. These coadds form one major part of the final analysis products that we plan to release to the public.

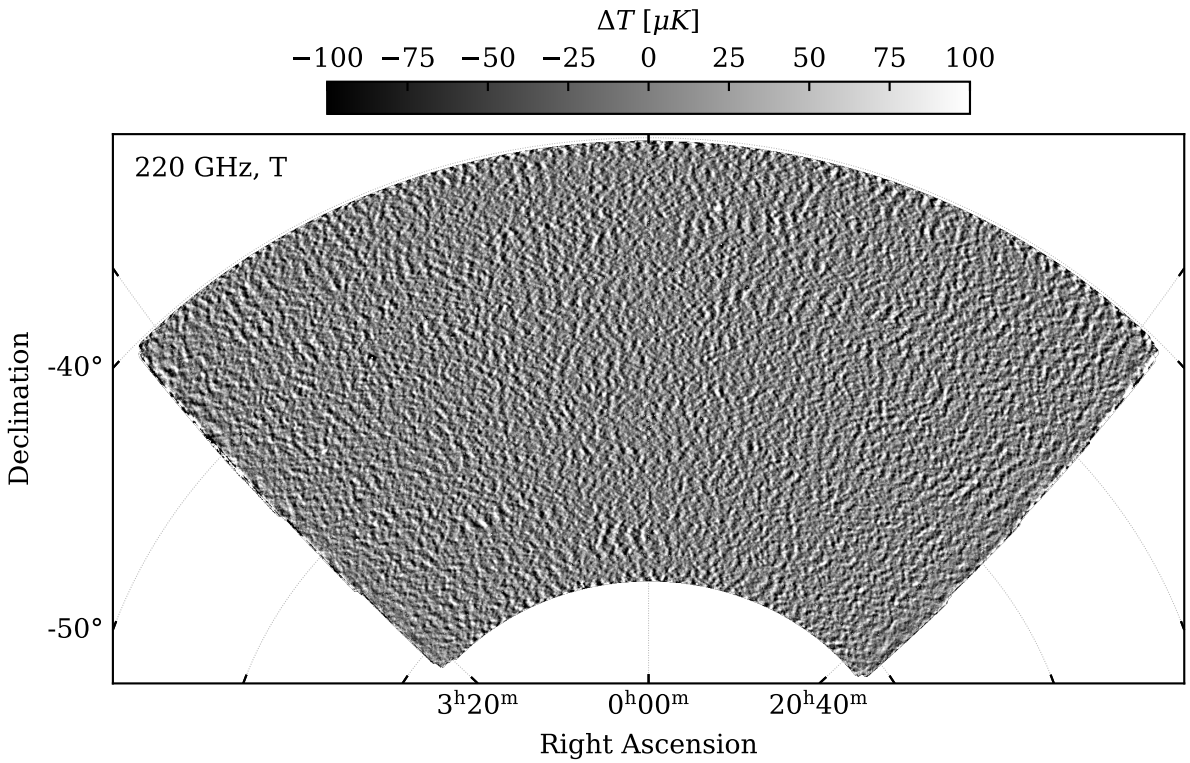

Figure 4.5. 220 GHz full-depth T coadd.

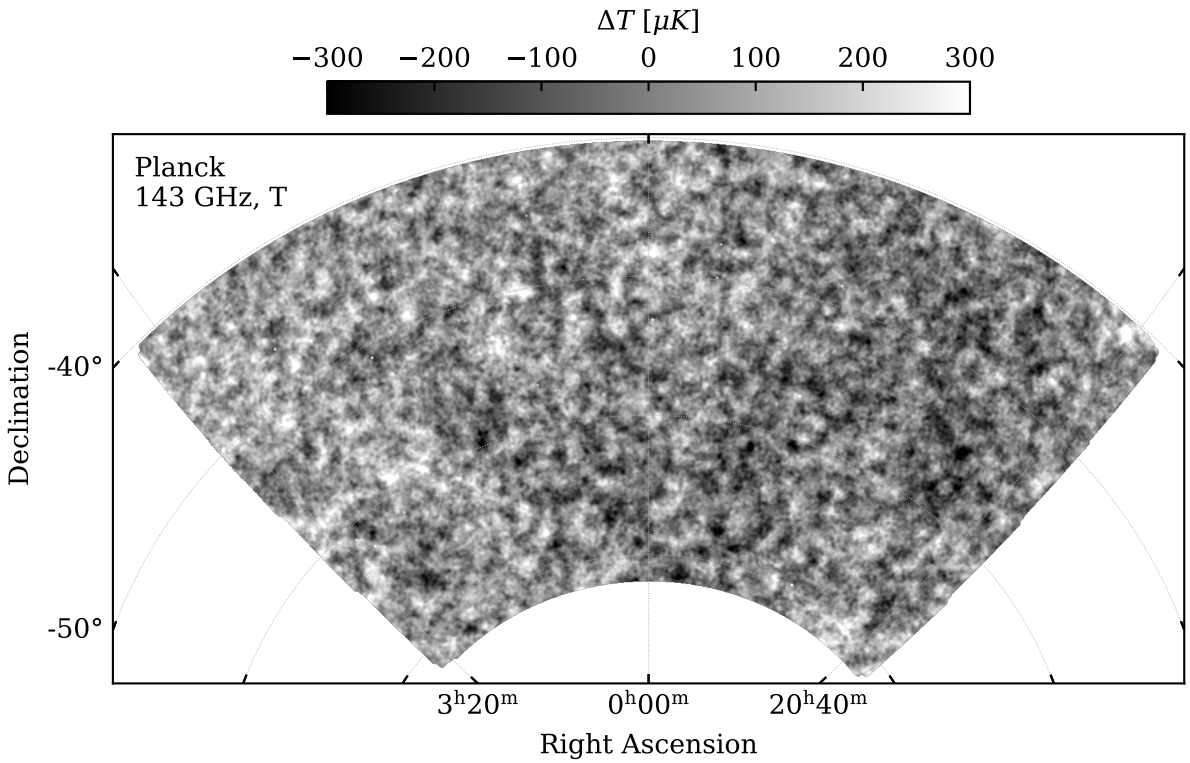

Figure 4.6. *Planck* 143 GHz full-depth T coadd in the winter field.

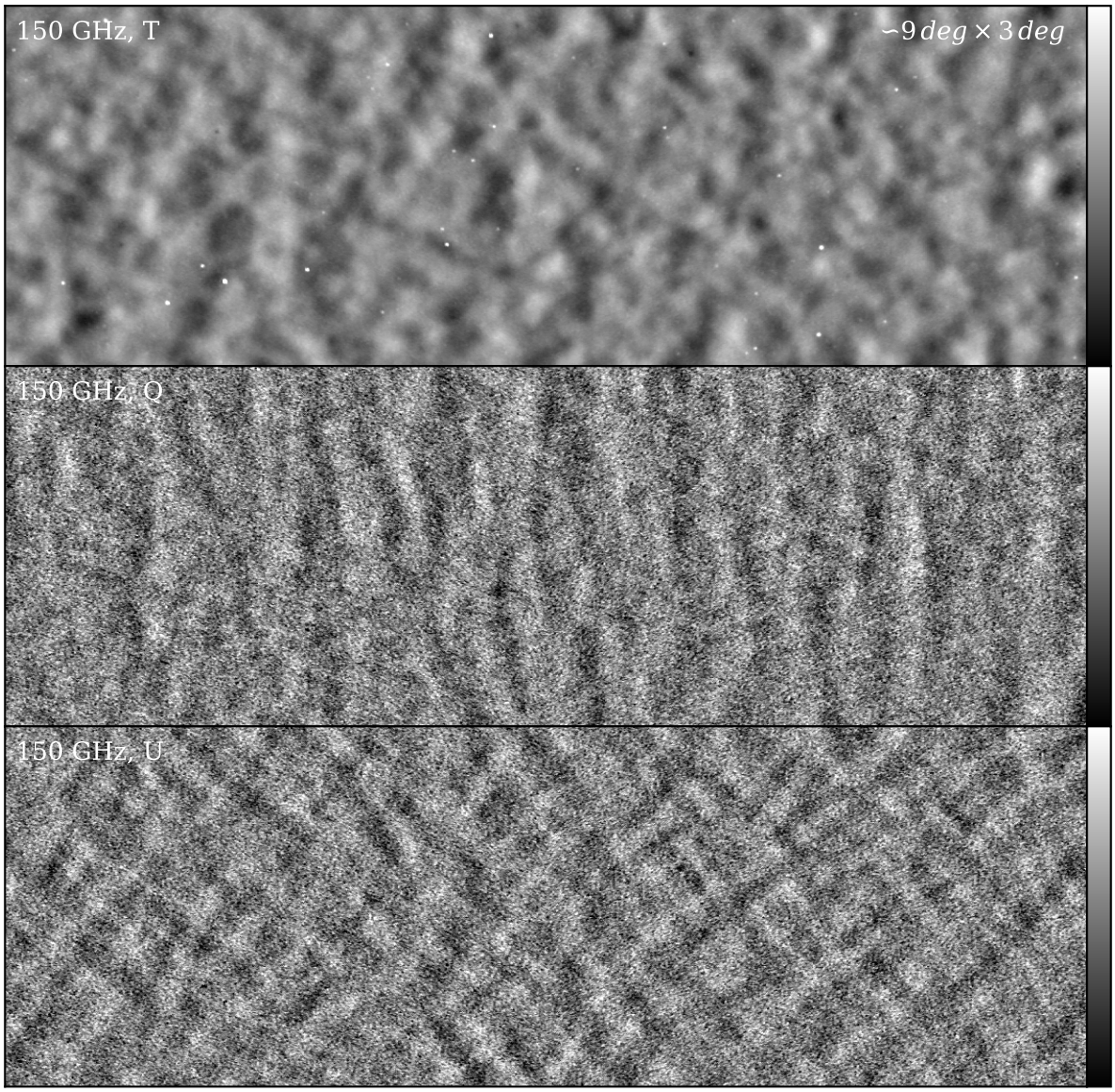

Figure 4.7. 150 GHz full-depth T, Q, and U coadds in a small region. The top left corner of each panel shows the relevant Stokes parameter. For the top panel, the temperature range represented by the gray scale is from -200 μK to 200 μK. For the other two panels, the range is from -20 μK to 20 μK. The width and height of the small region are approximately nine and three degrees, respectively.

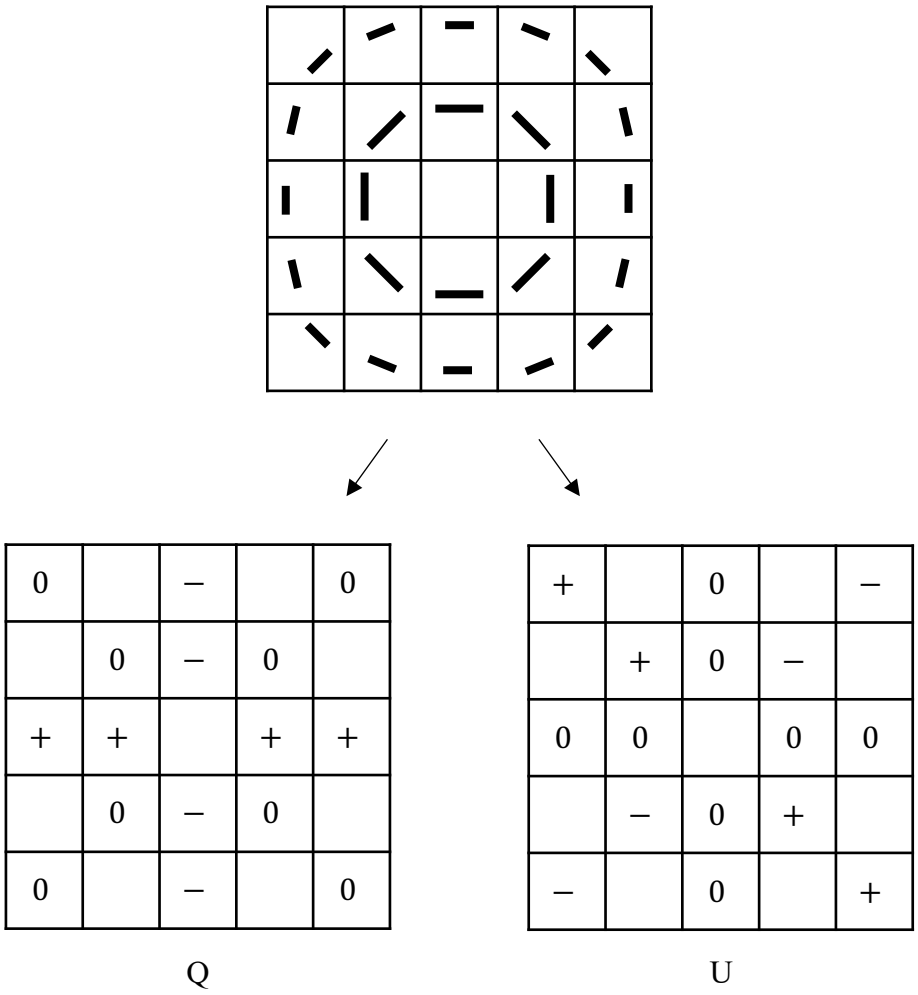

Figure 4.8. Toy model for the ridges in the Q and U coadds. In this diagram, the top square shows the polarization directions in a grid of pixels. These directions form a characteristic pattern of the E-mode polarization. In some pixels, the polarization direction is such that either the Stokes Q or U parameter is zero. This is shown in the bottom two squares. The bottom left square shows the sign of Q in some of the pixels, and the bottom right square is for U. The nonzero values in the Q map form horizontal or vertical features, and the nonzero values in the U map form diagonal features. Because the CMB has much more E-mode than B-mode polarization, we see these features clearly in our Q and U coadds.

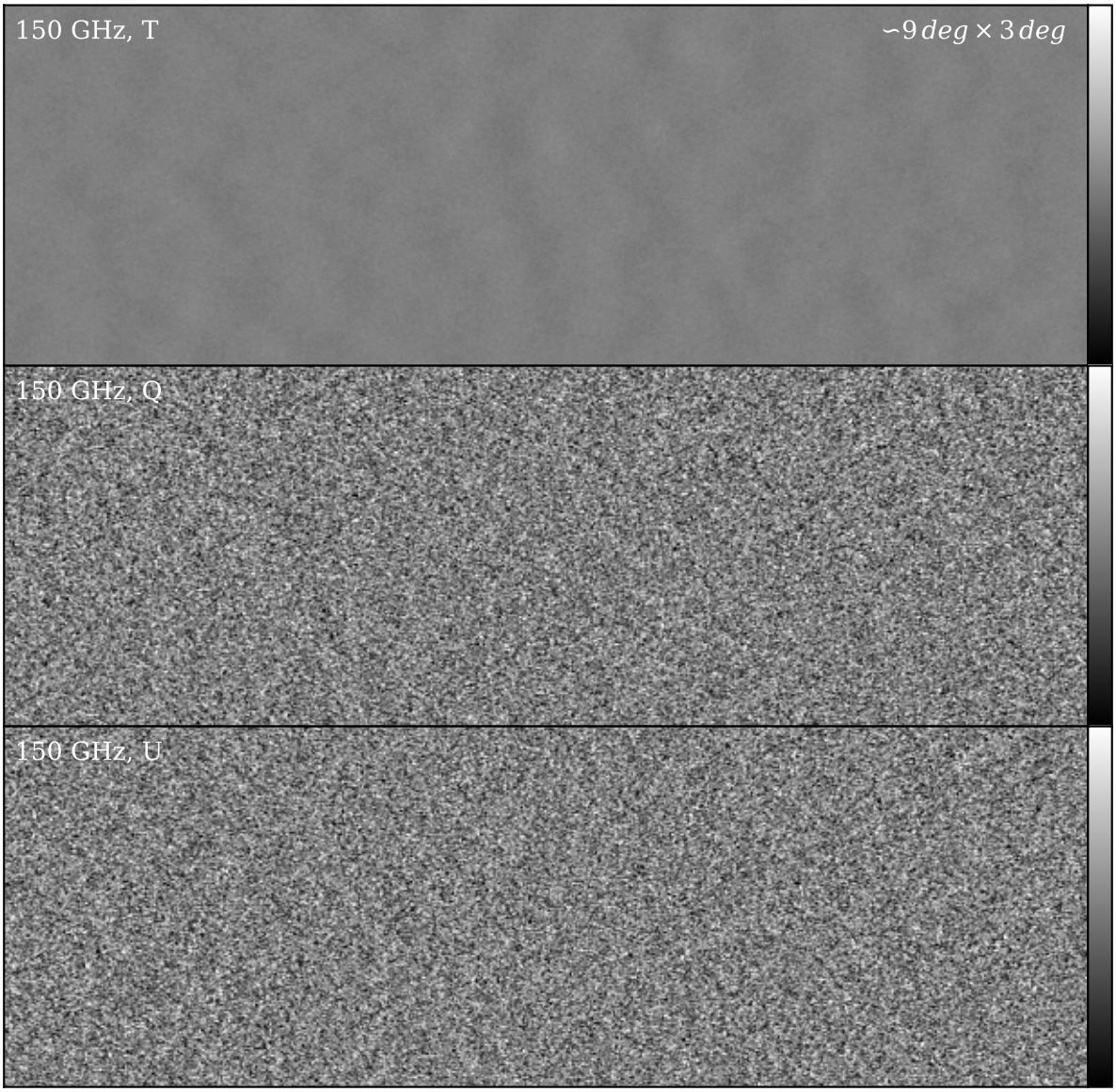

Figure 4.9. Possible noise patterns in the 150 GHz full-depth T, Q, and U coadds. This figure uses the same temperature ranges for the gray scales as figure 4.7.

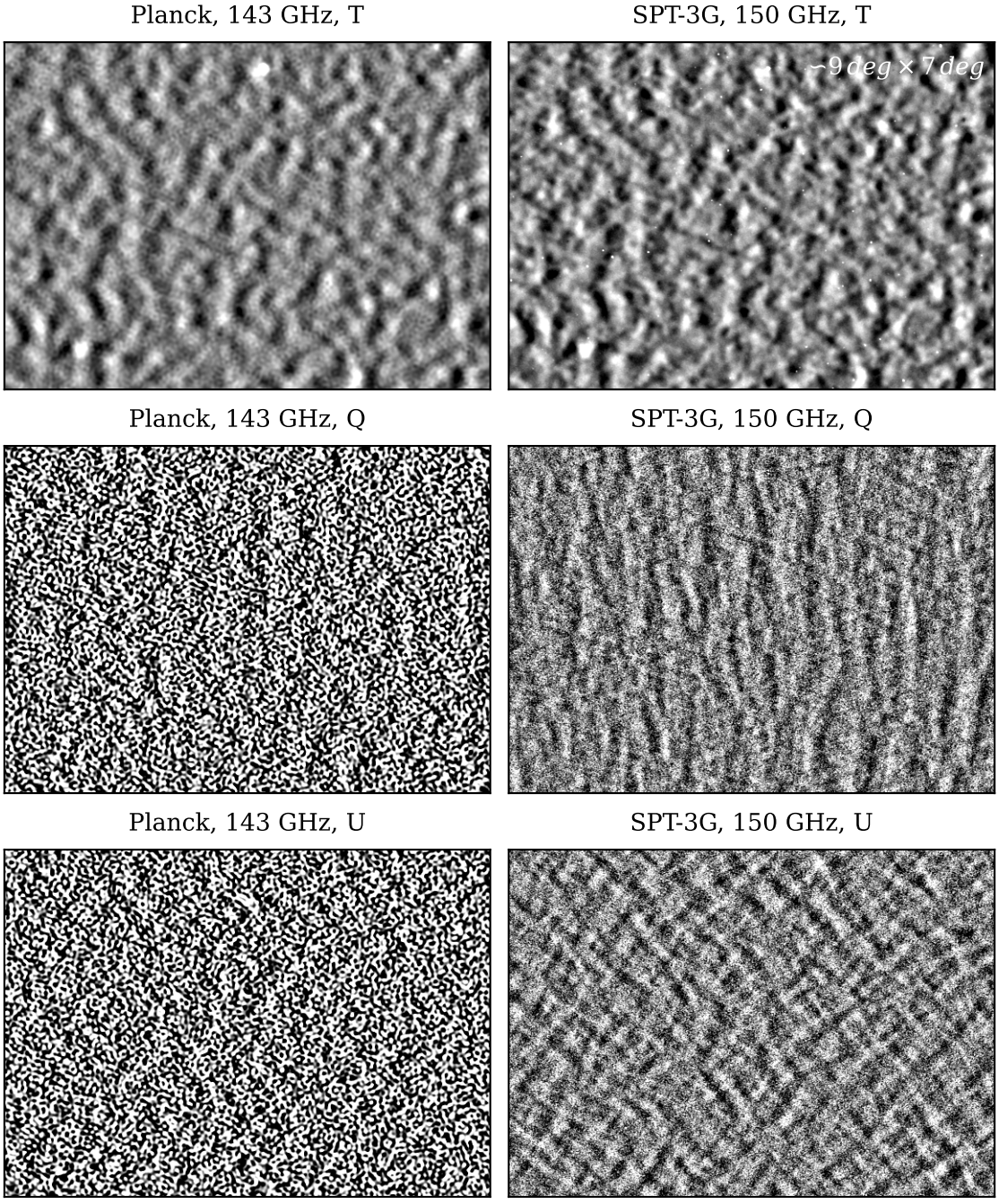

Figure 4.10. SPT-3G 150 GHz and *Planck* 143 GHz full-depth T, Q, and U coadds. The original *Planck* maps from which these mock-observed maps were made were downloaded from the Planck Legacy Archive. For the top row, the temperature range represented by the gray scale is from -100 μK to 100 μK. For the other two rows, the range is from -10 μK to 10 μK.

4.4 Null Tests

In the previous three sections, I discussed two analysis tasks closely relevant to the first major step of this analysis, making the T, Q, and U coadds from the timestreams, and showed some of the full-depth coadds.

In the following three sections, I will discuss two analysis tasks closely relevant to the second major step of this analysis, calculating the $EE/TE/TT$ band powers from the bundles, and show some of the band powers. As discussed in subsections 3.3.3–3.3.5, we calculated the average cross-correlation spectra from the properly calibrated bundles that we obtained from the first major step, and we corrected for the known multiplicative biases and searched for potential systematic errors in the spectra. Calculating the average cross-correlation spectra was simply a matter of following equation 3.18, so I will focus on the latter in the following two sections.

In this section, I further discuss the null tests introduced in subsection 3.3.5. As introduced there, we conducted null tests to probe potential systematic errors in our data.

4.4.1 Types of Tests

For this analysis, we searched for systematic errors associated with six types of potential causes. We gave the six types of null tests the following names: sun, moon, azimuth, year, scan, and wafer null tests.

As discussed in subsection 3.3.5, the purpose of the sun test was to check whether our data were contaminated by the sun's radiation. For the 2019–2020 dataset, the maps from the individual subfield observations taken between late September and the end of November of the two years formed one of the two parts that we needed to create null bundles, and the maps from the observations taken in the other months formed the other part.

The moon test was similar to the sun test. It was another test meant to check whether

the presence of a very bright object in the sky contaminated our data even when it was far from our field. For this test, one part comprised the maps from the observations taken when the moon was above the horizon, and the other other part when the moon was below the horizon. Each part had data from one half of each month of the two winter observing seasons.

The azimuth test was used to check whether our data were contaminated by the radiation from a few buildings at the South Pole station that are close to the telescope. These buildings are all approximately in the same direction from the telescope, and the corresponding azimuth angle is 150°. For each subfield observation, we assigned a representative azimuth angle to it, which was the midpoint of the azimuth range that was covered by all the scans of that observation. Then, we used all the observations whose representative azimuth angles were within ±90° of 150° to form one part and all the other observations to form the other part. Because we observed each subfield during different hours on different days, the observations of each subfield had various different azimuth angles. As a result, the two parts had maps from approximately the same number of observations.

The year test was used to check whether anything was significantly different between the data from the 2019 winter observing season and the data from 2020. We used the maps from all the observations that we took in 2019 to form one part and all the observations in 2020 to form the other part.

The scan test was used to check whether one or the other of the telescope's scanning directions (increasing-azimuth scans and decreasing-azimuth scans) introduced a systematic error in our data. As discussed in section 3.1, each subfield observation had multiple pairs of scans in the opposite directions. The two scans in a pair have not only the opposite directions but also other differences in their motions. As one example, it is always the increasing-azimuth scan that is preceded by a change in the elevation of the telescope. As another example, the decreasing-azimuth scan moves slightly faster in the azimuth than the increasing-azimuth

scan to counter the rotation of the earth and make the two scans have the same speed in right ascension. We conducted the scan test to check whether differences like these affected our coadds and band powers in some way. Although in subsection 3.2.3 it was stated that we made one set of T, Q, and U maps for each frequency band from each subfield observation during the mapmaking, that was not entirely accurate. We made one set of maps from the timestreams of all the increasing-azimuth scans of an observation and another set of maps from the timestreams of all the decreasing-azimuth scans. To conduct the scan null test, we subtracted one set of maps from the other to create null maps from that observation, and then we constructed null bundles from them. (For other analysis tasks, we combined the two sets of maps.)

Finally, the wafer test was used to check whether data from detectors on some wafers had significant systematic errors. Different wafers on the focal plane were made in different batches of fabrication in a cleanroom and have somewhat different thermal and electronic properties. For example, when we were checking data quality of timestreams, we noticed that timestreams from detectors on two out of the ten wafers had spectral lines at 1.42 Hz. One part of our cryogenic system compresses and expands helium gas at that frequency, and it appears that some detectors responded to this through some mechanism. We conducted the wafer null test to check whether differences like this introduced systematic errors in our coadds and band powers. The procedure of creating null bundles in this case was similar to the procedure used for the scan null test. First, we divided the ten wafers into two groups of five wafers. Second, for each subfield observation, during the mapmaking, we split all the timestreams by the group assignment as well as the scan direction, so in fact we made four sets of T, Q, and U maps for each frequency band from each subfield observation. Third, we combined the maps from the two scan directions for each group of wafers and then created null maps, which were then used to construct null bundles. (For the scan null test, we combined the maps from the two groups of wafers for each scan direction.)

4.4.2 Passing Criteria

For each test, we obtained nine spectra and their uncertainties. The number of null bundles created for each test was 25, and each bundle comprised a set of T, Q, and U maps in each frequency band. From these bundles, we calculated 300 ($25 \times 24/2$) cross-correlation spectra for each anisotropy combination ($EE/TE/TT$) and each frequency band. Then, for each set of 300 spectra, we binned all the spectra and calculated the average and standard deviation of them. We called the binned average spectrum a null spectrum and used the binned standard-error spectrum as the uncertainty in the null spectrum. This procedure gave us nine null spectra (three anisotropy combinations and three frequency bands) for each test.

To decide whether a null spectrum was consistent with noise fluctuations, we calculated a χ^2 value from the spectrum and the corresponding P-value, and we compared the P-value with a threshold that we agreed in advance to use to judge whether a given P-value is high enough. We calculated the χ^2 value of a null spectrum by using a standard definition:

$$\chi^2 = \sum_b \left(\frac{N_b - N_{b,\,exp}}{\sigma_b}\right)^2 = \sum_b \left(\frac{N_b}{\sigma_b}\right)^2, \tag{4.8}$$

where N_b represents a null spectrum, the sum is over all the ℓ bins of the spectrum, $N_{b,\,exp}$ is what we expect the spectrum to look like in the absence of any systematic errors, and σ_b is the uncertainty in the spectrum. As for $N_{b,\,exp}$, we chose it to be simply zero as a starting point.

What we used as σ_b to calculate the χ^2 value of a null spectrum was in fact not simply the standard-error spectrum discussed above but the quadrature sum of that and 1% of the square root of the sample variance associated with the relevant signal spectrum. For example, for a 150 GHz TT null spectrum from any test, the additional uncertainties were 1% of $\sqrt{2/n_{m,\,eff}}\, C_{b,\,avg}^{TT,\,150\times150}$, where $n_{m,\,eff}$ is $(2\ell_b{+}1)\,\Delta\ell\, f_{sky}$, an estimate of the effective number of modes within an ℓ bin. I slightly changed equation 3.18 by using b instead of ℓ to

represent ℓ bins, and ℓ_b represents the ℓ at the center of a bin. Compared with equation 2.1, the expression for the effective number of modes used here has the additional factor $\Delta\ell$ to include all the modes within a bin. The idea for this additional term was that, even if we find that a null spectrum contains some kind of systematic error larger than noise fluctuations, this systematic error is not concerning at ℓs where uncertainties in our band powers are dominated by the sample variance if the systematic error is small compared with the sample variance. At those ℓs, even if some band powers have a systematic error added to them, as long as the systematic error is small compared with the band power uncertainties, which are dominated by the sample variance, the systematic error causes a negligible amount of bias on our constraints on cosmological parameters. This statement was tested in the 2018 analysis (Balkenhol et al. [2023]). By having this additional term, we gave ourselves a margin to help us pass null tests in anticipation of finding some small systematics.

The threshold that we chose to judge whether a P-value was high enough was based on (1) a value that we thought would have been reasonable to use if we had had only one null spectrum and (2) the total number of null spectra that we calculated. If we conduct only one null test in which we calculate only one null spectrum and its P-value, we think 0.05 is a reasonable threshold to use. However, if we conduct many null tests and many null spectra and their P-values, even in the absence of any systematic errors, a large χ^2 value with a corresponding low P-value can arise by chance. Taking this look-elsewhere effect into account, we decided to use 0.05/54 (0.00093) as the threshold, where 54 was the total number of P-values that we calculated (6 tests and 9 null spectra for each test).

4.4.3 Test Results

All the sun, moon, azimuth, and year null spectra gave P-values that were higher than the threshold. Some of the spectra had high enough P-values without the additional uncertainties, and others needed the additional uncertainties to have high enough P-values.

Figure 4.11 shows the nine null spectra from the sun test, the two sets of uncertainties for each null spectrum (with and without the addition of 1% of the square root of the sample variance), and the reduced χ^2 values and P-values that are based on the two sets of uncertainties. For each of the TT null spectra (except for the 150 GHz null spectrum at relatively low ℓs), the first set of uncertainties (without the contribution from the sample variance) is too small to clearly see. The second set of uncertainties for each null spectrum is drawn with shallower colors, and it is most easily noticeable for the 95 GHz TT null spectrum. In that case, using the second set of uncertainties decreased the reduced χ^2 value from 0.88 to 0.34. For some of the other spectra, the second set of uncertainties is not visible. As for the 220 GHz TT null spectrum, for example, using the second set of uncertainties decreased the reduced χ^2 value from 0.74 to only 0.73. The 220 GHz spectra shown in the figure are the actual spectra divided by 10. Without this factor, it would be hard to see these spectra because they have much larger fluctuations For the sun test, all the nine null spectra had high enough P-values without the help of the additional uncertainties. The moon test had the same situation.

Figure 4.12 shows the nine null spectra from the azimuth test. Although the 95 and 150 GHz TT null spectra had P-values below the threshold when the additional uncertainties were not included, which meant that we did detect some systematic errors from the azimuth test, the P-values became high enough with the additional uncertainties, so we did not think those small systematic errors were problematic. The 95 GHz TT null spectrum shows that we detected an additive systematic error at the level of 0.1 $(\mu K \cdot rad)^2$ at relatively low ℓs, but the uncertainties in our 95 GHz TT band powers caused by the sample variance is at the level of 30 $(\mu K \cdot rad)^2$, so the systematic error is negligible. The year test had a similar situation. Although two null spectra had P-values below the threshold without the additional uncertainties, the values became high enough with the additional uncertainties.

However, most scan and wafer null spectra gave P-values that were too low even with

the additional uncertainties. Figures 4.13 and 4.14 show that those null spectra had large deviations from zero.

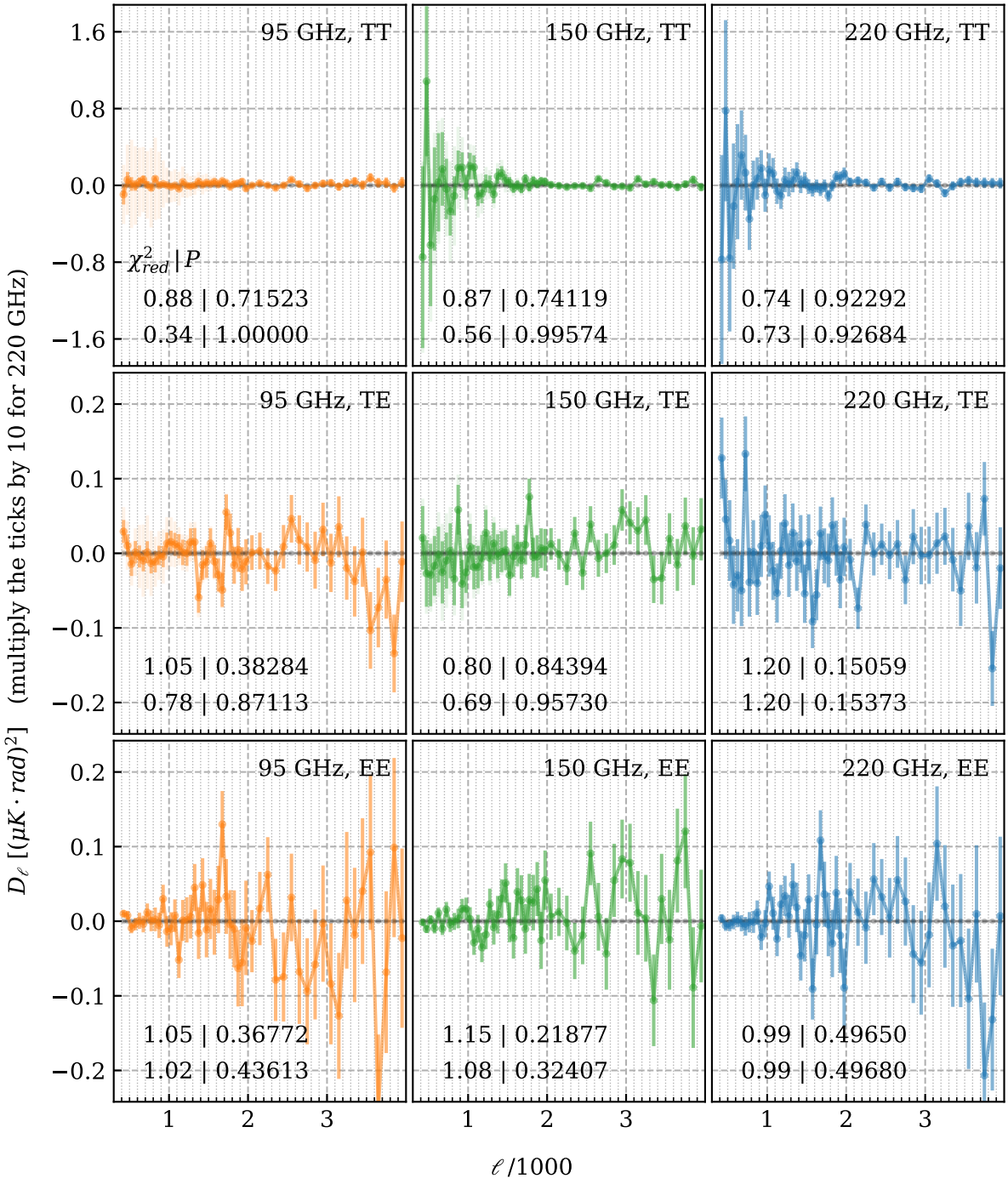

Figure 4.11. Null spectra from the sun test. Each panel shows one of the nine null spectra and the two sets of uncertainties discussed in subsection 4.4.2. The 220 GHz spectra shown here are the actual spectra divided by 10. The reduced χ^2 and the associated P-value for each set of uncertainties are also printed.

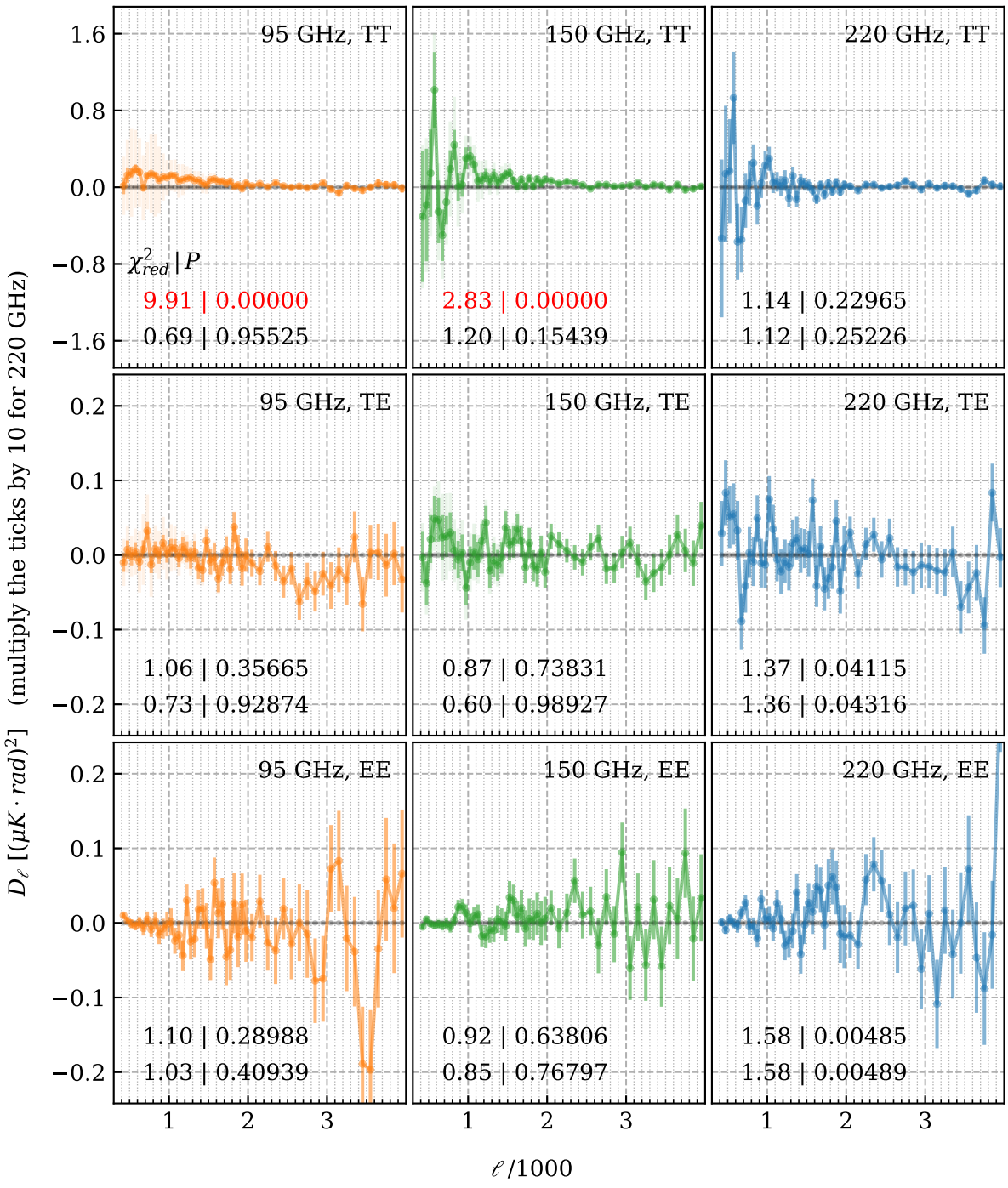

Figure 4.12. Null spectra from the azimuth test. Unlike figure 4.11, two panels in this figure have red P-values, which indicate that they are below the threshold.

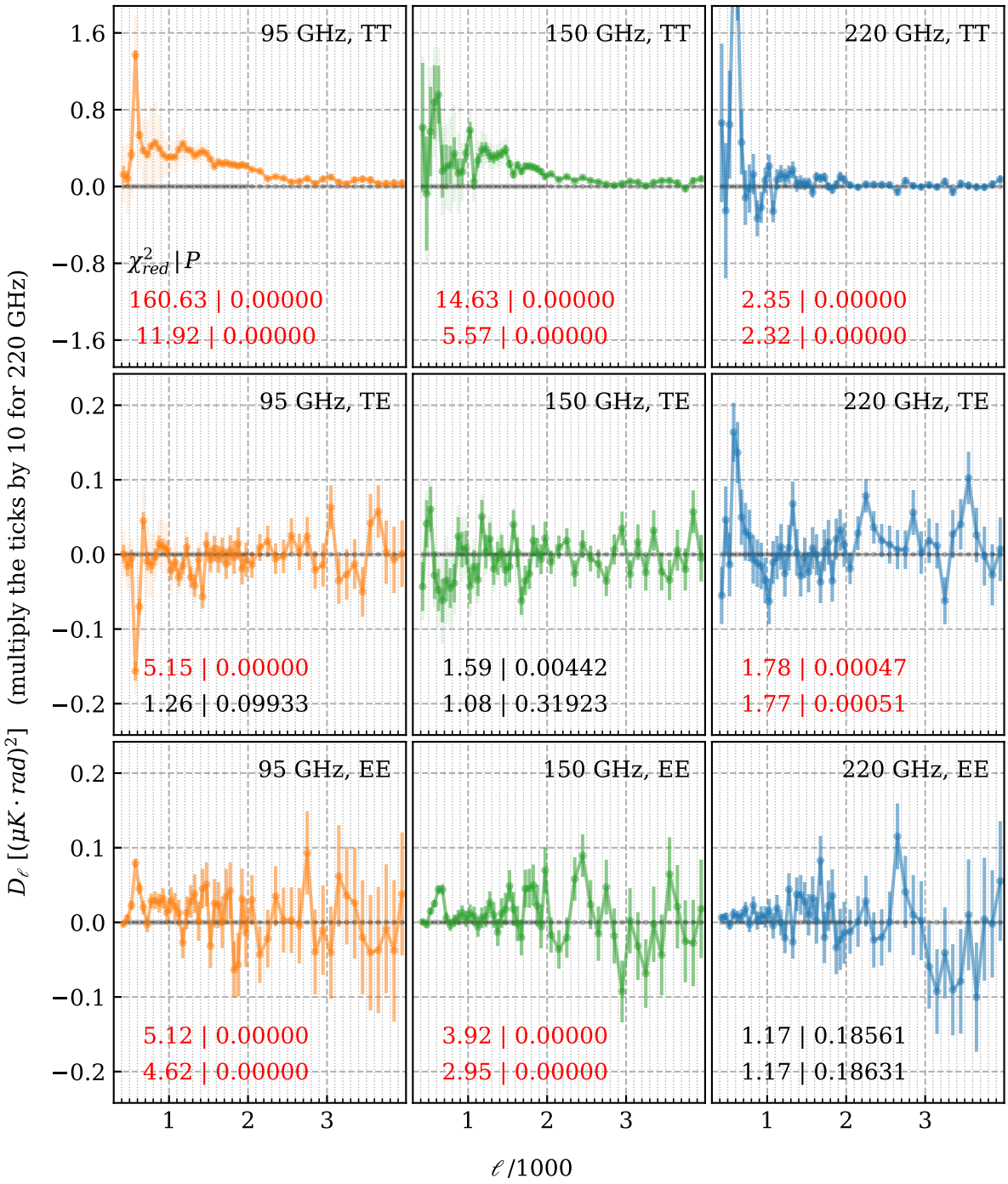

Figure 4.13. Null spectra from the scan test.

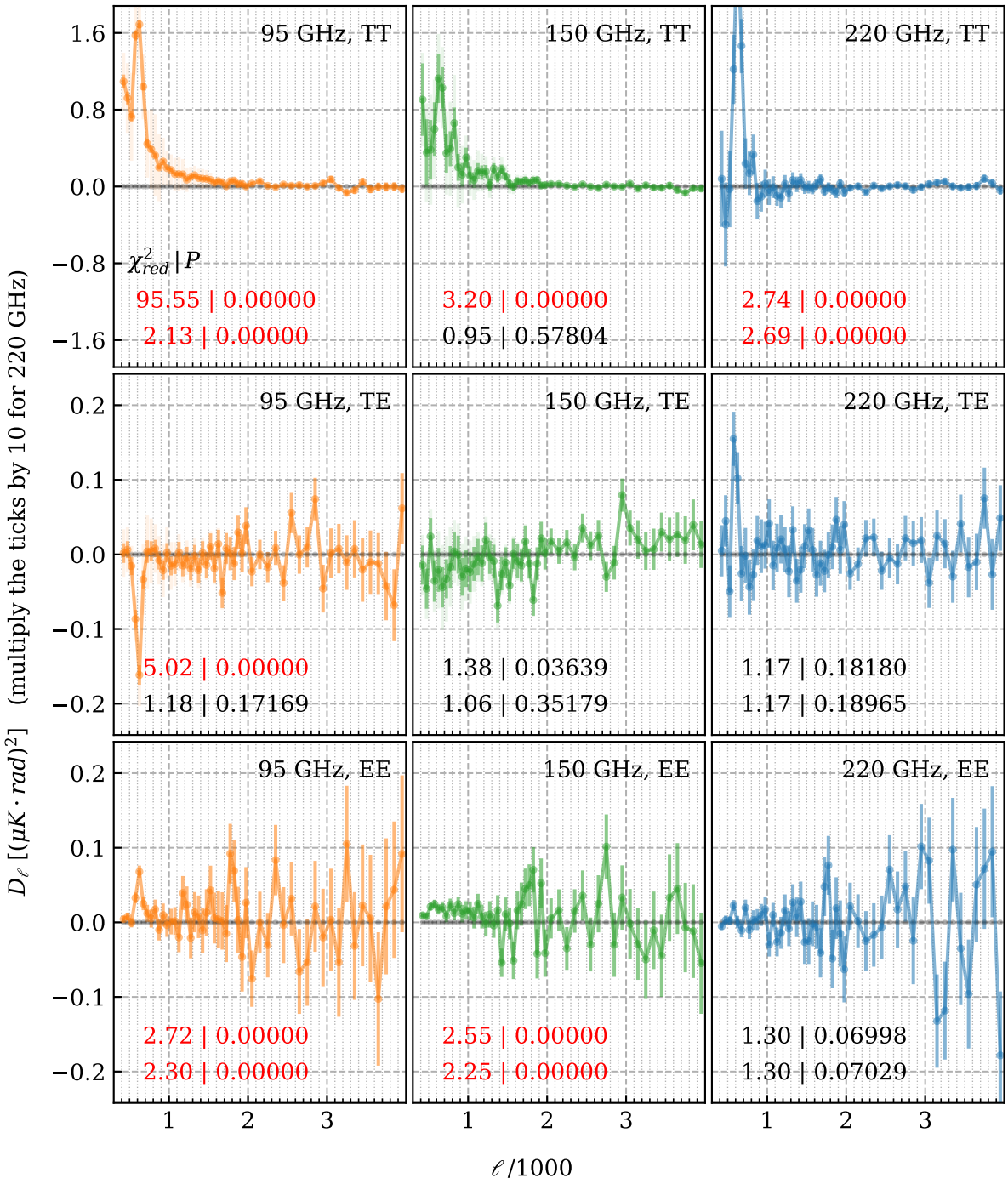

Figure 4.14. Null spectra from the wafer test.

4.4.4 Contamination Discovered in Scan and Wafer Tests

Almost all the scan and wafer null spectra revealed peaks at ℓs close to 600, and the excess power responsible for the peaks was localized along the m-axis as well. Figure 4.15 shows spherical harmonic coefficients of two 95 GHz T coadds. One coadd was a result of combining all the 25 scan null bundles, and the other coadd was from all the wafer null bundles. In both cases, the bright spots near the centers of the images were responsible for the peaks in the TT null spectra. (The one-dimensional angular power spectrum of each coadd is the result of collapsing each triangle along the vertical direction.)

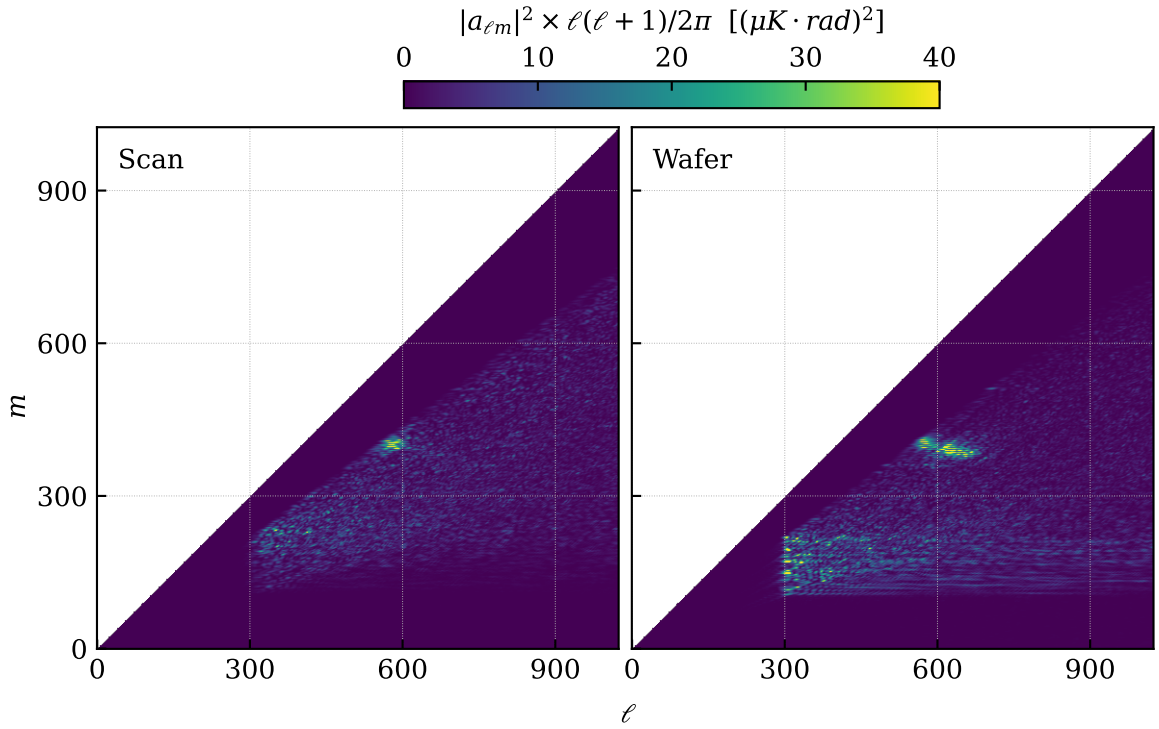

Figure 4.15. Harmonic space representation of the 95 GHz scan and wafer T null coadds. The left image is for the scan null coadd, and the right image the wafer null coadd. The square of the absolute value of each coefficient whose ℓ is smaller than 1000 is shown. Because the coadds have real values, only the coefficients of the modes that have positive m need to be shown.

Given the localization in m, we believe these peaks were caused by narrowband contam-

ination in timestreams because the frequency of a sinusoidal component in a timestream is mapped to a specific value of m as discussed in subsection 4.1.1. The relevant frequency in this case is approximately 1.1 Hz. After some investigations, we noticed an interesting property of this contamination: when we recalculated the null spectra by using a subarea of the field that had a narrower extent in right ascension (from -35° to 35° instead of from -50° to 50°), these peaks were gone. This meant that the contamination was localized in not only the harmonic domain but also the spatial domain. The contamination existed only near the left and right edges of the survey area. One hypothesis is that the motion of the telescope near the beginning and/or end of a scan was different from the motion during the middle of a scan in some way, and this difference affected timestreams from some wafers more than timestreams from other wafers. It is true that the telescope decelerates at the end of a scan, turns around, and accelerates to start a new scan in the opposite direction, but the timestreams that we recorded during the turnarounds were discarded from the dataset to begin with, so this difference should be irrelevant to the contamination. Another interesting property that we noticed was that this contamination was localized in not only right ascension but also declination. When we recalculated the null spectra by using the full range of right ascension but only the el2 and el3 subfields, the peaks were gone as well. This does not necessarily invalidates the hypothesis but is another phenomenon that we have not understood. One other interesting finding was that we saw excess power at approximately 1.1 Hz in azimuth and elevation timestreams of the telescope. However, the excess power was present throughout the entirety of a scan (not only the beginning and/or end) and for the full elevation range. Currently, it is not clear how/if the 1.1 Hz power in azimuth and elevation timestreams connects to the power in detector timestreams.

Rather than trying to have a full understanding of the exact mechanism of this contamination, we decided to move forward with the analysis by simply removing the contaminated region of the harmonics space when calculating all the null spectra from the scan and wafer

null bundles and all the signal spectra from the 30 signal bundles. This means that, after we calculated spherical harmonic coefficients of bundles, we set the coefficients of the contaminated spherical harmonics to zero before calculating one-dimensional cross-correlation spectra. In the 2018 analysis, we did not notice any obvious 1.1 Hz contamination. It is possible that the data were too noisy for this contamination to be detected. Or it is also possible that something that we changed when we upgraded our instrument at the end of 2018 introduced this contamination.

4.4.5 Remaining Features in Scan and Wafer Null Spectra

After we removed the peaks in the scan and wafer null spectra, the TT spectra still had features that were highly inconsistent with fluctuations around zero (and to a lesser extent for EE and TE), but these remaining features are in fact not concerning. These features are not caused by some contamination but caused by imperfect subtraction of signals in the null bundles, and we do not believe the mechanisms responsible for the imperfect subtraction bias our band powers.

As for the scan test, the imperfect subtraction occurred because the maps made from the timestreams of the increasing-azimuth scans of an observation contained signals that were slightly shifted in one direction, and the maps from the decreasing-azimuth scans in the opposite direction. There are two reasons for these shifts. One reason is that our detectors do not respond to changing optical power from the sky instantaneously. In other words, they have finite time constants. Our mathematical model of this time constant effect is the same as the model used to describe the charging and discharging of a capacitor connected in series with a resistor and a square-wave voltage source, and most of our detectors' time constants are several milliseconds. This time constant effect roughly makes signals recorded in a timestream delayed versions of the true signals, and scans in the opposite directions create these delays in the opposite directions. Another reason for the shift is that our data

acquisition system recorded a slightly wrong right ascension value for each timestream sample. The recorded coordinate was not the coordinate at which the detector was pointed when the sample was taken. Rather, we recorded the coordinate at which the detector was pointed several milliseconds prior to when the sample was taken. The second effect happened to mostly negate the first one, but there was still a residual time constant effect, and this caused the imperfect subtraction of signals in the scan null bundles.

These shifts caused the nonzero null spectra but did not introduce systematic errors in our band powers because effectively we corrected for the shifts when we corrected our band powers for the multiplicative bias caused by the beams. The signal bundles used to calculate the band powers had combined maps from the two scan directions. Because the two sets of maps had signals shifted in the opposite directions. combining the maps caused an additional smearing of signals. Equivalently, we broadened our beams. However, because the shifts were present in the maps of planets and galaxies that we used to measure our beams, the broadening effect was included in our beams.

As for the wafer null test, the imperfect subtraction occurred because the high-pass filter that we applied to timestreams from one wafer was slightly different from the high-pass filter for another wafer. As discussed in subsection 4.1.2, the cutoff frequency of the high-pass filter used for a given scan was a function of the elevation of the telescope during that scan so that we could achieve the same angular-scale cutoff across the full field. To be more precise, the elevation of the telescope was defined as the elevation at which a detector located in the center of the focal plane was pointed. Using the desired cutoff in ℓ, which we chose to be 300, and this definition of the elevation during each scan, we calculated the corresponding frequency cutoff and used that for all the detectors on the focal plane. However, the focal plane has a finite size, and it spans about two degrees in elevation. This means that we should use slightly different cutoff frequencies for different detectors on the focal plan to remove signals above the same angular scale from timestreams of different detectors for each

scan. Because that was not what we did during the mapmaking, different wafers had slightly different filter transfer functions, so some signals were still present in the wafer null bundles.

However, having different filter transfer functions for different wafers did not introduce systematic errors in our band powers because the differences were captured in our mock observations. The signal bundles used to calculate the band powers had combined maps from all the wafers, so the band powers calculated from the combined maps were biased by wafer-averaged filter transfer functions. Because we used all the wafers' pointing information during mock observations, the filter transfer functions that we obtained from the mock observations were also the wafer-average filter transfer functions.

We modeled the imperfect subtraction of signals by using analytical calculations and simulations, and the models agreed with the remaining features in the null spectra well. For example, figure 4.16 shows the models for the two 95 GHz TT null spectra.

After masking the contaminated region in harmonic space and creating models of the residual signals, we calculated the P-values of all the scan and wafer null spectra again. The values became high enough, so we succeeded in passing all the null tests and concluded this analysis task.

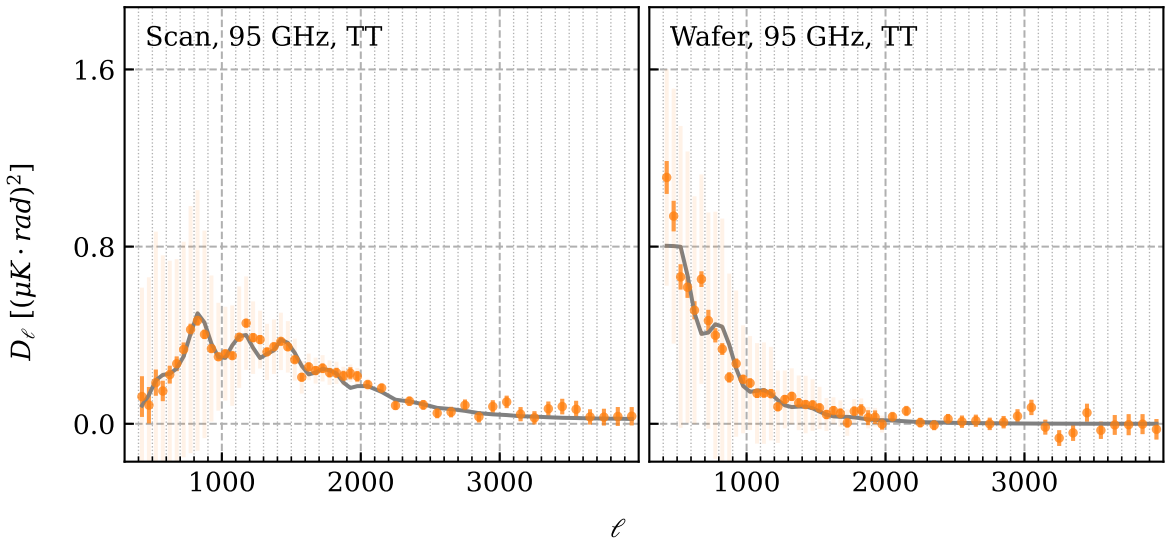

Figure 4.16. Models for the 95 GHz scan and wafer TT null spectra. The left panel is similar to the top left panel in figure 4.13, and the right panel is similar to the top left panel in figure 4.14. One difference between the null spectra shown in this figure and the null spectra shown in those two figures is that the peaks are gone because we masked the contaminated region in harmonic space. Another difference is that this figure also shows our models (gray curves) for the remaining features in the null spectra, and they agree well.

4.5 Multiplicative Biases

Another analysis task closely relevant to the second major step of this analysis is to correct for the three types of known multiplicative biases discussed in subsection 3.3.4: the filter transfer functions, beams, and pixel window function. After we calculated the average cross-correlation spectra from the bundles (see subsection 3.3.3), we removed these multiplicative biases from the spectra. The functions representing these biases that we divided our spectra by are shown in this section.

Figure 4.17 shows two filter transfer functions associated with $C_{\ell,avg}^{TT,150\times150}$, the average cross-correlation spectrum obtained by cross-correlating the 150 GHz T coadd from one bundle with that from another bundle, and these functions quantify what fraction of the

signals at each ℓ we retained as a result of the timestream high-pass filter discussed in section 4.1 and the harmonic-space masking.discussed in section 4.4. For each of the 500 simulated skies in the 150 GHz band, we calculated its TT spectrum, mock-observed it, calculated the TT spectrum of the output T coadd, and divided the latter spectrum by the former. The average of the 500 ratios is the dashed curve shown in the figure. At ℓs below 300, the value of this filter transfer function is zero because we chose the high-pass filter's cutoff value in ℓ to be 300 as discussed in section 4.1. At ℓs above 300, the function gradually approaches 1.0 as the ℓ increases. It does not abruptly reach 1.0 because the filter affects both low-ℓ and high-ℓ signals. As shown in figure 4.15, the filter removes the low-m modes in the horizontal strip in harmonic space. Because both low-ℓ and high-ℓ signals contain low-m modes, high-ℓ signals are affected by the filter as well. The solid curve in the figure shows the additional signal loss caused by the harmonic-space masking discussed in section 4.4. The masking created a notch at ℓs around 600. After we calculated $C_{\ell,\,avg}^{TT,\,150\times150}$, we divided it by the latter curve to remove the biases caused by the filtering and masking. The filter transfer functions that we used to correct the other average cross-correlation ($C_{\ell,\,avg}^{EE,\,95\times150}$, for example) were similar to the one shown here.

Figure 4.18 shows the Fourier transforms of our beams in the three frequency bands, which are labeled as B_ℓ^ν, and these functions quantify what fraction of the signals at each ℓ in each frequency band we retained as a result of finite resolutions of the telescope. The telescope has a finer resolution and retains more signals at a higher frequency because there is less diffraction. Our beams in the 95, 150, and 220 GHz bands in the spatial domain can be approximated as Gaussians whose full widths at half maximum are 1.6, 1.2, and 1.0 arc minutes, respectively. The larger this number, the more the smoothing effect. In the Fourier domain, the 220 GHz beam is closer to 1.0 at large ℓs than the 150 GHz beam, and the 150 GHz beam than the 95 GHz beam. We divided each $C_{\ell,\,avg}^{X_1X_2,\,\nu_1\times\nu_2}$ by the product of $B_\ell^{\nu_1}$ and $B_\ell^{\nu_2}$.

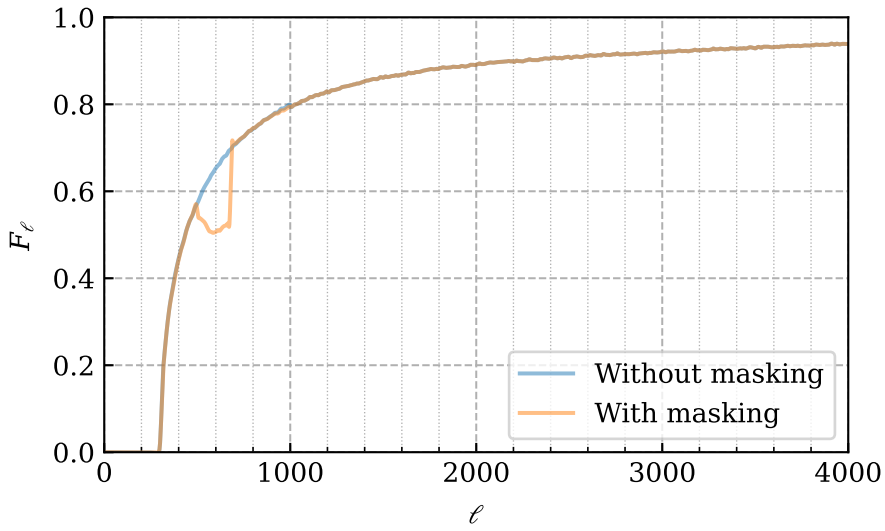

Figure 4.17. Example filter transfer function. The function that rises smoothly shows the effect of the high-pass filter, and the function with the notch has the additional effect caused by the harmonic-space masking that we implemented to remove the contamination that we found from the scan and wafer null tests. We use the notation F_ℓ to represent filter transfer functions.

Figure 4.19 shows the pixel window function associated with the pixelation scheme of our maps, and this function quantifies what fraction of the signals at each ℓ we retained as a result of averaging the signals within pixel areas. The values of this function is very close to 1.0 in the ℓ range relevant to this analysis because the resolution of our pixels is much finer than strictly necessary. In a one-dimensional case, the Fourier transform of the rectangle function whose width is equal to the interval between two adjacent samples of a time series (the pixel size of the time series in some sense) is a sinc function, and the value of the sinc function is $2/\pi$ at the Nyquist frequency corresponding to the sampling rate, the highest frequency that can be contained in the time series. Similarly, the resolution of a map pixel has a corresponding ℓ that we may call the Nyquist ℓ, and the value of the pixel window function at that ℓ is $2/\pi$. For this analysis, the maximum ℓ that we are interested in is 4000, and the corresponding pixel resolution is approximately 2.6 arc minutes. However, we chose

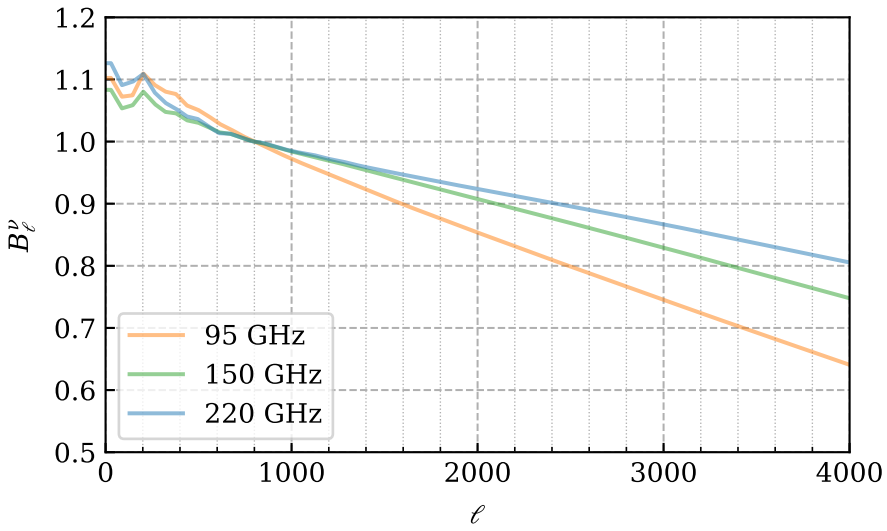

Figure 4.18. Fourier transforms of the beams.

our pixel resolution to be approximately 0.4 arc minute during the mapmaking to minimize pixel effects such as the pixel window function. As a result, our Nyquist ℓ is much higher than 4000, and the pixel window function is very close to 1.0 in the ℓ range that we are interested in. Compared with the other two types of multiplicative biases, this bias is much smaller.

After we divided the average cross-correlation spectra by these functions, we binned the unbiased spectra to create band powers.

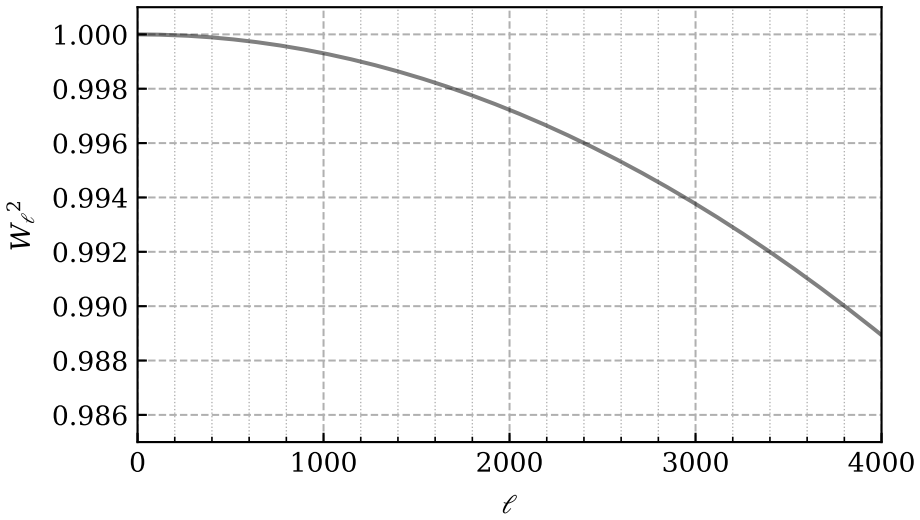

Figure 4.19. Pixel window function. This is the angular power spectrum of the average shape of our pixels. We use the notation $W_\ell{}^2$ to represent this quantity.

4.6 Band Powers

In this section, I show some of the band powers that we obtained from the 2019–2020 winter dataset and compare their uncertainties with those from the 2018 dataset and *Planck*.

Figure 4.20 shows all the autofrequency $EE/TE/TT$ band powers. The reason why the 220 GHz TT spectrum diverges from the other two TT spectra at relatively high ℓs is that it has more power from galaxies. The 150 GHz TT spectrum also diverges from the 95 GHz TT spectrum, but the difference is too small to see in this figure. The three EE spectra look identical because polarized emission from galaxies is negligible. The three TE spectra are expected to have no contributions from galaxies. This applies to the three TE spectra as well. The data points at ℓs below 400 are in fact not from this analysis because the timestream high-pass filter removed signals at those angular scales. These points are from an analysis that is based on the same dataset but filtered timestreams less heavily to retain and analyze low-ℓ polarization signals (Zebrowski et al., in prep.). In this analysis, 220 GHz maps are used to clean low-ℓ noise in 150 GHz maps, and 220 GHz band powers are unavailable. We

will possibly include those data points when constraining cosmological parameters.

Figure 4.21 compares the uncertainties in the 150 GHz EE/TE band powers shown in the previous figure with the uncertainties in the corresponding band powers obtained from the 2018 dataset. At relatively low ℓs, the uncertainties from both datasets are mostly caused by the sample variance discussed in section 2.4. Therefore, the new dataset does not improve much on the old one because the survey area has not changed. However, as ℓ becomes larger, the uncertainties receive larger relative contributions from the noise variance. Because the new dataset is nearly 10 times as large as the old one, the former improves on the latter by a similar factor as ℓ increases. The uncertainties in the TT band powers from the two datasets are not compared in the figure because we are limited by the sample variance in the entire ℓ range.

Figure 4.22 is the same as figure 4.21 except that the SPT-3G 2018 uncertainties were changed to *Planck*'s uncertainties. These comparisons reinforce the point that was made in section 2.4: SPT-3G complements *Planck* by making more precise measurements of the $EE/TE/TT$ spectra of the anisotropies of the CMB at high ℓs.

The total number of band powers that we obtained from this dataset was 936. As discussed in subsection 3.3.6, the size of an ℓ bin is 50, and our ℓ range of interest is from 400 to 4000, so there are 72 band powers for each of the 6 combinations of two frequency bands (95 GHz $\times$ 95 GHz, 95 GHz $\times$ 150 GHz, and so on) and for each of the 3 combinations of two anisotropy types ($E \times E$, $T \times E$, and $T \times T$). In total, we have 1512 band powers. Like the full-depth coadds, these band powers and the covariance matrix form another major part of the final analysis products that we plan to release to the public.

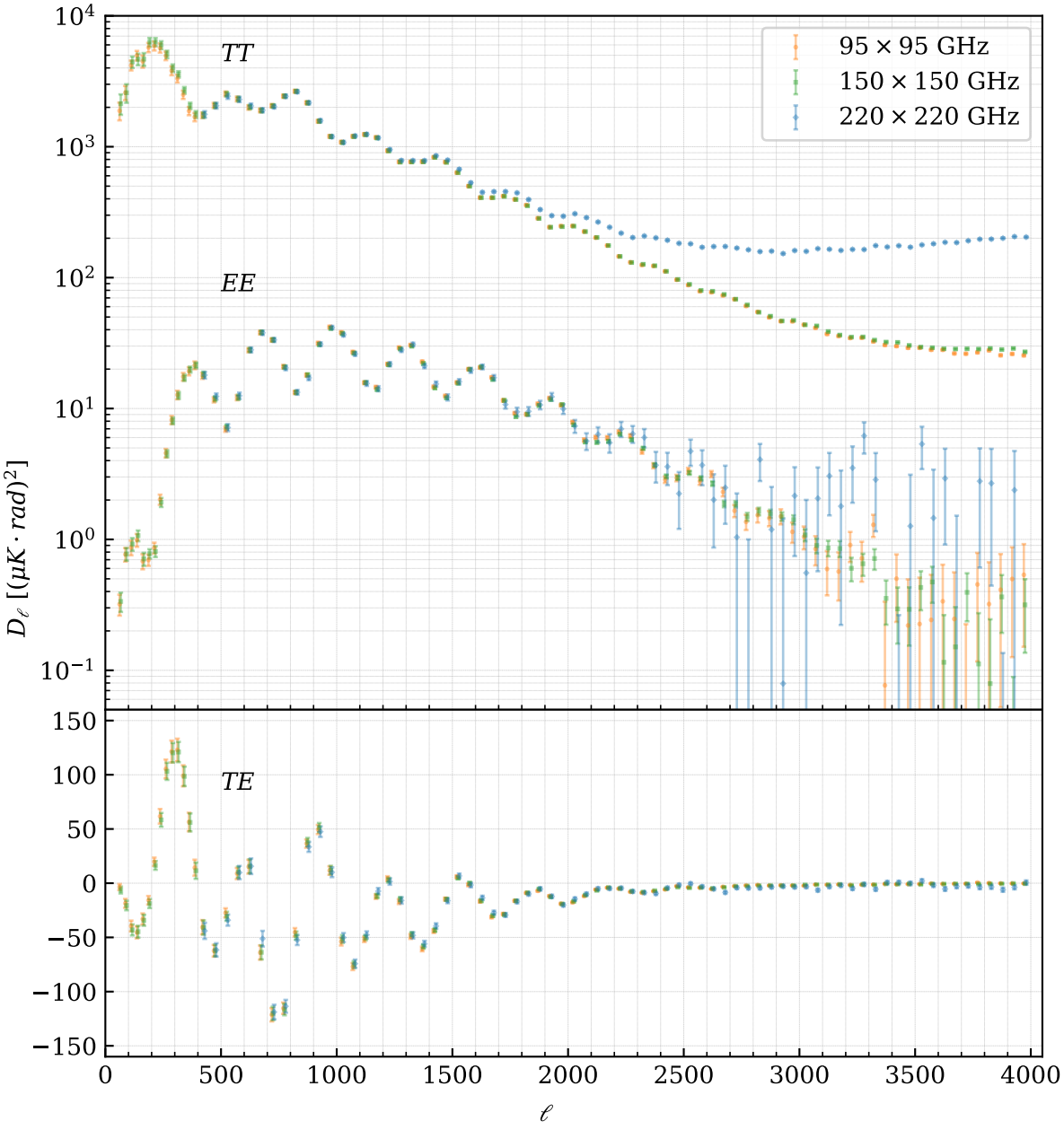

Figure 4.20. Autofrequency $EE/TE/TT$ band powers. The $EE/TE/TT$ band powers from the three autofrequency combinations are shown here. The band powers at ℓs below 400 are from another analysis.

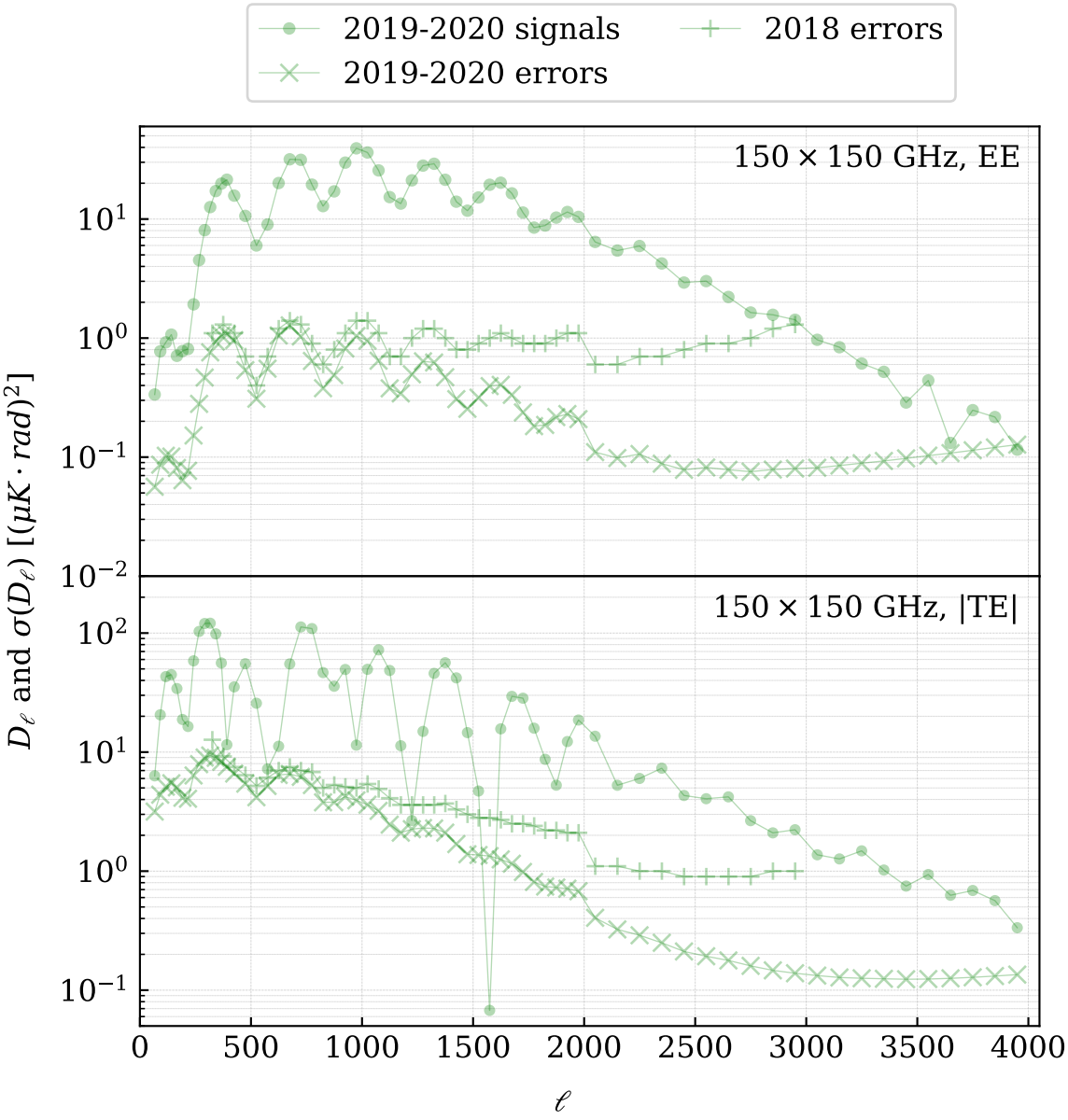

Figure 4.21. Band power uncertainties from the 2018 and 2019–2020 datasets. The top panel compares the two sets of uncertainties for the 150 GHz EE spectra, and the bottom panel is for the TE spectra. In the bottom, the absolute values of the TE signals are shown.

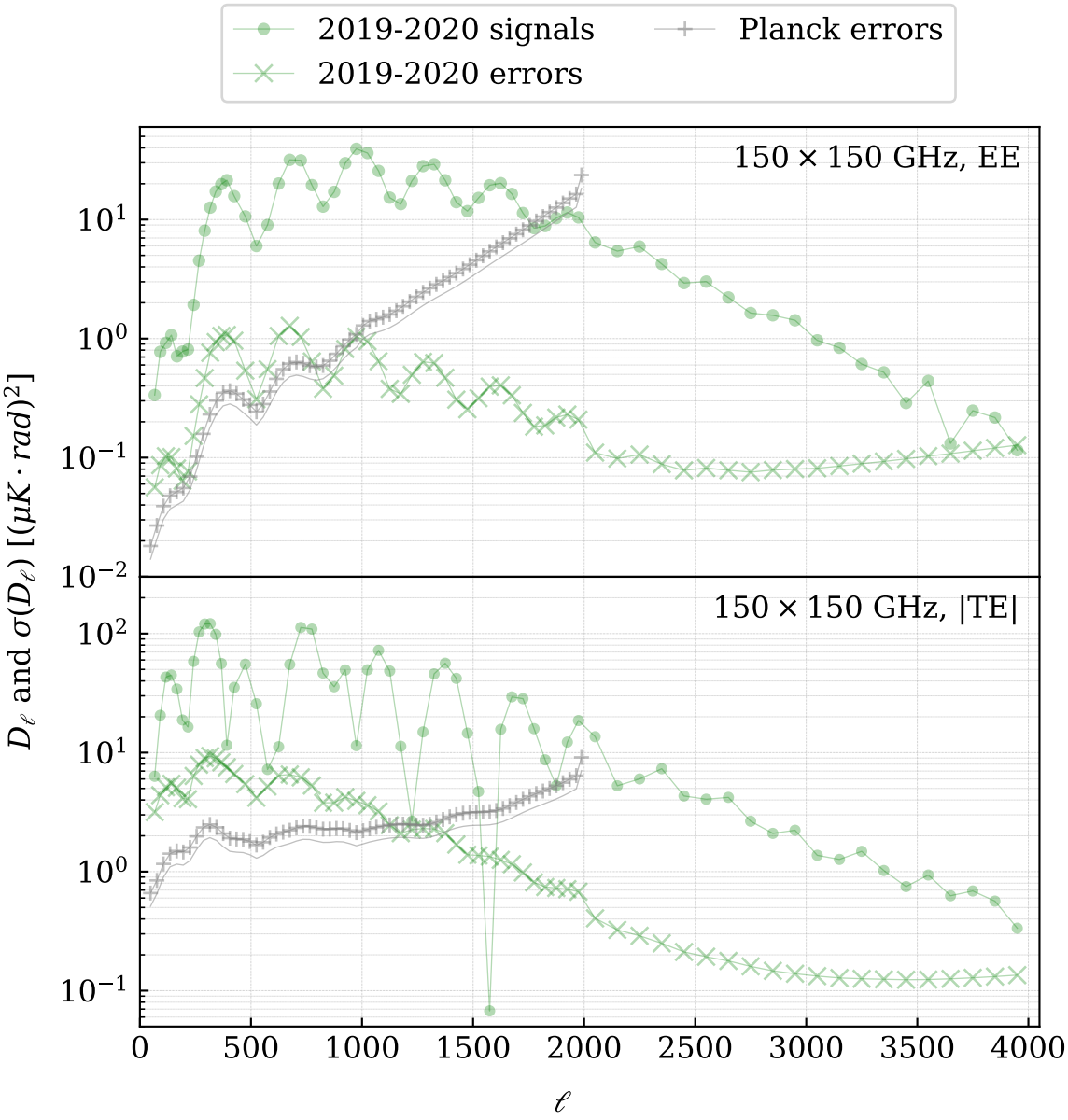

Figure 4.22. Band power uncertainties from the SPT-3G 2019–2020 dataset and *Planck*. The *Planck* data points were downloaded from the Planck Legacy Archive. They were obtained from maps in multiple frequency bands, while the SPT-3G data points are from only the 150 GHz bundles. Our errors will decrease at relatively high ℓs after we combine the band powers in all the frequency bands. Because the size of each *Planck* ℓ bin is 30 as opposed to 50, the *Planck* data points were also multiplied by $\sqrt{30/50}$ for fairer comparisons. This second set of *Planck* data points are shown as the gray curves below the gray pluses.

4.7 Future Steps

As of the writing of this thesis, we still have several analysis tasks to complete before we can obtain constraints on cosmological parameters. Currently, we are conducting two types of tests. First, we are conducting the interfrequency consistency tests discussed in subsection 3.3.5. We are testing whether our band powers in different frequency bands are consistent with each other. Second, we are conducting an alternate cosmology test discussed in subsection 3.4.2. We are testing an alternate model that has a high value for the Hubble constant and will possibly try more models. After we pass these tests, we will conduct the other test discussed in subsection 3.4.2, which is to check whether different subsets of our band powers yield consistent parameter constraints. I am very interested in seeing whether different subsets will yield statistically significantly different constraints on the Hubble constant. From the 2018 $EE/TE/TT$ analysis, we obtained 68.3 ± 1.5 km/s/Mpc by using the full set of band powers ($EE/TE/TT$ from the six combinations of the three frequency bands). We also obtained 65.1 ± 2.0 km/s/Mpc and 76.4 ± 3.8 km/s/Mpc by using the TE and EE band powers (from all the frequency combinations), respectively. The differences between these constraints and the constraint from the full set of band powers were not statistically significant in that case, but I am interested in seeing whether we will see similar differences at higher significance this time. If we find statistically significant differences, we will need to carefully examine whether they are caused by systematic errors in our band powers.

Once we pass all these tests, we will unblind our parameter constraints, and we will interpret them and compare them with existing results in the literature. Regarding the Hubble constant, by using the full set of band powers from the data that we took during the 2019–2020 winter observing seasons, we expect to be able to shrink the uncertainty to 0.9 km/s/Mpc. Furthermore, by combining these band powers with those from the data that we took during the summer observing seasons of those two years, an analysis of which

has been ongoing and is at a similar stage, we expect to be able to further shrink the uncertainty to 0.7 km/s/Mpc and approach the uncertainty achieved by *Planck*, which was 0.54 km/s/Mpc (Aghanim et al. [2020a]). With future analyses that will include data from additional years, we expect to be able to achieve smaller uncertainties than *Planck*. We are very excited about producing measurements of H_0 and other parameters that are competitive and complementary to *Planck*'s measurements by using the data from the two years.

While several important analysis tasks still remain to be done, we hope to be able to obtain parameter constraints in a few months.

REFERENCES

N. Aghanim et al. *Planck* 2018 results I. Overview and the cosmological legacy of Planck. *Astronomy and Astrophysics*, 641, 2020a. doi:10.1051/0004-6361/201833880.

N. Aghanim et al. *Planck* 2018 results VI. Cosmological Parameters. *Astronomy and Astrophysics*, 641, 2020b. doi:10.1051/0004-6361/201833910.

S. Aiola et al. The Atacama Cosmology Telescope: DR4 maps and cosmological parameters. *Journal of Cosmology and Astroparticle Physics*, 2020, 2020. doi:10.1088/1475-7516/2020/12/047.

L. Balkenhol and C. L. Reichardt. The parameter-level performance of covariance matrix conditioning in cosmic microwave background data analyses. *Monthly Notices of the Royal Astronomical Society*, 512(3):4394–4403, 2022. doi:10.1093/mnras/stac573.

L. Balkenhol et al. Constraints on ΛCDM extensions from the SPT-3G 2018 EE and TE power spectra. *Physical Review D*, 104, 2021. doi:10.1103/PhysRevD.104.083509.

L. Balkenhol et al. Measurement of the CMB temperature power spectrum and constraints on cosmology from the SPT-3G 2018 TT, TE, and EE dataset. *Physical Review D*, 108, 2023. doi:10.1103/PhysRevD.108.023510.

A. Bender et al. On-sky performance of the SPT-3G frequency-domain multiplexed readout. *Journal of Low Temperature Physics*, 199:182–191, 2020. doi:10.1007/s10909-019-02280-w.

C. L. Bennett et al. Four-Year COBE DMR Cosmic Microwave Background Observations: Maps and Basic Results. *The Astrophysical Journal*, 464(1):1–4, 1996. doi:10.1086/310075.

C. L. Bennett et al. First-Year Wilkinson Microwave Anisotropy Probe (WMAP) Observations: Preliminary Maps and Basic Results. *The Astrophysical Journal Supplement Series*, 148(1):1–27, 2003. doi:10.1086/377253.

M. L. Brown et al. Improved Measurements of the Temperature and Polarization of the Cosmic Microwave Background from QUaD. *The Astrophysical Journal*, 705(1):978–999, 2009. doi:10.1088/0004-637X/705/1/978.

E. Camphuis et al. Accurate cosmic microwave background covariance matrices: Exact calculation and approximations. *Astronomy and Astrophysics*, 668, 2022. doi:10.1051/0004-6361/202243948.

S. Choi et al. The Atacama Cosmology Telescope: a measurement of the Cosmic Microwave Background power spectra at 98 and 150 GHz. *Journal of Cosmology and Astroparticle Physics*, 2020, 2020. doi:10.1088/1475-7516/2020/12/045.

G. Chon et al. Fast Estimation of Polarization Power Spectra Using Correlation Functions. *Monthly Notices of the Royal Astronomical Society*, 350(3):914–926, 2004. doi:10.1111/j.1365-2966.2004.07737.x.

F. Couchot et al. Optimised polarimeter configurations for measuring the Stokes parameters of the cosmic microwave background radiation. *Astronomy and Astrophysics Supplement Series*, 135(3):579–584, 1999. doi:10.1051/aas:1999191.

A. T. Crites et al. Measurements of E-mode Polarization and Temperature-E-Mode Correlation in the Cosmic Microwave Background from 100 Square Degrees of SPTpol Data. *The Astrophysical Journal*, 805(1):36–54, 2015. doi:10.1088/0004-637X/805/1/36.

R. H. Dicke et al. COSMIC BLACK-BODY RADIATION. *The Astrophysical Journal*, 142: 414–419, 1965. doi:10.1086/148306.

D. Dutcher et al. Characterization and performance of the second-year SPT-3G focal plane. *Proceedings of the SPIE*, 10708, 2018. doi:10.1117/12.2312451.

D. Dutcher et al. Measurements of the E-mode polarization and temperature-E-mode correlation of the CMB from SPT-3G 2018 data. *Physical Review D*, 104, 2021. doi:10.1103/PhysRevD.104.022003.

D. J. Fixsen et al. The Cosmic Microwave Background Spectrum from the Full COBE FIRAS Data Set. *The Astrophysical Journal*, 473(2):576–587, 1996. doi:10.1086/178173.

S. Galli et al. CMB polarization can constrain cosmology better than CMB temperature. *Physical Review D*, 90, 2014. doi:10.1103/PhysRevD.90.063504.

K. Gorski et al. The HEALPix Primer. 1999. doi:10.48550/arXiv.astro-ph/9905275.

J. W. Henning et al. Measurements of the Temperature and E-mode Polarization of the CMB from 500 Square Degrees of SPTpol Data. *The Astrophysical Journal*, 852(2):97–128, 2018. doi:10.3847/1538-4357/aa9ff4.

E. Hivon et al. MASTER of the Cosmic Microwave Background Anisotropy Power Spectrum: A Fast Method for Statistical Analysis of Large and Complex Cosmic Microwave Background Data Sets. *The Astrophysical Journal*, 567(1):2–17, 2002. doi:10.1086/338126.

W. Hu and S. Dodelson. Cosmic Microwave Background Anisotropies. *Annual Review of Astronomy and Astrophysics*, 40:171–216, 2002. doi:10.1146/annurev.astro.40.060401.093926.

W. Hu and M. White. A CMB polarization primer. *New Astronomy*, 2(4):323–344, 1997. doi:10.1016/S1384-1076(97)00022-5.

W. Hu et al. Benchmark parameters for CMB polarization experiments. *Physical Review D*, 67, 2003. doi:10.1103/PhysRevD.67.043004.

L. Knox. Determination of inflationary observables by cosmic microwave background anisotropy experiments. *Physical Review D*, 52, 1995. doi:10.1103/PhysRevD.52.4307.

J. M. Kovac et al. Detection of polarization in the cosmic microwave background using DASI. *Nature*, 420:772–787, 2002. doi:10.1038/nature01269.

A. Lewis et al. Efficient Computation of Cosmic Microwave Background Anisotropies in Closed Friedmann-Robertson-Walker Models. *The Astrophysical Journal*, 538(2):473–476, 2000. doi:10.1086/309179.

J. C. Mather et al. A Preliminary Measurement of the Cosmic Microwave Background Spectrum by the Cosmic Background Explorer (COBE) Satellite. *The Astrophysical Journal*, 354:37–40, 1990. doi:10.1086/185717.

A. A. Penzias and R. W. Wilson. A Measurement of Excess Antenna Temperature at 4080 Mc/s. *The Astrophysical Journal*, 142:419–421, 1965. doi:10.1086/148306.

G. Polenta et al. Unbiased estimation of an angular power spectrum. *Journal of Cosmology and Astroparticle Physics*, 2005, 2005. doi:10.1088/1475-7516/2005/11/001.

C. M. Posada et al. Large arrays of dual-polarized multichroic TES detectors for CMB measurements with the SPT-3G receiver. *Proceedings of the SPIE*, 9914, 2016. doi:10.1117/12.2232912.

A. G. Riess et al. A Comprehensive Measurement of the Local Value of the Hubble Constant with $1\mathrm{km s}^{-1}\mathrm{Mpc}^{-1}$ Uncertainty from the Hubble Space Telescope and the SH0ES Team. *The Astrophysical Journal Letters*, 934(1), 2022. doi:10.3847/2041-8213/ac5c5b.

A. Rotti and K. Huffenberger. Real-space computation of E/B-mode maps. Part I. Formalism, compact kernels, and polarized filaments. *Journal of Cosmology and Astroparticle Physics*, 2019, 2019. doi:10.1088/1475-7516/2019/01/045.

J. A. Sobrin et al. The Design and Integrated Performance of SPT-3G. *The Astrophysical Journal Supplement Series*, 258, 2022. doi:10.3847/1538-4365/ac374f.

A. Spurio Mancini et al. CosmoPower: emulating cosmological power spectra for accelerated Bayesian inference from next-generation surveys. *Monthly Notices of the Royal Astronomical Society*, 511(2):1771–1788, 2022. doi:10.1093/mnras/stac064.

J. Torrado and A. Lewis. Cobaya: Code for Bayesian Analysis of hierarchical physical models. *Journal of Cosmology and Astroparticle Physics*, 2021, 2021. doi:10.1088/1475-7516/2021/05/057.

M. Zaldarriaga. Nature of the $E - B$ decomposition of CMB polarization. *Physical Review D*, 64, 2001. doi:10.1103/PhysRevD.64.103001.

M. Zaldarriaga and U. Seljak. All-sky analysis of polarization in the microwave background. *Physical Review D*, 55, 1997. doi:10.1103/PhysRevD.55.1830.

P. A. Zyla et al. The Review of Particle Physics (2020). *Progress of Theoretical and Experimental Physics*, 2020(8), 2020. doi:10.1093/ptep/ptaa104.